

HEMOZOIN: A CASE OF HEME CRYSTAL ENGINEERING

By

Anh N. Hoang

Dissertation

Submitted to the Faculty of the
Graduate School of Vanderbilt University
in partial fulfillment of the requirements

for the degree of

DOCTOR OF PHILOSOPHY

in

Interdisciplinary Materials Science

August, 2010

Nashville, Tennessee

Approved:

Dr. David W. Wright

Dr. David E. Cliffl

Dr. Todd D. Giorgio

Dr. Frederick R. Haselton

Dr. Kane G. Jennings

To my family-

Binh Hoang and Mau Tran

-parents who have given up their home and country for their children

Nguyen "Alex" Hoang

- a brother whose compassion for his community has inspired him to practice medicine.

Hoa Hoang

- a brother who wrote me letters while I was in college

Clint Lindsay

- my rock, my better half

ACKNOWLEDGEMENTS

This work would not have been possible without the financial support of Vanderbilt University, NIH (1R01AI083145-01), the U.S. Department of Defense (W81XWH-07-C-0092), The Medical Research Council of South Africa, and the University of Cape Town. Special thanks to The Vanderbilt/Fisk Interdisciplinary Program for Research & Education in the Nanosciences (NSF 0333392), which has not only provided me with financial support, but has provided me with the network to work and collaborate across departmental boundaries.

This work would also not have been possible without the advisement of my Ph.D. Committee members. To my advisor, Professor David Wright, who has tolerated my decisions to go to business school, to not go to business school, to post doc in Boulder (Colorado), to not go to Boulder, and finally, to accept a post doc. in Boston (Massachusetts). If the future permits and I become a faculty at a research institution, I too will allow my pet dog to decide the directions of my graduate students' research careers. In all seriousness, my time in your lab has not only taught me how to think scientifically and critically, but it has also taught me how to be an effective leader – someone who not only allows his students to make their own mistakes but also keeps them motivated to keep trying. To Professor David Cliffel- you have encouraged me to not take the “cream puff” route in graduate school and to maintain a work-life balance. Volleyball and video games at your house was always fun. Your parents-in-law makes the best meatballs. To Professor Todd Giorgio and Professor Rick Haselton -your excitements in bio-inspired application have encouraged me to pursue a post doc in biomedical engineering. Dr. Giorgio- your course in Biotechnology has introduced me to the world of cellular manipulation and the opportunities that have yet to be discovered. Professor Haselton- your daily enthusiasms

(about the coffee ring project) has served as a constant reminder of how awesomeness of medical application discoveries. To Professor. Kane Jennings- your group has probably not told you that I am a frequent user of your contact angle, surface tension, and IR instruments, but thank you.

Thank you all.

To Professor Timothy Egan- you are a professor that I hope to emulate. You inspire your students, engage the public in scientific research, and model your students to be observant and critical scientists. Thank you for hosting and showing me the Cape Town.

My joint memberships to Professor Wright and Professor Cliffel's groups have surrounded me with a mountain of support. These people have helped me troubleshoot experimental problems and provided insightful discussions throughout my academic pursuit. But I will remember them best for the times in between experiments and after work hours. Rebecca Sandlin, my sister from another mother, you have convinced me that kinetic experiment does not work during an overcastted day and that fruits taste best when we have to sneak out of the lab to go to the Farmer's Market to get them. Leslie Hiatt – you are my go-to-person for all things electronic and QCM malfunction. I know you will be a good professor. Jennifer (Merritt) McKenzie- a fellow member of the exclusive pizza club always knows how I like my pizza. Jonas Perez – you've shown me that drinking a gallon of water each day doesn't kill a person, but the multiple trips to the bathroom just might. John Stone – thanks for all the help with paper revisions and career directions. Brian Turner- do you remember those dinner parties that we had pre-married days? Joshua Swartz – I still owe you \$2 from your lab snack store. Kellen Harkness- your dual life as a graduate student and father is inspiring. Stevie Jackson- your first intoxication episode is priceless but won you a seat in the “cool” kid table. Chris Gulka- mango club was awesome. Make sure Becca waits awhile before finding my replacement in the SB club.

Matthew Bryant- you're the first person I know that pops his labcoat collar. Your care for your family makes me miss mine. Mika Meschievitz- I love the haircut. Nick Adams- before you came along, the group didn't know how a Mormon is suppose to look like ;P. Have fun in Nashville and I might run into you back in Utah. Noelle Holmes- I wish I am as good with kids as you are. Gongping Chen – thanks for the hair advice. Perm hair is definitely better! To the former lab members- Reese Harry and Kristen HalfPenny good luck in your career pursuit! Alex and Ryan Rutledge and Leila Deravi – Tuesday Trivia Night was a blast! Can't wait for Thanksgiving reunion in Boston. Good luck to all. Please keep in touch.

This work cannot be completed without the support of my friends and family. They have tolerated my regular absence from their lives for the last four years. To my family- Binh and Mau Tran- thank you for your constant support (and phone calls). It's been eight years. Another 2-3 years and maybe I'll make something of myself. To Nguyen and Hoa – I don't think I can ask for better brothers. You guys are whom I brag about. To Clint- who has weathered all the emotions and drama that came with irregular lab hours and experimental failure. You are my rock. Thank you. Thang Dao- my complicated and sister, you and Mayur are my extended family. Crystal Nguyen – wish your post doc. is in Boston. Have fun in San Diego and thanks for the furniture. Chi Trang- can't wait to see you and O again in the fall. Jodi McKenzie, Chisanga Lwatula, and Farah Siddique – thank you for your constant support and phone calls.

And finally, thank you to Professor Rosenthal and Professor Eva Harth. They have provided me career guidance throughout my time at Vanderbilt. To Professor Tim Hanusa – rock collecting is fun. Come to the mountain west and we can show you some spots for rock hounding. Sarah Satterwhite, Rene Colehour, Sandra Ford, and Shellie Richards- without you

guys, I would not be able to navigate my way around the paperwork in graduate school. Thank you for making sure I get paid and meet all the requirements.

TABLE OF CONTENTS

	Page
DEDICATION	ii
ACKNOWLEDGEMENTS	iii
LIST OF TABLES	viii
LIST OF SCHEMES	viii
LIST OF FIGURES	ix
Chapter	
I. INTRODUCTION	1
Hemozoin: a case of heme crystal engineering	1
Malaria review	2
Hemoglobin degradation	3
Heme metabolism	6
Hemozoin characterization	7
Biological mediator of hemozoin formation	11
Antimalarials	12
II. NEUTRAL LIPID MEDIATION OF HEMOZOIN FORMATION	15
Experimental	17
Results and Discussion	26
Conclusions	61
III. INTERACTIONS OF NEUTRAL LIPIDS AND FERRI- PROTOPORPHYRIN IX DURING HEMOZOIN FORMATION IN LANGMUIR-BLODGETT FILMS.....	65
Experimental	67
Results and Discussion	74
Conclusions	90
IV. CRYSTAL ENGINEERING: SOLVENT'S EFFECT ON BETA-HEMATIN FORMATION.....	92
Experimental	94

Results and Discussion	100
Conclusions	133
V. PHAGE DISPLAY APPLICATION TO BETA-HEMATIN.....	135
Experimental	137
Results and Discussion	151
Conclusions	170
REFERENCES.....	172
Appendix	
A. CONFOCAL MICROGRAPH OF NILE RED LABELED LIPID BODIES IN PRESENCE OF FE(III)PPIX.....	187
B. MN(III)PPIX CRYSTALLIZATION IN CITRIC BUFFER: DMSO SYSTEM.....	188
C. PHAGE DISPLAY PANNING PROTOCOL.....	180
D. PHAGE TITERING OPTIMIZATON PROTOCOL.....	192
CURRICULUM VITAE.....	193

LIST OF TABLES

Table No.	Page
1. Properties of solvents used to investigate beta-hematin morphologies.....	127
2. Measured surface tension of citrate buffer: solvent system.....	127
3. Seven amino acid sequences identified through phage panning.....	159

LIST OF SCHEMES

Scheme No.	Page
1. Life cycle of the <i>Plasmodium falciparum</i> within the human host.....	5
2. Evolution of the lipid emulsion following deposition of a solution on the aqueous surface.....	29
3. The proposed mechanism of hemozoin formation under neutral lipid mediation.....	43
4. Langmuir monolayer compression surface pressure-area (π -A) isotherms.....	69
5. The chemical formulas for compounds investigated via Langmuir compression.....	71
6. Proposed lipid-Fe(III)PPIX interaction during hemozoin formation.....	89
7. Beta-hematin phage display experimental procedure.	139
8. Selection and amplification of individual phage.....	141

LIST OF FIGURES

Figure No.	Page
1. Hemozoin's chemical structure.....	8
2. Characterization of hemozoin and beta-hematin.....	10
3. Hemozoin-chloroquine interaction model.....	14
4. Characterization of monopalmitoyl glycerol in acetone/methanol solution after deposition onto an aqueous surface.....	27
5. TEM image of heme localized at or near the lipid-water interface.....	31
6. Infrared, X-ray diffraction, and transmission electron microscopy evidence for the formation of beta-hematin at the lipid-water interface using MSG and MPG.....	32
7. Beta-Hematin formation using various neutral lipids.....	34
8. Comparison of efficiency of lipids, solvents and amphiphiles in forming beta-hematin at the interface with aqueous solution.....	36
9. TEM of beta-hematin formed at the MSG/water and MPG/water interface through methods of extrusion.....	39
10. Temperature and pH dependence of beta-hematin formation at the lipid-water interface.....	41
11. Confocal micrographs of synthetic neutral lipid bodies and zeta potentials of synthetic neutral lipid body and its components.....	46
12. Differential scanning calorimetry of individual lipids and SNLB.....	48
13. Characterization of beta-hematin produced using synthetic neutral	

lipid body	52
14. Kinetics and activation energy of beta-hematin formation under neutral lipid mediation.....	52
15. A typical fluorescence emission spectrum of Nile Red in synthetic neutral lipid body dispersed in aqueous solution.....	55
16. Linearity of fluorescence response and dependence of fluorescence quenching by Fe(III)PPIX on pH.....	57
17. Confocal micrographs of Nile Red labeled synthetic neutral lipid body droplets in the presence of Fe(III)PPIX.....	58
18. Surface pressure-area isotherms and limiting packing area of mono-, di-, and tripalmitoyl glycerol and the lipid blend.....	76
19. Pressure-area (π -A) of lipid blend and protoporphyrin-lipid blend mixtures at 100 μ M.....	79
20. PH dependence of lipid blend-Fe(III)PPIX packing.....	82
21. Langmuir compression of premixed chloroquine, Fe(III)PPIX, and lipid blend....	84
22. Fluorescence spectra of synthetic neutral lipid body tagged with the hydrophobic dye, Nile Red.....	86
23. Fluorescence spectra of chloroquine and Fe(III)PPIX and the Nile Red labeled SNLB system.....	88
24. DMSO promotes spontaneous heme solubilization.....	102
25. DMSO promotes spontaneous heme crystallization.....	102
26. Increase in DMSO content promotes spontaneous heme solubilization and crystallization.....	106

27. PEGs are able to induce beta-hematin formation under acid conditions.....	108
28. Scanning electron micrographs of beta-hematin induced by PEGs.....	110
29. Prior heme solubilization by PEGs and organic solvents promote spontaneous heme crystallization.....	112
30. Heme solubility and beta-hematin produced in DMSO solution increase with reduced water activity.....	115
31. The addition of DMSO, DMF, THF, MeCN to a solution of aqueous Fe(III)PPIX increased heme solubility.....	118
32. Product characterization of crystals formed under citrate buffer: solvent system...	120
33. PH effects of beta-hematin formation under DMF, DMSO, and THF.....	123
34. Effect of temperature on beta-hematin morphologies.....	125
35. Effects of solvent concentration of beta-hematin formation.....	128
36. Kinetics of beta-hematin formation under solvent: CB system.....	130
37. Formation of beta-hematin using mixed (DMF and toluene) solvents.....	132
38. Beta-hematin self assemble monolayer.....	144
39. Polymerase chain reaction (PCR) is a method to amplify select DNA sequence using cycles of repeated heating and cooling.....	148
40. Increased panning rounds reduces non-specific phage.....	152
41. Functionalization of beta-hematin crystal onto quartz crystal microbalance (QCM) chip.....	154
42. QCM quantification of round 5 phage recognition of beta-hematin surface.....	155
43. QCM measurements of round 5 phage and BSA-blocked poly-lysine served as a control for phage recognition of beta-hematin.....	156

44. Electrophoresis analysis of round 5 PCR products confirmed the presence of 240 bp DNA fragment.....	158
45. Peptide mediation of beta-hematin formation in acetate buffer and citric buffer conditions.....	161
46. FTIR and XRD analysis of products form by EDKNNVA.....	163
47. Peptides do not possess beta-hematin inhibiting properties.....	164
48. Kinetic of beta-hematin formation for ASDEQPS, SITEDKN, and EDKNNVA in acetate buffer.....	166
49. Dynamic light scattering measurements of ASDQEPS, EDKNNVA, and SITEDKN.....	168
50. Confocal micrographs of Nile Red labeled synthetic neutral lipid bodies.....	187
51. Characterization of Mn(III)PPIX crystals produced in citric buffer: DMSO system.....	190

Chapter I

HEMOZOIN: A CASE OF HEME CRYSTAL ENGINEERING

Nature provides numerous examples of organic-inorganic interactions that produce precisely controlled biominerals in which structural morphologies are reproducible in size, shape and orientation (1). This process by which living organisms produce minerals is referred to as biomineralization. For example, many multicellular organisms produce hard tissues such as bones, teeth, shells, skeletal units, and spicules. These minerals can serve as mechanical devices (e.g., skeletal support, cutting, grinding) or physical function (e.g., magnetic and optical) (2, 3). The detailed mechanism of biomineralization is far from complete; however, current understanding points to mediation by organic molecules. Organic macromolecules may act as nucleators, growth modifiers, anchoring units, compartments, or scaffold in mineral growth (4). These roles can be achieved through templating (1, 5, 6) or enzymatic (7) effects. As a template, macromolecules can provide stereochemistry and physisorption for the inorganic assembly (1). In contrast, as an enzyme, the macromolecule could regulate inorganic phase synthesis by controlling local chemistry (3). While biominerals can provide mechanical support, their presence in human can indicate medical complications. Despite the practical functionality of calcium oxalate monohydrate as mechanical support in plants (8), their presence in humans, better known as kidney stone, can cause painful inflammation. While considerable advances have been made in understanding how the organic components of organisms (proteins(9) and lipids(10)) direct the formation for some biominerals, in many cases their role remains unclear. This is especially with hemozoin, a dark, crystalline heme pigment (11, 12). Heme or

Fe(III)PPIX is the precursor of hemozoin and its potential role in a number of pathogenic conditions has produced a surge of research interest in hemozoin formation. Blood feeding organisms implicated in malaria (11), schistosomiasis (13), and Chagas' disease (14) , namely, the malaria parasite *Plasmodium falciparum*, the worm *Schistosoma mansoni*, and the kissing bug *Rhodnius Prolixus*, produces hemozoin to circumvent heme toxicity associated with hemoglobin degradation (15). A better understanding of hemozoin and its formation will shed new light on these diseases and drug designs to combat them.

Malaria Review

Malaria is a disease that is rooted in human history, having been clinically described as early as the fourth century B.C by Hippocrates. However, it wasn't until the 19th century that Charles Laveran established a causal relationship of pigmentation to the malaria parasite (1880) (16), through his observation of moving bodies from blood samples of patients suspected of having malaria. And a decade later, Sir Ronald Ross linked the transmission of the disease to mosquitoes and reported the life cycle of the parasite. Despite its rich history, molecular understanding of the disease is still incomplete. Today, malaria is classified as a protozoan parasitic disease that is a leading public health and economic burden. The disease infects 300-500 million children annually and is endemic in over 100 countries (17). The majority of these cases occur in Sub-Sahara Africa (17). With the recent increase in parasite resistance to traditional antimalarial drugs and vector resistance to insecticides, an in-depth understanding of the disease is crucial for the future treatment of this disease.

Malaria is caused by parasites belonging to the genus *Plasmodium*. Four species have been shown to infect humans: *Plasmodium falciparum*, *Plasmodium ovale*, *Plasmodium malariae* and *Plasmodium vivax*. *Plasmodium falciparum*, the most prevalent species is often fatal to humans.

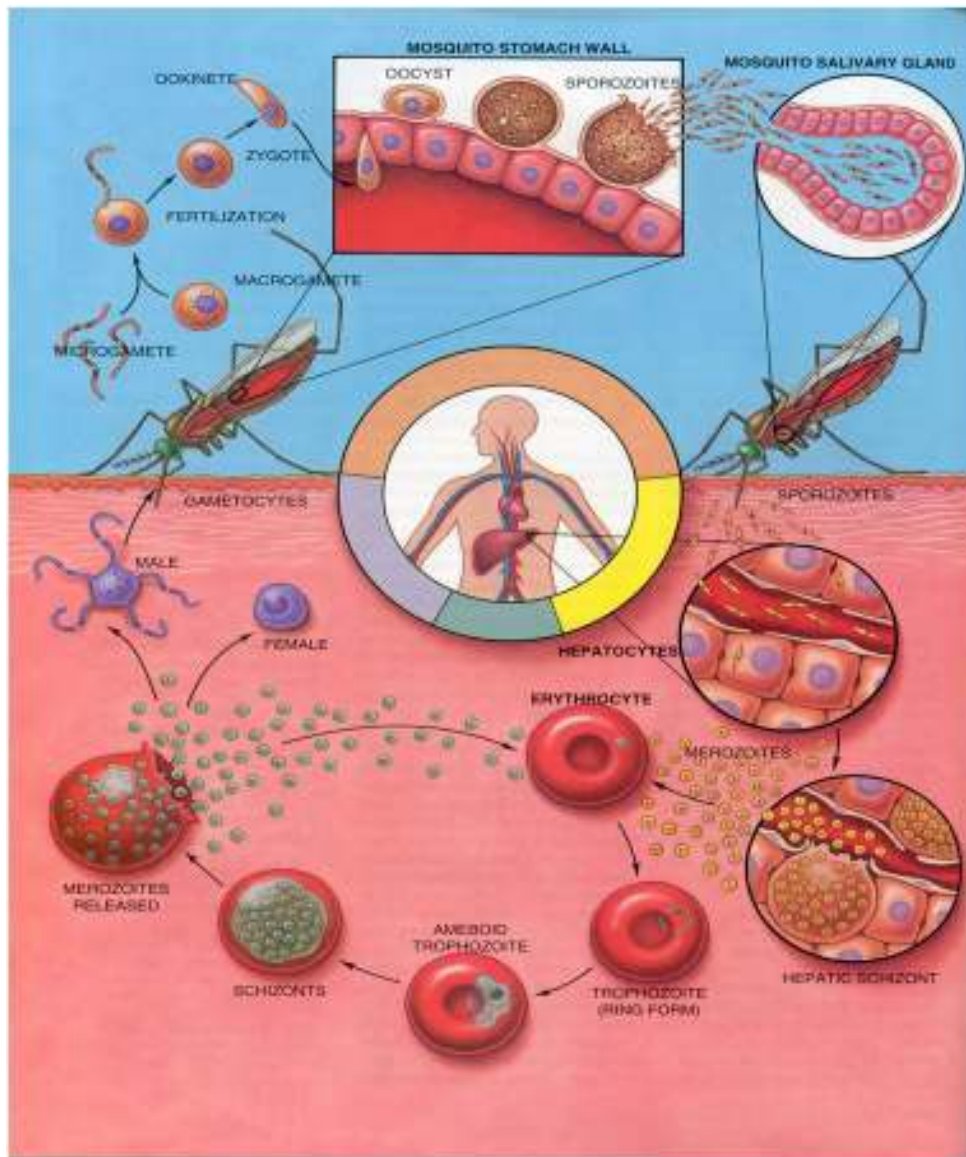
The life cycle of *Plasmodium Falciparum* is divided into three stages: vector (mosquito), liver (host), and blood (host) stages. Briefly, the life cycle of *P. falciparum* begins when a female mosquito transfers the malaria parasite to her human host (Scheme 1). The sporozoite travels through the bloodstream and invades the liver cells where it develops for 5-10 days. During the liver stage the sporozoite undergoes asexual reproduction to form tissue schizont which then develops to form merozoite. The end of the liver stage is signified by merozoites rupturing the liver cells and invading red blood cells (RBC). In the RBC, the merozoite matures into trophozoite which develops further to form schizont. These schizonts develop, divide, and then rupture from the RBC, releasing additional merozoites ready to begin another cycle by invading another RBC. The RBC cycle is associated with symptoms of clinical malaria such as chills, fever, and anemia. If left untreated, these symptoms may escalate to death. Some merozoites develop into sexual forms called gametocytes which can be taken up by another mosquito during its feeding. In the gut, these gametocytes matures into oocysts and then into sporozoites. The sporozoites then travel to the salivary gland where it waits to be injected into the next host.

Hemoglobin Degradation

The malaria parasite has a limited capacity to synthesize amino acids *de novo*, and consequently, must scavenge nutrient exogenously by catabolizing the host's supply. Within the RBC, *P. falciparum* attains nutrients by degrading hemoglobin (Hb), a protein responsible for the

host's oxygen transport (18). Hb is transported into the acidic digestive food vacuole (pH 4.8 \pm 0.4) (19, 20) via transport vesicles known as cytotome. During the intraerythrocytic stage, the malaria parasite can degrade up to 80% of the host's hemoglobin (21). To illustrate this phenomenon, in an average patient with 750 g of health hemoglobin and a 20% parasitemia, as much as 100 g of hemoglobin can be degraded during this cycle (11). These peptides are further hydrolyzed into amino acid in the parasite cytosol. As a consequence of Hb degradation, heme is released. In the "free" state, heme induces oxygen dependent free radical formation, lipid peroxidation and protein and DNA oxidation. *P. falciparum* has evolved efficient adaptations to circumvent the toxic effects of "free" heme. This process involves the crystallization of heme into hemozoin which is nontoxic to the parasite.

Inside the parasite, the degradation of hemoglobin takes place within the acidic lysosomal organelle called the digestive food vacuole (22). Within this compartment, a suite of *Plasmodial* proteinases, including two aspartic proteases, plasmepsin I and II, and one cysteine protease, falcipain, breaks down the hemoglobin protein (18). This process begins with a cleavage between residues α 33Phe and α 34Leu by an aspartic protease (23). This site of cleavage is critical for securing the hemoglobin tetramer together when oxygen is bound (24). Plasmepsin I and II further cleave the fragment at secondary sites. These fragments are substrates for the cysteine protease falcipain (25), which continues to break down the fragments into smaller units. Inhibition of Plasmepsin I/II and cysteine protease falcipain results in parasite death. Metalloprotease found in the digestive vacuole are the final enzyme that acts on the fragments prior to transport of the small peptides from the digestive vacuole into the cytoplasm where they are further degraded to amino acids (26).



Scheme 1. Life cycle of the *Plasmodium falciparum* within the human host (27).

Heme Metabolism

Iron protoporphyrin IX or heme is a ubiquitous molecule that is essential for the function of all aerobic cells (i.e. biological processes, including oxygen transport, respiration, photosynthesis, drug detoxification, and signal transduction) (28). Despite the necessity of heme for biological functions, free heme can generate reactive oxygen species that can damage biological molecules. The root of free heme cytotoxicity involves its highly hydrophobic nature which allows the iron contained within its protoporphyrin IX ring to enter and cross cell membranes (29). Its amphiphilic nature favors its association with phospholipid bilayers, interfering with the physical integrity (30). As a consequence, the toxic effect of heme is associated with diverse pathologies such as inflammation, atherosclerosis, Alzheimer's and Parkinson's diseases. It is not surprising that evolution has developed many adaptations to protect organisms against the detrimental consequences of free heme (31).

Heme oxygenase -1 (HO-1) is an essential enzyme in the heme breakdown (32). To date, two isozymes of HO are known, HO-1 and HO-2 (33), and a possibility of a third, HO-3, remains debatable (34). HO activity is higher in tissues (spleen, liver, and bone marrow) where senescent erythrocytes are sequestered and degraded (35). Characteristically, HO-1 and HO-2 are highly induced by its substrate heme (35-37) and binds to heme in an equimolar ratio using the reduced form of nicotinamide-adenin dinucleotide phosphate (NADPH), three molecules of oxygen and at least seven electrons provided by NADPH-cytochrome P450 reductase (38). Both HO isoforms can cleave the protoporphyrin IX ring of free heme, releasing Fe from its inner core and generating carbon monoxide. The remaining protoporphyrin structure gives rise to

biliverdine which is reduced to bilirubin, transported to the liver conjugated with glucuronic acid and excreted into bile (39).

Plasmodium, the causative agent of malaria, lacks the enzyme heme oxygenase to catabolize the porphyrin moiety, and must address heme toxicity by converting heme to hemozoin. Interestingly, mouse strain that expresses high level of HO-1 in response to *Plasmodium* infection do not succumb to severe and/or cerebral malaria, while those that express low level of HO-1 do so (40).

Hemozoin Characterization

Hemozoin was first observed as the discoloration in organs of malaria patient, and was later reported as a byproduct of hemoglobin degradation. It is a microcrystalline cyclic dimer of ferriprotoporphyrin IX (Fe(III)PPIX) in which the propionate side chain of one protoporphyrin coordinates to the iron(III) centre of the other. The dimers hydrogen bond to their neighbours *via* the second propionic acid group, forming extended chains through the macroscopic crystal (41, 42). Hemozoin is chemically and structurally similar to a distinctive hematin pigment, called beta-hematin (Figure 1) (43). Today, all synthetic hematin-crystals with iron of one hematin bound to the propionic acid group of another hematin are called beta-hematin. It should be noted that this terminology does not convey possible variations in three-dimensional structure.

Chemically, hemozoin and its synthetic counterpart can be identified by Fourier transform infrared spectroscopy with intense absorbance at 1664 cm^{-1} , corresponding to the C=O stretching vibration, and at 1210 cm^{-1} , corresponding to the C-O stretching vibration (Figure 2d) (42). These peaks were absent from the spectra of the synthetic substrates hemin chloride and

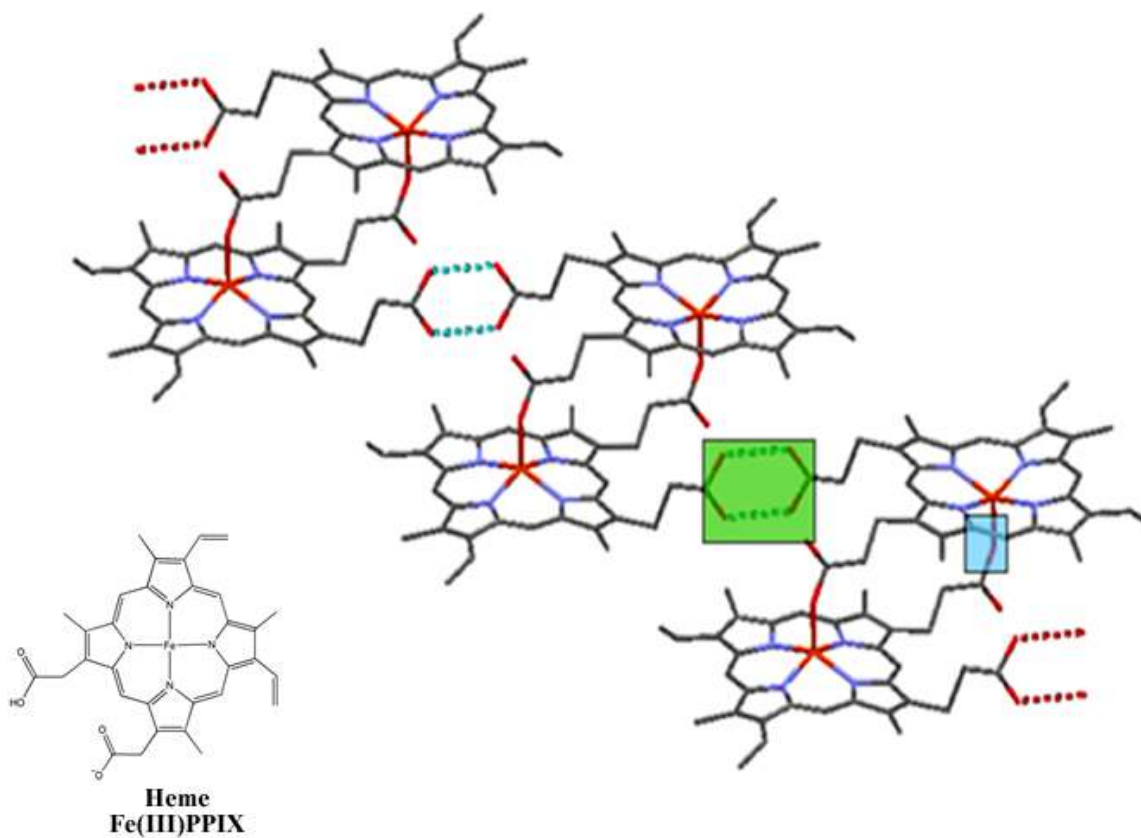


Figure 1. Hemozoin's chemical structure. Hemozoin is a crystalline dimer which is composed of direct a coordination between a propionate group of one Fe(III)PPIX and the iron of another heme dimer unit . The dimers hydrogen bond to form an extended network, making up the macroscopic crystal.

hematin, suggesting a direct coordination between the carboxylate of one heme monomer and the iron center of another. The presence of these peaks signifies the formation of precursor Fe(III)PPIX dimers. Structurally, hemozoin and beta-hematin are identical at the atomic level with distinct powder x-ray diffraction peaks at 7, 22, and 24 2θ (θ) (Figure 2e). These structures were determined using simulated annealing techniques on the diffraction data, which includes the use of Le Bail algorithm to compare integrated peak intensities, the Rietveld refinement of the structure's molecular bonding geometry and Fourier difference calculations of atomic positions (41). The diffraction pattern proposed a triclinic unit cell with a space group of P-1, indicating an inversion of symmetry between the unit cells of the Fe(III)PPIX dimer. This pattern suggests a five-coordinate Fe(III)PPIX dimer bound by reciprocal monodentate carboxylate interactions with the propionic side chains of each PPIX (41).

Morphologically, scanning electron microscopy analysis show hemozoin from *P. falciparum* from human have a regular, flat-faced, needle-like structure (Figure 2 b,c) (44). These structures are micron-size crystals with three dominant side faces: {100}, {010}, and {001}. This morphology is determined by the relative growth rate of its various faces. Briefly, the morphological properties of a crystal depends on the relationship between the layer energy, E_1 , the energy released when a layer is formed, and the attachment energy, E_{att} , the energy per molecule released when a new layer is attached to the crystal face. E_{att} regulates the growth rate perpendicular to the layer, while E_1 controls the stability of the layer. The morphological importance of crystal face is inversely proportional to its attachment energy. Generally, the face that grows slowest is expressed in the crystal habit. Values for E_1 and E_{att} of hemozoin were calculated by Buller *et al* (45) via computational modeling of atom-atom potential energy functions. These calculations predicted low E_{att} for {001} (-101.5 kcal/mol) and larger values

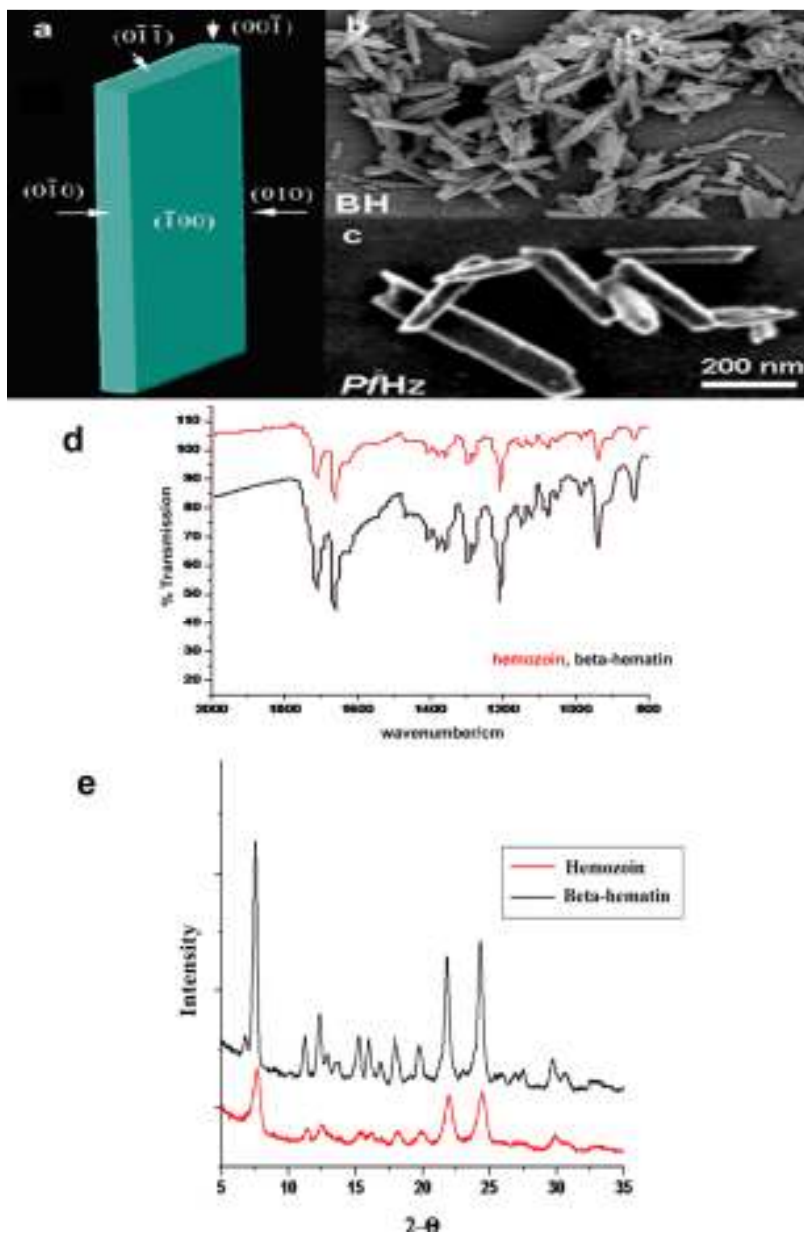


Figure 2. Characterization of hemozoin and beta-hematin. Morphologically, both hemozoin(c) and beta-hematin (b) are needle-like in structure. FT-IR analysis (d) of both samples revealed characteristic peaks at 1664 cm^{-1} and 1210 cm^{-1} , indicating the presence of a heme dimer. X-ray diffraction patterns of hemozoin and beta-hematin exhibit characteristic peaks at 7, 22, and 24 2θ (e).

for {100} (-30.6 kcal/mol) and {010} (-27.7 kcal/mol) side faces. From these predictions, the authors proposed that the fastest growing face of hemozoin is likely to be the {001}. Thus, stabilization of dominate crystal faces, {010} and {100} may promote crystal nucleation; and binding onto the fastest growing face, {001}, may inhibit crystal growth.

Biological Mediator of Hemozoin Formation

Nearly 95% of the heme released from hemoglobin degradation is converted into the malaria pigment in *Plasmodium Falciparum* (46); however, the molecular understanding of this process remains unclear. The history of hemozoin research comprises of three main hypotheses for hemozoin formation: enzymatic mediated, protein mediated, and lipid mediated. Initially, Slater and Cerami (47) observed that extracts of *P. Falciparum* trophozoites incubated with heme in sodium acetate at physiological conditions was sufficient in converting hematin to beta-hematin. This conversion was inhibited by the addition of quinoline-containing drugs (47). This observation led them to propose that the formation of hemozoin was catalyzed by a heme polymerase enzyme. Dorn *et al.* refuted the “heme polymerase” proposal by demonstrating that the same catalytic property was conserved in parasitic extract that were subjected to heat treatment (48). They concluded that hemozoin formation is a chemical process rather than an enzymatic process.

Another spotlight in the search for a mediator of hemozoin formation was the histidine-rich protein (HRP). Sullivan *et al.* identified two proteins, HRPII and HRPIII, that were sufficient at mediating beta-hematin formation (49). HRP II contains 51 repeats of the sequence Ala-His-His, making up 76% of the mature protein (50). HRPIII contains 28 Ala-His-His

sequences, making up 56% of its mature protein (51). Functionalized nanoparticles containing HRP epitope promoted beta-hematin in a pH dependent manner with optimal conversion at pH4, similar to that of the digestive food vacuole of *Plasmodium falciparum*. However, reports of HRP's location outside the digestive vacuole (52) and *P. falciparum* clone that lack the genes for both HRP II and HRPIII still retain hemozoin production (53) made the first proposal unlikely.

Currently, research in hemozoin formation is focused on lipids. The role of neutral lipids on hemozoin crystallization was initially proposed by Fitch *et al.* (54) and was later identified as composing of di- and triacyl- glycerols (55). Most importantly, Sullivan and coworkers reported the presence of neutral lipid bodies enveloping hemozoin crystals inside *P. Falciparum* digestive vacuoles (56). These lipid bodies were identified as a mixture of mono and di-glycerides (57). Recently, Egan and colleagues (58) demonstrated the beta-hematin formation occurs at the lipid-water interface and that the rate of heme conversion can account for heme toxicity. However, the details of this mechanism are unknown.

Antimalarials

The quinoline family of drugs has served as the primary treatment for malaria for over 300 years (11). Chloroquine (CQ), a synthetic analogue of the oldest known antimalarial, quinine, was extensively used for half a century as the major antimalarial throughout the world. Its popularity stemmed from its being an effective antimalarial and inexpensive. Chloroquine exist in the neutral form within the body ($pK_{a1}=8.1$ and $pK_{a2} = 10.2$), allowing it to passively transport through cell membranes. However, within the digestive food vacuole of *P. falciparum* (pH 4.8 ± 0.4) parasite the drug is doubly protonated (45), explaining its accumulation within the vacuole up to millimolar concentration (59-63). The extensive use of chloroquine and surging

resistance have encouraged production of other effect quinoline analogues that includes the bicyclic quinoline skeleton and a flexible amine moiety(64, 65). There is an abundance of evidence that suggests chloroquine and related aminoquinoline compounds stems from their ability to complex with free heme released during hemoglobin degradation (Figure 3) (66-68). Likewise, computational models reveal that this crystal “capping” effect is brought about when CQ blocks the {001} and {010} crystal face, preventing growth.

Growing parasite’s resistance to chloroquine and many of the quinoline based anti-malarial drugs has paved way for the resurface of the malaria disease. It is believed that the parasite acquires resistance through an efflux mechanism which prevents the accumulation of drugs within the digestive food vacuole, the site of hemozoin formation, in the parasite (20, 69). Because the mechanism of drug resistance does not disrupt the heme conversion, the conversion of heme to hemozoin remains a potential target for therapeutic treatments. Thus, a more detailed understanding of hemozoin formation will shed new light on malaria treatments.

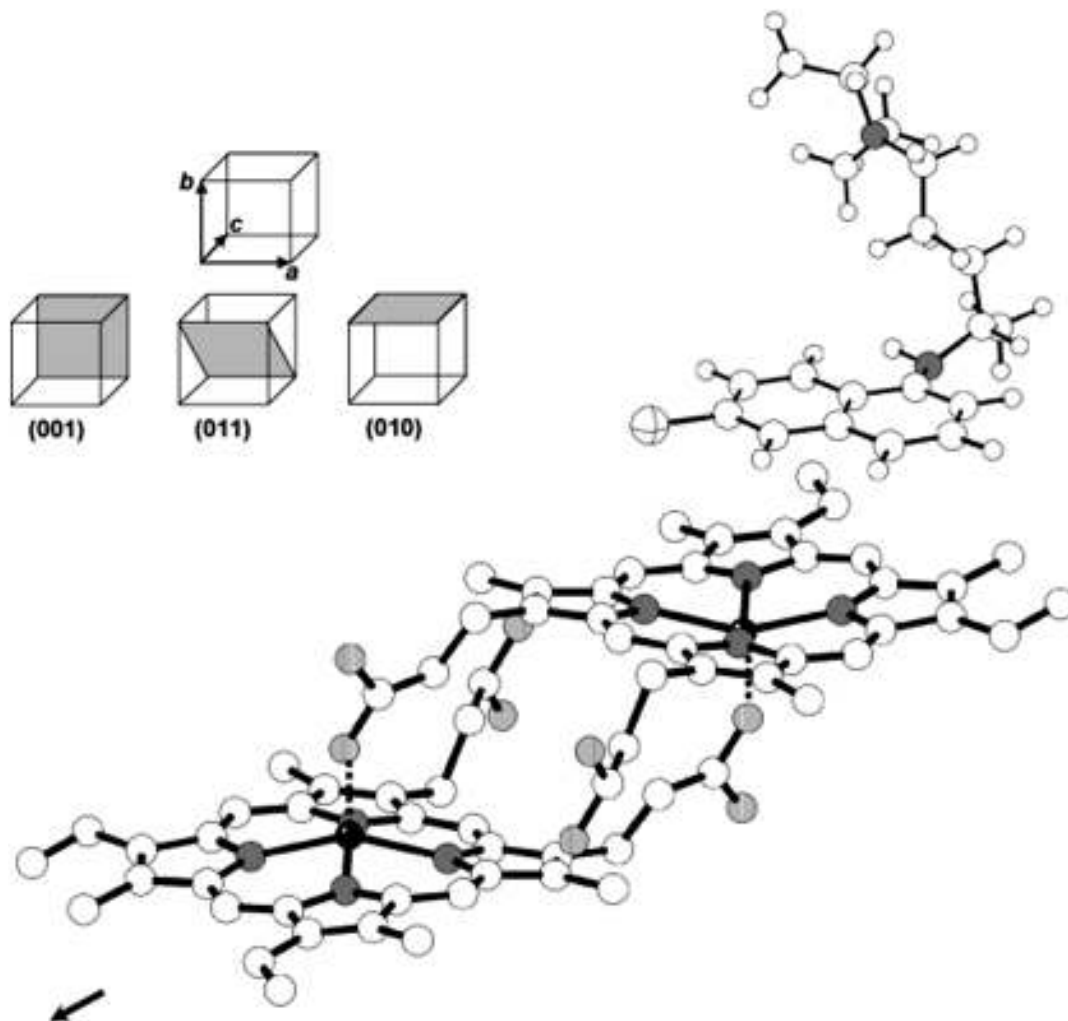


Figure 3. Hemozoin-chloroquine interaction model. Current understanding of Chloroquine mode of action centers on its interaction to the $\{001\}$ and $\{011\}$ faces of heme as well as π - π stacking at the $\{010\}$ face.(45) A chloroquine molecule complex to each axial face of a Fe(III)PIX molecule, preventing crystal extension.

Chapter II

NEUTRAL LIPID MEDIATION OF HEMOZOIN FORMATION

Lipids have been implicated in the formation of hemozoin. Bendrat and colleagues initially speculated that this process is mediated by lipids when they observed that an acetonitrile extract of *P. falciparum* promoted the formation of beta-hematin. The dramatic increase in lipid content of the infected erythrocyte (70-74) and observations of hemozoin localization in close proximity to neutral lipid bodies (NLBs) (57, 75) have directed investigations of hemozoin formation towards neutral lipids. Specifically, triacylglycerol (TAG) and diacylglycerol (DAG), lipids traditionally important for membrane biogenesis and energy storage, are synthesized by *Plasmodium falciparum* and packaged into NLBs in a stage-specific manner within the DV (72, 73, 76). In contrast, these lipids are barely detectable in uninfected erythrocytes (70, 74). This observation was corroborated by recent finding in helminth *Schistosoma mansoni* that hemozoin are localized at neutral lipid droplets (13, 14, 77). However, the function of NLBs during parasite growth remains unclear. Two popular hypotheses include NLBs functioning as a depot of lipid intermediates that are generated during digestion of phospholipids (76) and NLBs serving as a deposit of lipid components that can be quickly mobilized to supply the growing parasite with fatty acids and acylglycerols for membrane generation (73). Of significance, the *P. falciparum* NLB composition was reported as a specific blend of mono- di- and triacylglycerols present in the DV is sufficient for mediating hemozoin formation. Mass spectrometry identified the components of these lipids to be the monoglycerides monostearoylglycerol (MSG) and monopalmitoylglycerol (MPG) and the diglycerides 1,3-dioleoylglycerol (DOG), 1,3-

dipalmitoylglycerol (DPG) and 1,3-dilinoleoylglycerol (DLG) in a 4:2:1:1:1 ratio(57). This biological composition is referred to as the “lipid blend.”

Recently, biologically realistic half-lives of about 5 minutes at 37 °C were reported for beta-hematin formation in a lipid-water interface model (58), suggesting that the interface may play an essential role during heme crystallization. The question remains, how does the lipid-water interface facilitate hemozoin formation? In an attempt to address this question, we evaluated the hypothesis that neutral lipid bodies are the biological mediator of hemozoin formation within the digestive food vacuole of the parasite. In part I of this chapter will investigate the organization of model neutral lipid (MSG and MPG). In addition, the ability of MSG/MPG lipid bodies to facilitate beta-hematin formation was examined.

In the second part, synthetic neutral lipid bodies (SNLB) composed of the lipid blend were utilized to investigate the localization and partitioning of heme into the lipid bodies. Differential scanning calorimetry and kinetic measurements demonstrate that the lipid blend provides a unique environment for hemozoin formation. By observing the collisional (Stern-Volmer) quenching of Nile Red (NR) fluorescence, confocal microscopy and conventional fluorescence spectroscopy reveal that soluble Fe(III)PPIX spontaneously localizes to the SNLBs and partitions into SNLBs in a pH-dependent manner. In conjunction with the known pattern of LB proliferation, it is speculated that NLBs within the DV are not only the location of *in vivo* hemozoin formation, but are also essential for the survival of the parasite by functioning as a time and site specific mediator for heme detoxification. The work presented in this chapter is the result of collaborative work with Dr. Timothy Egan (University of Cape Town(UCT), South Africa), Dr. Katherine De Villiers (University of Stellenbosch, South Africa), Dr. Kanyile Ncokazi (UCT), Rebecca Sandlin (Vander

Experimental Methods

Materials

All materials used were of analytical grade or of the highest grade of purity available from commercial suppliers. Stock solutions made from citric acid purchased from Merck were used to prepare citrate buffer (50 mM) and pH adjusted to 4.8 using a slurry of sodium hydroxide (NaOH). A stock solution (3.2 mM) of hematin was formed by dissolving 2 mg of hematin in 0.4 mL NaOH (0.1 M) followed by the addition of 0.6 mL of 1:9 acetone/methanol. The following lipids were used in this study: monoglyceride lipids *rac* 1-monopalmitoylglycerol (MPG), *rac* 1-monostearoylglycerol (MSG), *rac* 1-monomyristoylglycerol (MMG) and *rac* 1-monooleoylglycerol (MOG); diglycerides 1,3-dioleoylglycerol (DOG), 1,3-dipalmitoylglycerol (DPG) and 1,3-dilinoleoylglycerol (DLG); triglycerides trioleoylglycerol (TOG) and trimyristoylglycerol (TMG); and cholesterol (CHL). All lipids used in this study were obtained from Sigma-Aldrich South Africa. 3.3 mM solutions of lipids were prepared in 1:9 acetone/methanol solvent. In order to carry out a reaction, 200 μ L of lipid solution was pre-mixed with 2 μ L of hematin solution and was layered on the surface of the citrate buffer (5 mL) which was pre-incubated at 37 °C.

The lipid blend refers to the established biological ratio of 4:2:1:1:1 of MSG:MPG:DOG:DLG:DPG reported by the Sullivan group. Each lipid was dissolved in a 9:1 ratio of methanol: acetone to promote lipid solubility. Stock solutions of lipids for lipid blend experiments were prepared at 16.2 mM. A 20 μ M stock solution of Nile Red (MP Biomedicals, LLC or Sigma-Aldrich South Africa) was prepared in acetone and used immediately.

Characterization of neutral lipid bodies

When a solution of neutral lipid is deposited onto an aqueous surface, a monolayer of lipid is formed at the surface. The selectively fluorescent, hydrophobic phenoxazone dye, Nile Red(78) was used to characterize the organization of lipid molecules dispersed in the solution beneath this surface monolayer. 200 μL of stock MPG solution was layered on top of a 5 mL solution of citrate buffer (50 mM, 37 $^{\circ}\text{C}$) drop-wise using a microsyringe. After 5 min. incubation, 2 μL of a 500 $\mu\text{g}/\text{mL}$ Nile Red stock solution was introduced to the surface. Samples were then withdrawn from beneath the surface and placed on a glass slide for imaging by a Nikon Epifluorescent microscope and a Zeiss LSM 510 meta inverted confocal microscope. Confocal imaging was performed using a 488 nm argon laser with 505-550 nm band pass filter. Confocal orthogonal projection was produced using Zeiss LSM Image Browser software. Another 2 μL of the sample was stained with a 2 % solution of uranyl acetate for imaging using a JEM 1200EXII TEM operated at 120 kV. The same experiment was repeated for the lipid blend. The size distribution of the lipid (MPG) emulsions were measured using two Malvern particle sizing systems: The Malvern Zetasizer with a lower limit of 0.1 nm and an upper limit of 6 μm and the Malvern Mastersizer with a lower limit of 50 nm and upper limit of 800 μm . 1 mL of MPG stock solution was deposited onto surface of citric acid buffer (50 mL, 50 mM, pH 4.8) and 0.5 mL samples extracted from below the surface were used for Zetasizer measurements while 2 mL samples were used for the Mastersizer. Three measurements were taken for each sample at 0, 20, 40, and 60 minutes after the lipids were deposited to determine the stability of the size distribution of the lipid bodies in these emulsions with time.

Localization of heme (Fe (III)PPIX)

Hematin was dissolved in 0.1 M NaOH and then mixed with an acetone/methanol (1:9 v/v) solution to form a 2 mg/mL stock solution (3.2 mM) of Fe(III)PPIX (from here on generically referred to as heme). 3.3 mM lipid solutions of MPG and MSG were prepared as described above, except that the ratio of acetone (acetone/methanol) was increased for MSG to ensure that the lipid had dissolved completely. 2 μ L solution of heme and 200 μ L of lipid were mixed. This premixed solution was introduced, as previously described, onto the surface of citric acid buffer solution (5 mL, 37 °C, pH 4.8) in a 15 mL conical tube (Falcon, diameter = 46.87 mm). To determine the localization of heme with respect to the lipid bodies, samples were taken immediately from beneath the layered surface and prepared for transmission electron microscopy imaging using a LEO 912 transmission electron microscope. Additional samples were withdrawn after ten minutes of incubation at 37 °C. Iron distribution was measured from the latter sample on objects that mirrored the structures of beta-hematin crystals using TEM electron spectroscopic imaging (ESI) for elemental analysis of iron.

Characterization of beta-hematin

A scale up version of the above setup was performed 24 times using MPG and MSG for product characterization. Beta-hematin formed in the lipid-water system was characterized by Fourier transformed infrared (FTIR) spectroscopy of undried material as Nujol mulls. Powder X-ray diffraction (XRD) of the extensively washed (5% pyridine solution) dried product, and transmission electron microscopy imaging of samples removed directly from MSG-lipid interface were also performed. XRD was carried out using Cu K α radiation ($\lambda=1.541$ Å), with data collection on a Philips PW1050/80 vertical goniometer in the 2θ range 5 – 40° using an Al

sample holder. TEM images were obtained using the LEO 912. Heme incubated in the aqueous medium alone served as control. Lattice spacings were measured from images obtained from a Philips CM20 transmission electron microscope (TEM).

The role of OH and C=O groups in nucleating beta-hematin.

Experiments at pentanol and octanol/aqueous interfaces were carried out exactly as described previously (58) using 10 mL of the solvent. The experiment with toluene was conducted in the same way except that toluene was substituted for pentanol or octanol. In the case of docosane a 1.9 mg/mL stock solution was prepared by dissolving 1.9 mg in 1.0 mL of a solution containing 1:3:6 acetone:chloroform:methanol (v/v), while for methyl laurate a 2.61 mg/mL stock solution was prepared to volume in a 1.0 mL volumetric flask by dissolving 3 μ L of neat methyl laurate (0.869 g/mL) in 1:9 acetone:methanol solution. 2.0 mg hematin was dissolved in 1.2 mL of 0.1 M NaOH in a 10 mL glass vial. After complete dissolution of the solid, 1.8 mL of the 1:9 acetone:methanol solution was added and the new solution was thoroughly mixed to give a final concentration of 0.67 mg/mL. This solution was prepared fresh for each individual experiment.

Experiments were carried out in Schott Duran crystallising dishes with an internal diameter of 5 cm in the case of pentanol, octanol and toluene and 9 cm in the case of docosane and methyl laurate. 50.0 mL of citrate buffer was measured into each vessel and incubated with a pentanol, octanol or toluene layer on top of the aqueous solution. In the case of the other two, the aqueous layer was pre-incubated at 37°C while docosane, methyl laurate and heme solutions were prepared. On average this process took 15 – 20 minutes. These organic liquids are all largely insoluble in aqueous medium and the solvent system used to dissolve docosane showed a

tendency to precipitate heme at high concentrations. Thus it was reasoned that premixing any of them with the heme/NaOH solution would not produce a sensible result and so the interface was prepared with no premixing. The non-aqueous layer was spread over the surface of the citrate buffer. Subsequently, 0.5 mL (0.33 mg) of heme solution was added drop-wise to the pre-incubated interface using a syringe with a needle diameter of 0.5 mm. Once heme had been delivered to the interface, the experiments were left to incubate for 30 minutes. Control experiments in the presence and absence of MMG were carried out at the same time. At the end of the incubation period the surface was agitated to force all the heme products (both unconverted heme and beta-hematin) to precipitate into the acidic bulk medium. The total volume of solvents and precipitate (~ 50.5 mL) was transferred to an 85 mL Nalgene centrifuge tube and centrifuged at 10,000 rpm for 10 minutes. The clear supernatant was discarded and the pellet kept for further analysis. 1.0 mL of a pyridine:water:acetone solution (1:17.9:5.5 pH 7.5) was added to wash the pellet. In the case of methyl laurate, the supernatant remaining after a second centrifugation was subsequently diluted (40:1960 μ L) and the absorbance measured at 405 nm to quantify the unreacted hematin. The remaining pellet from docosane and methyl laurate experiments was analysed as a nujol mull by FT-IR.

Beta-hematin formation via methods of extrusion

A premixed solution of MPG (1 mL, 3.3 mM) and hematin (10 μ L, 3.2 mM) was adjusted to pH 7.0 with 0.01 M hydrochloric acid (HCl). Citric acid buffer (~300 μ L, 50 mM, pH 7.0) was carefully added to this solution, to avoid precipitation of the lipid solution. MPG/heme vesicles were formed by extrusion through Nucleopore track-etch polycarbonate membranes (Avanti Polar Lipids Inc.) 19 times at temperature above the T_c . The newly formed heme-MPG

lipid emulsions were introduced into an aqueous solution buffered at pH 4.8 containing 50 mM citrate. The mixture was incubated at 37 °C for about 10 minutes and TEM imaging of 3 μ L of samples was taken using the LEO 912 electron microscope. This experiment was repeated for MSG.

Kinetic studies of beta-hematin formation

Kinetics for the following lipids were examined: monoglycerides MPG, MSG, and MOG; diglycerides DOG, DPG, and DLG; triglycerides TOG and TMG; and CHL. The experimental setup was as described above. Briefly, premixed solution was formed using 2 μ L of heme and 200 μ L of lipid stock solutions and was layered onto citric acid buffer. The mixture was incubated at 37 °C for 0, 1, 3, 5, 15, 30, 45 and 60 minutes. Each time point was performed in triplicate. The reaction was quenched with the addition of 1 mL of an aqueous solution containing 30% pyridine, 10% HEPES buffer (2.0 M, pH 7.5), and 40% acetone (v/v). The sample was immediately centrifuged for 10 minutes at 4,000 rpm. The percentage of unconverted heme was determined by performing colorimetric measurements at 405 nm on the supernatant of quenched and centrifuged samples. This is a modification of an assay published and confirmed by Ncokazi and Egan (58, 79).

The effect of temperature on kinetics of beta-hematin formation

For temperature analysis of beta-hematin formation in the lipid-water system, measurements of percentage of heme conversion were conducted at 25, 30, 40, and 50 °C. A premixed solution of 200 μ L MSG and 2 μ L heme stock solution was deposited onto a citric acid buffer (50 mM, pH 4.8) sub-phase at designated temperatures. The reaction was quenched and

colorimetric measurements were performed as described above at various time points. Half life, $t_{1/2}$ was calculated using Prism 4©. Rate constants were calculated from $t_{1/2}$ values and were applied to the Arrhenius plot to determine activation energy, A_e using the Arrhenius equation.

$$k = Ae^{-E_a/RT}$$

where k is the rate constant, A is the pre-exponential factor, T is the temperature (Kelvin), and R is the gas constant.

The effect of pH on kinetics of beta-hematin formation

In order to examine the effect of pH on beta-hematin formation at the lipid-water interface, the pH of the aqueous solution on which the lipid solution was deposited was adjusted to 0.5, 1.0, 2.0, 2.5, 3.0, 3.5, 4.0, 4.5, 4.8, 5.0, 5.5, 6.0, 6.5 and 7.0 at 37 °C. The method is as described previously. After 1 hr of incubation the reaction was quenched with pyridine solution and the beta-hematin percentage yield was recorded by means of colorimetric measurements at 405 nm.

Fe(III)PPIX localization and partitioning into SNLB

Fluorescence spectra of NR were recorded in acetone as a function of concentration in order to determine the linear range of intensity versus concentration. A series of fluorescence spectra were also recorded in different solvents so as to observe the dependence of λ_{em} (max) on polarity. To observe the effects of Fe(III)PPIX on NR fluorescence, a 100:1 solution of lipid: NR was prepared with a final concentration in buffer at the desired pH of 100 μ M lipid and 1.0 μ M NR. Buffers used were 0.020 M HEPES (pH 6.0 – 8.0) or citric acid/citrate (pH 2.8 – 5.5). A 1 mL aliquot of NR-labeled SNLB dispersed in aqueous medium was placed in a quartz fluorescence cuvette and titrated with Fe(III)PPIX prepared by dissolving hematin in 0.1 M

NaOH. The fluorescence spectrum was measured on a Varian Cary Eclipse fluorescence spectrophotometer. Both excitation and emission slit width's were set to 5 nm with a medium scan control and medium PMT detector voltage. The sample was excited at 540 nm and the emission spectrum was recorded from 560-800 nm.

Data were analyzed according to the Stern-Volmer equation (equation 1):

$$\frac{I_0}{I} = 1 + K_{SV}[Q] \quad (1)$$

where I_0 is $\lambda_{em}(\max)$ in the absence of the quencher, I is the observed $\lambda_{em}(\max)$ in the presence of a given concentration of quencher, K_{SV} is the Stern-Volmer quenching constant and $[Q]$ is the concentration of the quencher, in this case Fe(III)PPIX.

Partitioning of Fe(III)PPIX between aqueous solution and octanol was measured at pH 7.51 using HEPES buffered aqueous solution (0.020 M). Fe(III)PPIX was prepared from hematin in 0.1 M NaOH and then introduced into the buffer at a final concentration of 57.8 μM . This was shaken and equilibrated for 6 h at 37 °C with an equal volume of octanol. At the end, the UV-visible spectra of the aqueous and octanol layers were measured on a Varian Cary 100 spectrophotometer at 403 nm.

Confocal imaging of heme localization

For confocal microscopy measurements, the 16.2 mM lipid blend solution was prepared using stocks in a 4:2:1:1:1 volume ratio. A 100:1 solution of lipid: NR was prepared by combining 150 μL NR stock with 18.5 μL of lipid blend stock. This solution was briefly vortexed and diluted with a 50 mM solution of citric buffer (pH 4.8) to give a final volume of 1 mL. This solution was again briefly vortexed, giving a final lipid concentration of 300 μM and Nile Red of 3 μM . A lipid volume of 180 μL was imaged in a glass bottom microwell dish

(35mm Petri dish and 14 mm microwell dish, MatTek Corporation). A 500 μM Fe(III)PPIX solution was prepared for quenching of the NR signal as described above. Quenching was performed by sequentially adding 20 μL of the Fe(III)PPIX solution every ~ 30 seconds, starting 10 seconds into imaging, until complete quenching was observed. Great care was taken to not displace the lipid bodies. Measurements were made using a Zeiss LSM 510META upright confocal microscope (VUMC Cell Imaging Shared Resource) using the time series application with 63 \times oil (1.4) immersion objectives. Z-stacking was performed before and after quenching to ensure lipid bodies were not displaced during the experiment. The quenching experiment was repeated with the exception of introducing 400 μL of 250 μM Fe(III)PPIX at once (10 seconds into imaging). The quenching experiments were repeated for citric buffer adjusted to pH 1.3, 2.3, 4.8, 5.5, 6.7, 7.3, and 8.1. The rate of photobleaching was measured by imaging the fluorescence intensity of NR-labeled SNLBs without the presence of heme for 200 seconds. The experiment was repeated for pH 4.8 with the addition of 140 μL Fe(III)PPIX.

Differential scanning calorimetry (DSC)

Thermal analysis (TA) of neutral lipid samples encapsulated in sealed aluminum capsules were conducted with a TA instrument DSC Q200. Approximately 2.4-3.2 mg samples of each lipid were weighed with a microbalance and analyzed from a temperature of 80 $^{\circ}\text{C}$ to -80 $^{\circ}\text{C}$ at a cooling rate of 10 $^{\circ}\text{C}/\text{min}$ and a heating rate of 15 $^{\circ}\text{C}/\text{min}$. The exothermic and endothermic peaks were determined by plotting heat flow (adjusted for weight) vs. temperature.

Results and Discussion

Part I: Beta-Hematin Formation at the Interface of MSG/MPG Model Lipid Bodies

Part II: Heme Partitioning into Synthetic Neutral Lipid Bodies (SNLB) and the Mediation of Beta-Hematin Formation by SNLB

Part I: Beta-Hematin Formation at the Interface of MSG/MPG Model Lipid Bodies

Characterization of neutral lipid bodies

Studies of lipid mediation of beta-hematin formation have demonstrated rapid heme conversion when hematin was introduced to a solution of rac 1-monomyristoylglycerol (MMG) that was deposited onto an aqueous subphase (58). By contrast, previous crystallization studies using only a monolayer of the phospholipid dipalmitoylphosphatidyl-choline (DPPC) reported the insufficiency of the lipid monolayer to mediate beta-hematin formation, even after 24 h of incubation (80). Instead, when an aged bulk solution of lipid was substituted, beta-hematin crystals were detected. Together, these data point to an unknown lipid mediated heme conversion process that exists beneath the surface monolayer which produces most if not all of the beta-hematin. Little is known about the organization of these lipids beneath the surface. To investigate the distribution of neutral lipids in this system, transmission electron microscopy (TEM) and fluorescent imaging were performed on samples extracted from just beneath the surface. Imaging data suggest that lipids spontaneously organize into a lipid emulsion beneath the surface (Figure 4a, b). Fluorescence imaging of samples stained with the lipophilic stain, Nile Red, and a water

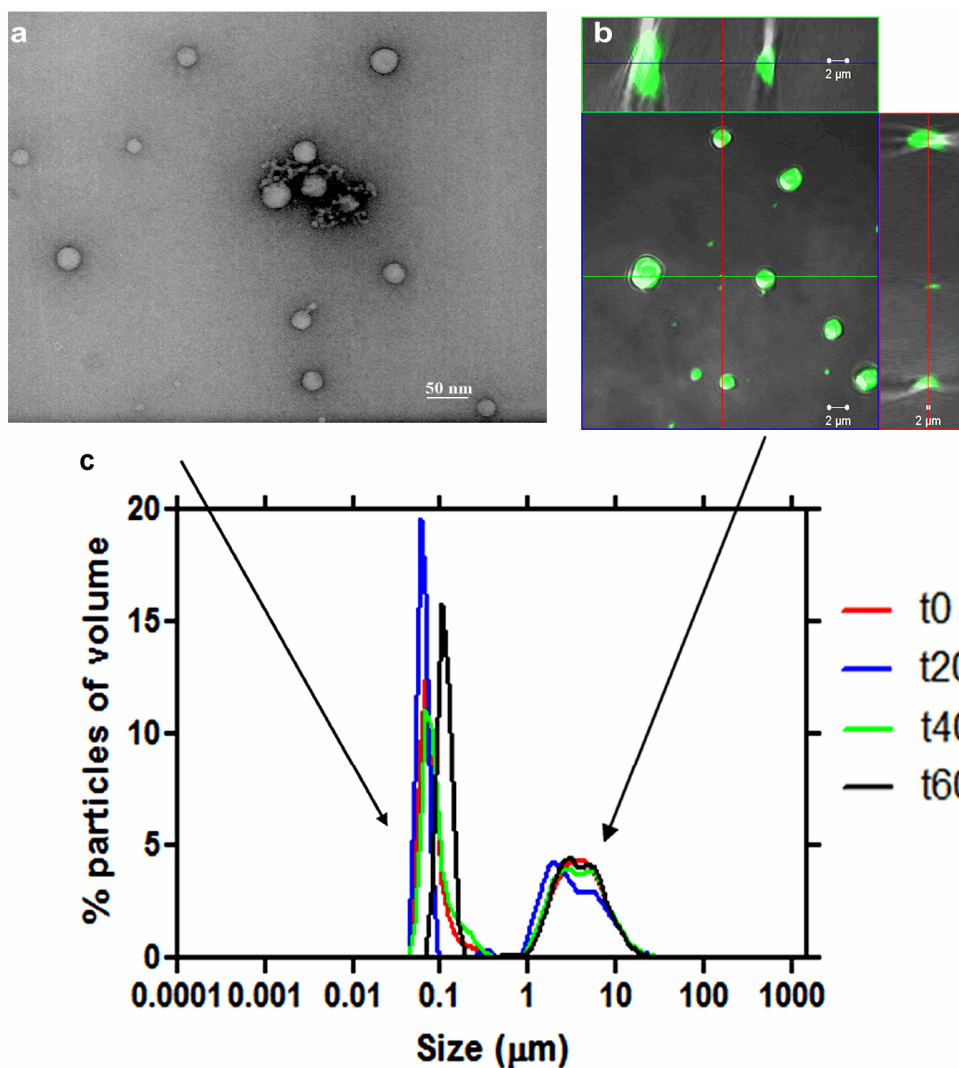
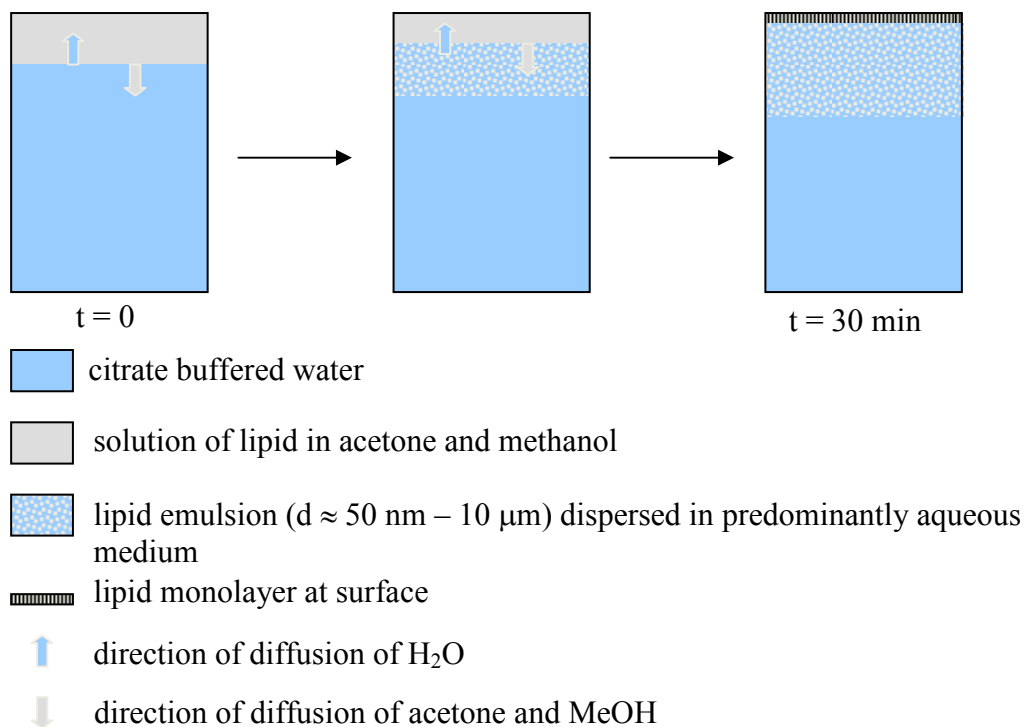


Figure 4. Characterization of monopalmitoyl glycerol in acetone/methanol solution after deposition onto an aqueous surface. Samples were extracted from just beneath the surface. TEM images show lipid bodies in the nanometre size range (a), while fluorescence imaging of samples stained with the lipophilic stain, Nile Red (orange), and the water soluble dye, fluorescein (green), show bodies in the micrometer size range (b). Measurements of lipid particle size distribution reveal two populations, one in the range 50 – 200 nm and the other 1 – 10 μm . This size distribution remained stable over a period of an hour (c). Confocal orthogonal projection confirms that lipid bodies are not hollow, but rather continuous throughout their interiors (d).

soluble dye, fluorescein, showed lipid bodies in the emulsion layer in the micrometer size range (Figure 4b), while TEM imaging showed structures in the nanometre size range (Figure 4a). Confocal microscopy of the samples confirmed that the lipid bodies contain a homogeneous core (Figure 4d) and are not hollow liposomes. Measurements of the particle size distribution in these lipid emulsions revealed two populations. A large population in the 50 to 200 nm diameter range (Figure 4c) and a smaller population of lipid bodies in the 1 to 10 μm range. These emulsions were stable over time, as little fluctuation in size distribution was observed in four independent measurements over a period of an hour.

Experimental evidence presented here incontrovertibly demonstrates that the remaining lipid forms an emulsion in the sub-phase beneath this monolayer. Furthermore, the sizes of the lipid bodies in this emulsion fall into two populations, one in the low micrometer range and the other in the range 50 – 200 nm. The lipid bodies are not micelles or hollow liposomes, but rather have a “solid” core (i.e. are homogeneous through their interiors) as shown by confocal microscopy of the larger population of bodies. These lipid bodies, which form spontaneously as shown in Scheme 2, are strikingly similar in appearance to neutral lipid bodies reported associated with the digestive vacuole of *P. falciparum* and the gut lumen of *S. mansoni* and which, at least in the case of the former organism have been shown to consist largely of mono-, di- and triglycerides (14, 57, 73, 81). Indeed, they appear to be essentially synthetic counterparts of these lipid bodies.



Scheme 2. Evolution of the lipid emulsion following deposition of a solution on the aqueous surface. A sample of lipid dissolved in 1:9 acetone to methanol solution is deposited onto an aqueous surface. As the environment surrounding the lipid becomes predominately aqueous, the lipids rearrange to form lipid bodies.

Localization of heme and product characterization

TEM imaging showed that when hematin was premixed with MPG and introduced onto an aqueous surface, electron dense material, probably heme, rapidly localized around the surface of the lipid bodies, apparently at or near the lipid-water interface (Figure 5a). Images of samples incubated for 10 minutes showed crystals resembling beta-hematin (Figure 5b). TEM/ESI of iron distribution in these samples confirmed the presence of iron in these putative beta-hematin crystals (Figure 5b). TEM evidence suggests that the heme accumulates near the surface of the lipid bodies. Such accumulation of the amphiphilic heme molecule at the surface of lipid bodies in *P. falciparum* and *S. mansoni* has previously been proposed (57, 73, 81, 82), but this represents the first direct evidence of localization of free heme at the interface of lipid bodies and water. Morphologically, these crystals resemble hemozoin in their crystal habit (Fig. 6c, f). Infrared spectra and powder diffraction data of the products formed using MSG and MPG clearly demonstrates the production of beta-hematin with percentage of product conversion of 75 ± 2 and 65 ± 4 , respectively (Fig. 7a). Prominent IR peaks at 1662 cm^{-1} and 1210 cm^{-1} are readily discernible indicating significant formation of beta-hematin (Fig. 6a, d). These findings are confirmed by XRD (Fig. 6b, e) showing the characteristic diffraction peaks of beta-hematin. The diffraction pattern of the product formed with MSG in particular, definitively demonstrates the presence of beta-hematin. Subsequent formation of beta-hematin has been unequivocally demonstrated in this work by FTIR spectroscopy and powder XRD. TEM also demonstrates the formation of crystals identical in habit to hemozoin. In contrast to current results, previous studies by Sullivan and co-workers reported MSG as ineffective in promoting beta-hematin (57). This result may be owing to its low solubility. By employing a 1:9 acetone/methanol mixture pre-incubated at $37 \text{ }^\circ\text{C}$, MSG was effectively solubilized. Though this does not directly mimic

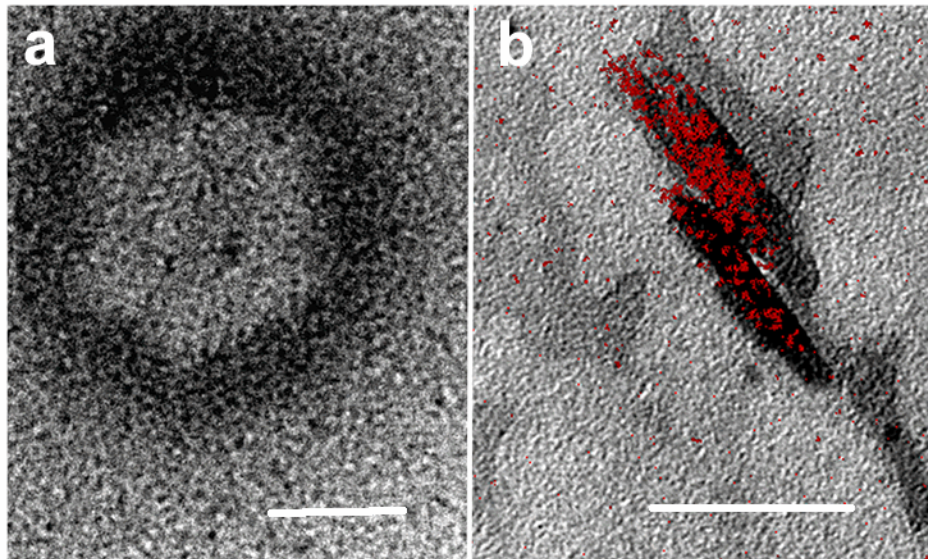


Figure 5. TEM image of heme localized at or near the lipid-water interface. When hematin was premixed with MPG and introduced onto an aqueous surface and immediately imaged using TEM, electron dense materials, presumably hematin was localized at or near the lipid-water interface (a). Elemental imaging of iron using TEM with electron spectroscopic imaging (ESI) conducted on samples reacted for 10 min. confirmed the presence of beta-hematin crystals (b). Regions highlighted in red denote the presence of iron (Fe). Scale bar = 50 nm.

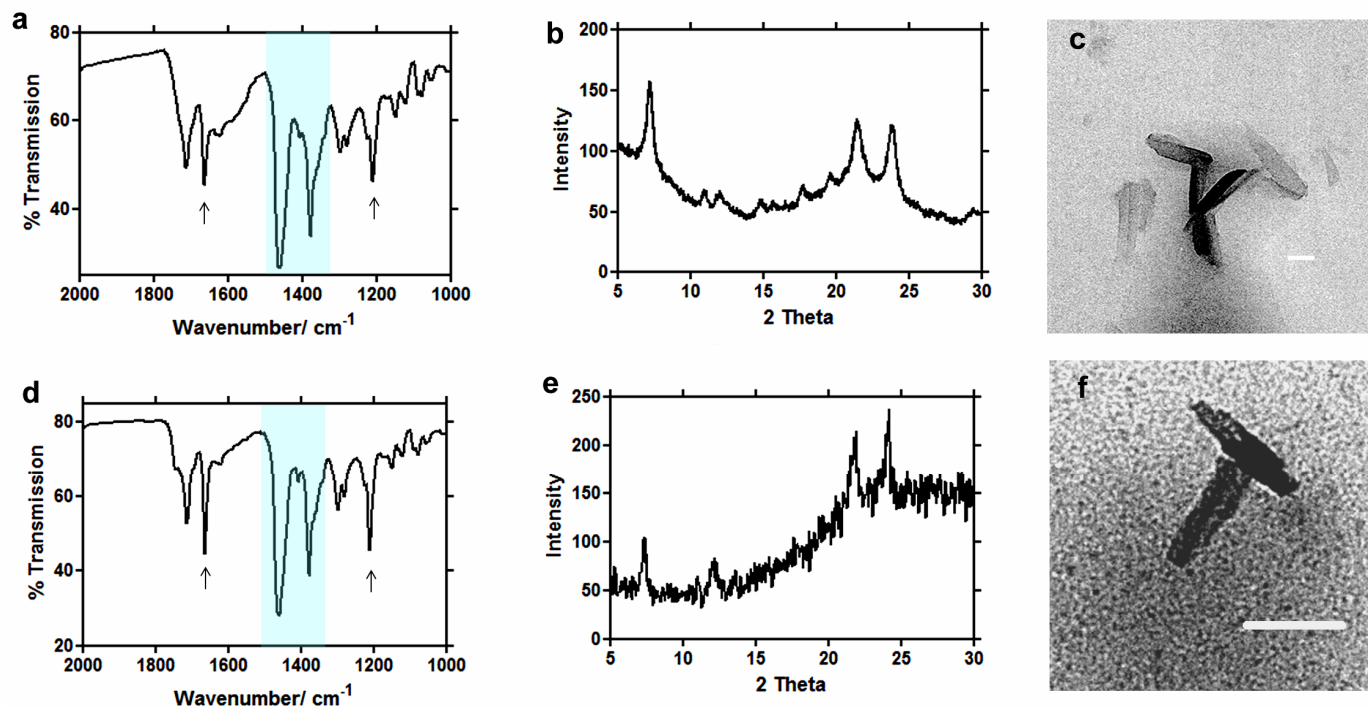


Figure 6. Infrared (IR), X-ray diffraction (XRD), and transmission electron microscopy (TEM) evidence for the formation of beta-hematin at the lipid-water interface using MSG (a, b, c), and MPG (d, e, f). Two large Nujol peaks (a, d) obscure the region between 1550 and 1320 cm^{-1} but do not interfere with the characteristic beta-hematin IR peaks at 1660 and 1210 cm^{-1} (42). Both products formed under mediation of MSG (a) and MPG (d) show IR characteristics of beta-hematin. XRD of products obtained in presence of MSG (b) and MPG (e) show patterns characteristic of beta-hematin (41). TEM images of these products closely resemble hemozoin in their crystal habit (c, f). Scale bar = 50nm.

the physiological process, it is necessary in order to introduce the lipid and heme to the interface in a soluble form so as to promote beta-hematin crystallization, probably promoting lipid droplet formation and preventing precipitation of unconverted heme.

Beta-hematin nucleation and extension

To examine the role of the hydrophilic head group during nucleation, percentage heme conversion was examined in the presence of various mediators. Octanol and pentanol resemble neutral mono- and diglyceride lipids in having OH head groups and aliphatic chains. Docosane, $\text{CH}_3(\text{CH}_2)_{20}\text{CH}_3$, and methyl laurate, $(\text{CH}_3)\text{-O-C(=O)-}(\text{CH}_2)_{10}\text{CH}_3$, lack OH groups while methyl laurate, but not docosane, contains C=O groups. Toluene can π -stack with heme, but lacks either chains or polar head groups. These solvents were therefore proposed as good substitutes for lipids in order to probe the role of the terminal OH groups, C=O groups and π -electron containing groups in nucleating beta-hematin. In the presence of the hydroxyl (-OH) group, such as in the case of octanol and pentanol, a percentage of beta-hematin formation comparable to that mediated by monoglyceride was found, 83% and 95%, respectively (Figure 8b). This percentage was reduced by nearly half (40%) when the ester methyl laurate was substituted (Figure 8. 5a). However, under the mediation of a long chain alkane, docosane, which mimics the alkyl chain of the lipid, but lacks the hydrophilic head group, no product was detected. Interestingly, toluene as a mediator produced 42% conversion to beta-hematin (Figure 8a).

The lipids used in this study all contain carbonyl (C=O) head groups, while mono- and diglycerides also contain hydroxyl (OH) head groups. These lipids pack together by virtue of interactions between their polar head groups (30). As each additional is esterified in going from mono- to di- to triglycerides the polarity of the head group is reduced (83, 84). In

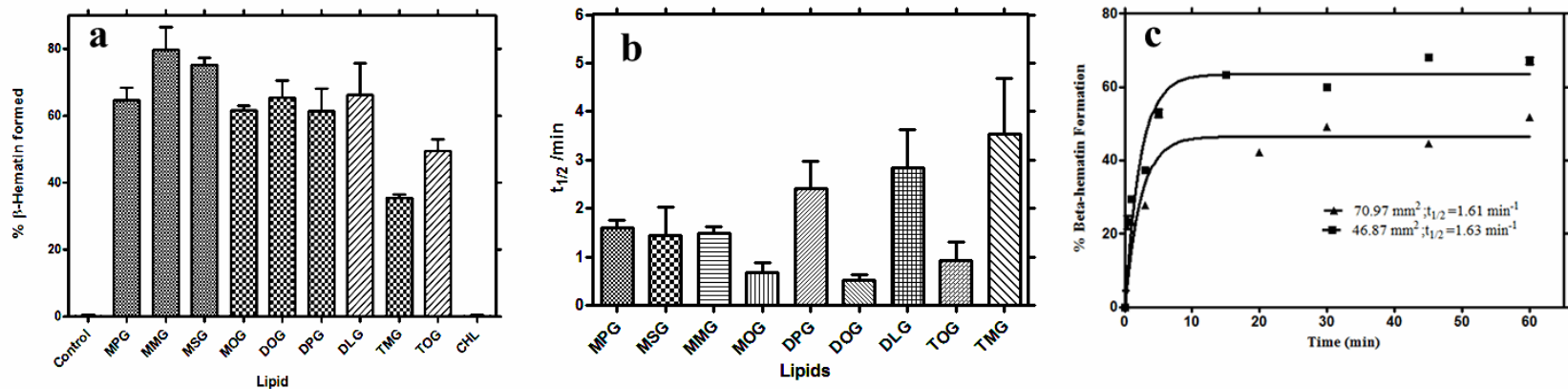


Figure. 7 Beta-Hematin formation using various neutral lipids. The percentage of beta-hematin formation was measured for premixed solutions of hematin and lipid deposited onto an aqueous solution. Mono- and diglycerides exhibited about the same efficiency in mediating beta-hematin formation, while the triglyceride mediated reaction resulted in less product. The control reaction in which heme was incubated in the aqueous medium alone produced no product (a). No statistically significant difference was observed in the rate of beta-hematin formation for these lipids, except for MOG and DOG which are significantly faster than the others (b). This rate did not change when the surface area of the experimental vessel was increased for MSG (c); however, a reduction in the percent yield was observed in reactions performed in a vessel with a 71 mm² surface area ($t_{1/2} = 1.63$ min; 47% yield) compared with that with a 47 mm² surface area ($t_{1/2} = 1.61$ min; 63.8 % yield).

Langmuir-Blodgett films in which the alkyl chains are positioned towards the air and the head groups interact with the aqueous solution, lateral compression of diglycerides reports a collapse pressure of 25 – 35 mN/m, significantly higher than that of triglycerides (12 – 14 mN/m). This indicates that the former anchor more strongly in the water phase than triglycerides (85). The higher polarity of mono- and diglycerides is likely to contribute to their efficiency in directing crystal nucleation. These molecules likely self assemble with their polar head groups facing the aqueous layer, presenting OH groups and lone pair electrons which can interact with heme. This is supported by observations with other amphiphilics which indicate that oxygen containing head groups (OH or $-(C=O)-O-$) play a crucial role in beta-hematin formation, since pentanol, octanol and methyl laurate all promote its formation, while no beta-hematin was formed in the presence of docosane. These observations support the proposal of Leiserowitz and colleagues that hemozoin formation occurs at lipid-water interfaces through epitaxial growth (80). Indeed, the role of amphiphilic molecules orienting nucleation of inorganic crystals through structural complementarity and/or lattice epitaxy between head groups of the amphiphile and the later arrangement within the crystal is well established in other systems (86). However, it is also the case that decreasing surface tension plays a role in crystal nucleation, as has been demonstrated by Huy *et al.* for beta-hematin formation in acidic aqueous alcohol solutions using water miscible alcohols (87). The activities of the various amphiphilic solvents used in this study and of the lipids could thus alternatively simply reflect their ability to lower surface tension and warrants future investigation.

TEM imaging of extruded samples of both MPG/heme and MSG/heme solutions showed beta-hematin formed near the outer region of the lipid bodies (Figure 9). In all observations, crystal size did not exceed dimensions of associated lipid bodies. Clusters of beta-hematin

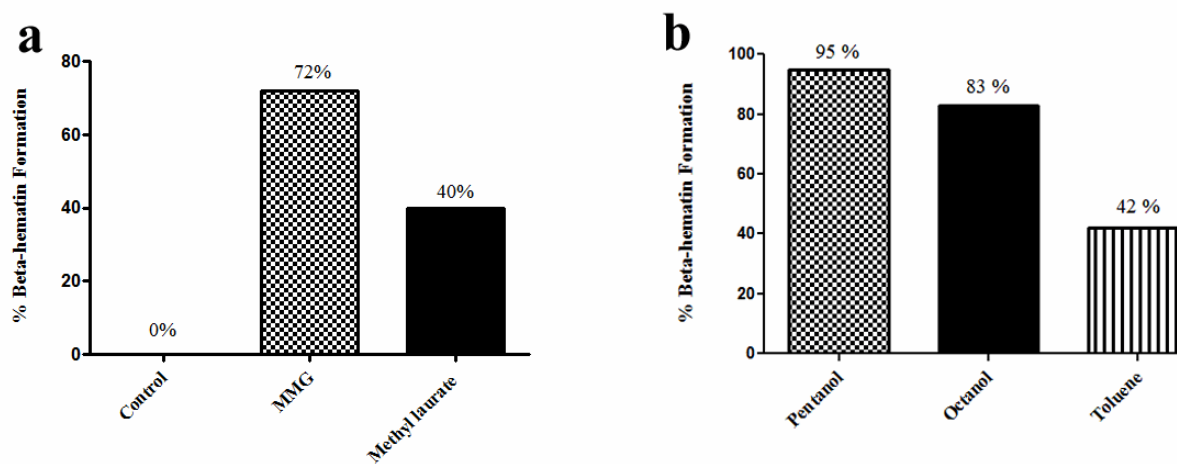


Figure 8. Comparison of efficiency of lipids, solvents and amphiphiles in forming beta-hematin at the interface with aqueous solution (pH 4.8, 37 °C). Comparison of MMG, methyl laurate and a control in which heme is spread on the surface of the aqueous medium in the absence of an amphiphilic molecule, measured at 30 min (a). Comparison of organic solvents pentanol, octanol and toluene in a two-phase system with heme introduced at the interface, measured at 30 min (b) were performed to evaluate the roles of hydrocarbon chain length and polar head group during beta-hematin formation.

crystals were observed localized near and aligned parallel to the interface and each other (Figure 9b, c, f, g). In several images, the beta-hematin crystals were located along the lipid-water interface of the lipid bodies (Figure 9a, e). These images closely resemble observations in *P. falciparum* reported by Coppens and Vielemeyer and Pisciotta *et al.* (57, 88), while images of early stages of hemozoin formation in *S. mansoni* also appear to be similar upon close inspection (13). The observations in the current study provide direct evidence that crystal nucleation occurs at the lipid-water interface and that crystal elongation occurs parallel to this interface. Based on the work of Buller *et al.*(45) which relates the shape of beta-hematin crystals to the $\{h,k,l\}$ indices of the crystal, it appears likely that crystal extension occurs parallel to the c-axis until its growth is limited by the curvature of the lipid particle. Thus, the slowest growing $\{100\}$ face is in contact with the lipid surface and the fastest growing $\{001\}$ face is approximately perpendicular to the interface. This arrangement is in agreement with the findings of the recent GIXD and XR study of beta-hematin formation in a premixed MMG/hematin system which showed that the $\{100\}$ face of the crystals is perfectly aligned with the surface of the solution (89). However, in the absence of electron diffraction data in the present study, this remains somewhat speculative. In part II, a more detailed approach to analyze heme localization will be presented.

Kinetic studies of beta-hematin formation

A premixed lipid-hematin solution was introduced onto the aqueous sub-phase. After the designated incubation period, the percentage of beta-hematin formation was measured using a pyridine-based assay. This assay has been described and validated elsewhere (79) . Briefly, the assay is based on the ability of 5% (v/v) aqueous pyridine solution (pH 7.5) to react with

unconverted heme, but not beta-hematin, resulting in the formation of a low spin pyridine-heme complex with a distinctive absorbance at 405 nm and a characteristic orange-pink colour. When the percent yield for the 60 minute time point was compared, similar percentages of heme conversion were measured for mono- and diglycerides while less product was formed using triglycerides (Figure 7a). Interestingly, cholesterol was found to be inefficient at mediating beta-hematin formation. Though there are observed differences between mono- and diglycerides on the one hand and triglycerides on the other in the percentage of heme conversion, the rates of product formation mediated by these lipids were not greatly affected by the lipid. Overall, the reaction was completed within five minutes and a significant quantity of product was formed in less than one minute (Figure 7b). Interestingly, unsaturated glycerides promoted beta-hematin formation more rapidly than saturated glycerides. Nearly a two fold increase in rate was observed for formation of beta-hematin with unsaturated glyceride (MOG, DOG, and TOG) mediation when compared to the rate calculated from saturated glycerides. In the absence of the lipid bodies, no product was formed. Reaction rates were also unaffected by the cross-sectional area of the vessel in which the reaction was conducted.

Model neutral lipid bodies composed of a homogenous sample are competent for the detoxification of free heme at a biologically realistic rate under physiological conditions. Indeed, the observed rates are the fastest so far reported for beta-hematin formation with half-lives of about 0.5 min at 37 °C for the monoglycerides MPG, MMG and MSG and only slightly slower for the di- and triglycerides (DLG, DPG and TMG). If hemoglobin degradation occurs at a constant rate, lipid-water interface mediated hemozoin formation would be more than sufficient to manage the entire flux during the intraerythrocytic stage. The rate of formation is about an

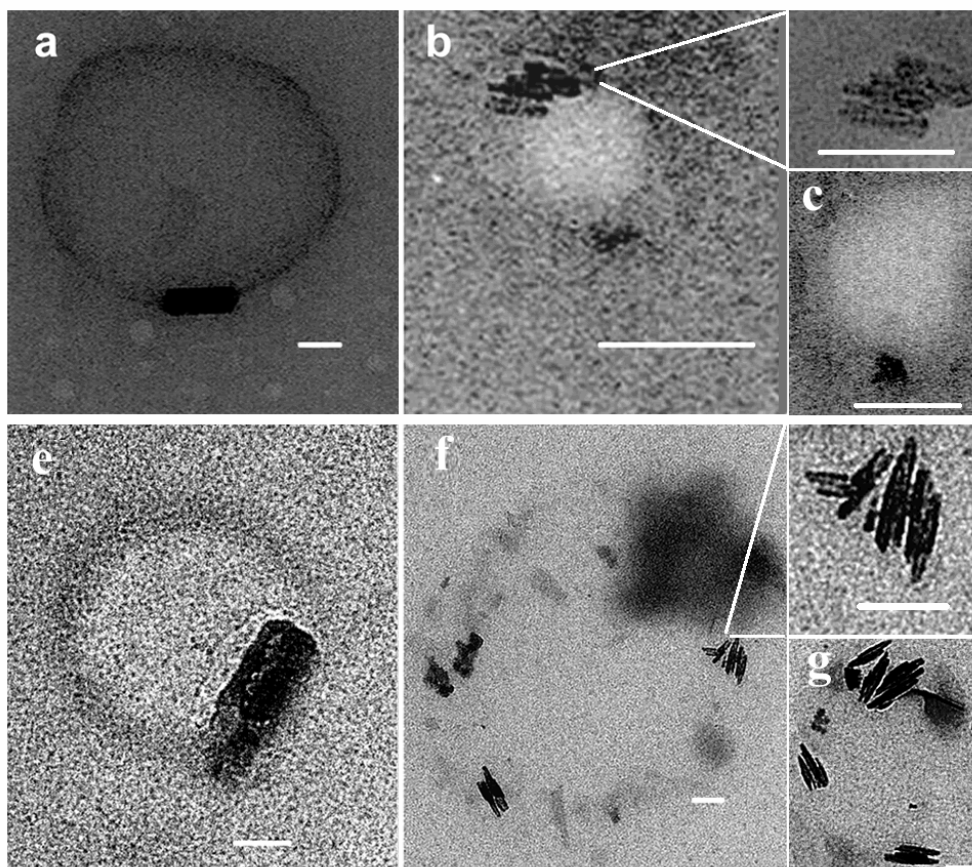


Figure 9. TEM of beta-hematin formed at the MSG/water (a – c) and MPG/water (e – g) interface through methods of extrusion. A lipid and haematin solution was extruded through a fixed membrane filter and then introduced into an aqueous solution containing 50 mM citric acid (pH 4.8, 37 °C). Samples were taken for TEM images after 10 min of incubation. beta-hematin crystals were observed aligned along the lipid-water interface for both extruded samples of MSG (top row) and MPG (bottom row). Clusters of beta-hematin crystals were oriented parallel to each other and to the lipid-water interface (MSG, b, c; MPG, f, g).

order of magnitude faster than that previously reported with the lipid-water system (58). In these previous studies, the heme and lipid solutions were separately introduced to the aqueous interface, whereas in the current work they were premixed. This demonstrates that the method by which heme is introduced to the interface strongly influences the kinetics, and also suggests that the rate of diffusion or transport of heme molecules to the lipid bodies contributes to the efficacy of the biological process. The reaction rates for the different lipids do not vary greatly, but the unsaturated glycerides (MOG, DOG, TOG) promote crystal formation significantly more rapidly than the saturated glycerides. It is possible that unsaturated lipid bodies favor initial interaction of heme and lipid via π -stacking. It is interesting in this regard that while the alkane docosane does not support beta-hematin formation, the aromatic solvent toluene does, albeit less efficiently than octanol and pentanol. This lends support to the notion that a π -system may further promote beta-hematin formation at the interface. It is noteworthy that the unsaturated fatty acid linoleic acid has been reported to increase 40% in parasitized erythrocytes relative to control (71), raising the question of whether it serves as a promoter of hemozoin formation.

pH and temperature dependence of beta-hematin formation

The pH dependence of the percentage of beta-hematin formation at the lipid-water interface after 1 h incubation at 37 °C follows a bell-shaped curve (Figure 10b) with maximal production at pH 4. As the reaction moves away from this optimal pH, the percentage of heme conversion is reduced. No product was detected below pH 2 or above 6. The dependence of yield on pH follows a bell shaped curve, with near optimal formation at the physiological pH of the malaria parasite digestive vacuole (4.8 – 5.2) (20). This pH dependence can be ascribed to the

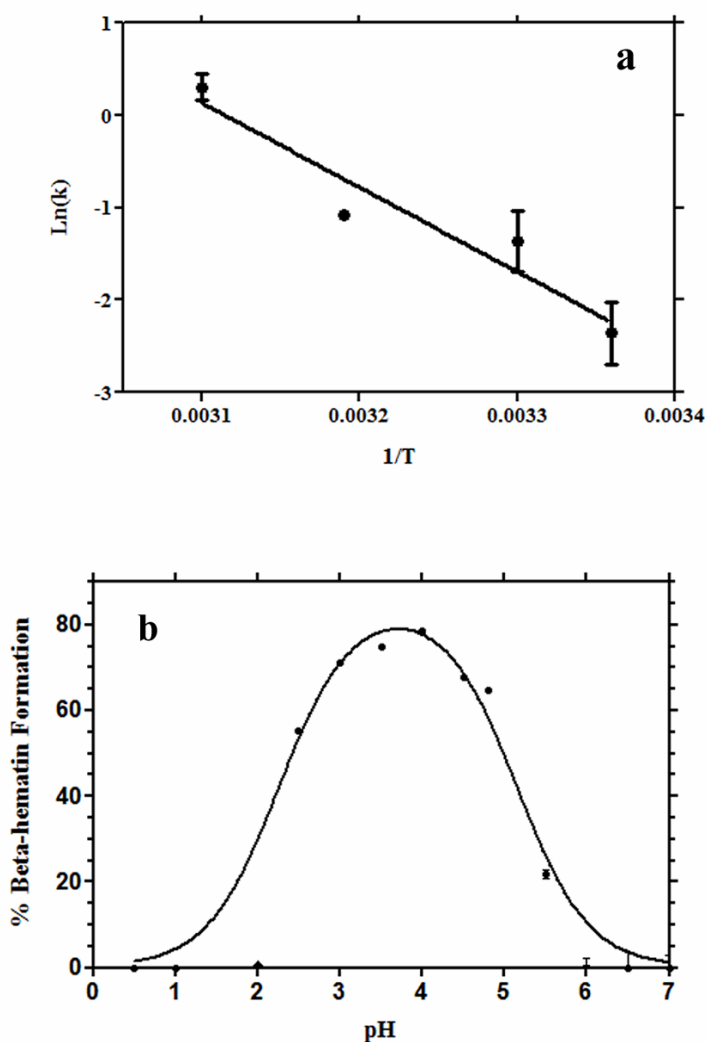
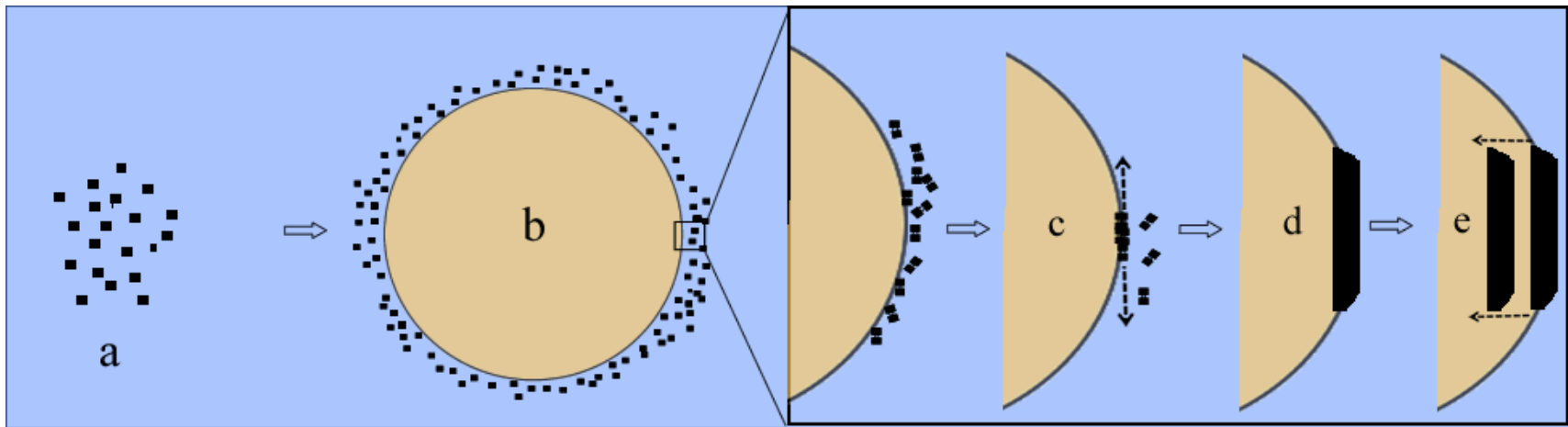


Figure 10. Temperature and pH dependence of beta-hematin formation at the lipid-water interface. The Arrhenius plot (a) was constructed from rate constants (k) measured in an MSG interface system at pH 4.8 and temperatures ranging between 25 and 50 °C. The slope gives an activation energy of 76 ± 16 kJ/mol. The effect of pH (b) was measured at 37 °C and using an MSG interface system. The solid line fitted through the pH data is a best fit to an equation representing two pK_a values with, $\text{pK}_{a1} = 2.3 \pm 0.01$ and $\text{pK}_{a2} = 5.2 \pm 0.01$.

protonation state of beta-hematin itself, in which one propionic acid group is un-ionized, while the other is ionized. At low pH (< 2) both propionic acid groups are un-ionized and beta-hematin formation is abolished, while at high pH (> 6) both are ionized and beta-hematin formation is similarly abolished.

The dependence of the rate of beta-hematin formation on temperature in the MSG/water emulsion was also determined. The Arrhenius plot of $\ln(k)$ vs $1/\text{temperature}$ yielded a negative slope (Figure 10a), suggesting that the assembly of heme dimers is a first order reaction. A first order reaction indicates that the rate of beta-hematin formation depends on the concentration of the reactant. In this case, the rate is likely dependent on the concentration of heme dimers to the first power and not the concentration of lipid or Fe(III)PPIX in solution because the product, beta-hematin, is the result of heme dimer hydrogen bonding to form the macroscopic crystal. Applying the slope of the $\ln(k)$ vs $1/\text{temperature}$ to the Arrhenius Equation resulted in an activation energy of 76 ± 16 kJ/mol (Figure 10a). The activation energy obtained in the lipid water system is a little lower than that for beta-hematin formation in 4.5 M acetate buffer and 50 mM benzoic acid buffer (84 ± 4 kJ/mol), but the difference is not statistically significant. The activation energy for beta-hematin formation brought about by MSG lipid bodies (76 ± 16 kJ/mol) is not significantly different from that reported in acetate or benzoate buffer (84 ± 4 kJ/mol) (90, 91). Thus the much faster rate observed in the lipid system arises from a much bigger pre-exponential factor, consistent with the idea that the interface is involved mainly in preorganizing heme and hence facilitating interactions between heme molecules. When adjusted for concentration of lipid per unit total volume, the concentration of lipid in the lipid-interface system is 384 times less than that of benzoic acid and 34,615 times less than acetic acid. Thus, the lipid particle/water interface is far more active in promoting beta-hematin formation than the



Scheme 3. The proposed mechanism of hemozoin formation. Free heme (a) released as a result of hemoglobin degradation accumulates at the interface of the neutral lipid body within the digestive food vacuole of *P. falciparum* (b). Nucleation occurs at the interface and elongation of the crystal extends along the interface (c) until curvature of the lipid body prevents further elongation of the crystal (d). The hydrophobic nature of the mature crystal (e) favors its transport into the lipid interior leading to a stack of aligned crystals.

Other two systems and meets the requirement for physiologically relevant rates of formation. Its biological counterpart, the neutral lipid body-water interface, is thus likely to be the site of hemozoin formation in biology.

Part II

Heme Partitioning into Synthetic Neutral Lipid Bodies (SNLB) and the Mediation of Beta-Hematin Formation by SNLB

Characterization of synthetic neutral lipid bodies

Most eukaryotic cells contain cytosolic neutral lipid bodies which are hypothesized to participate in energy storage (92, 93). However, the presence of neutral lipid nanospheres in the digestive food vacuole of *Plasmodium* as well as the association of NLBs with the digestive vacuole suggests that these neutral may have a role in hemozoin formation, a process that occurs within this organelle. In this study, experimental data supports the hypothesis that neutral lipid nanospheres within the digestive food vacuole together with lipid bodies associated with the digestive vacuole are not only the location of *in vivo* hemozoin formation, but are also essential for the survival of the parasite by functioning as a time and site specific mediator of heme detoxification. Previous studies of synthetic neutral lipid droplets formed through sonication reported successful mediation of β -hematin formation (94). Recently, interfacial studies revealed crystal formation at a biologically compatible rate ($t_{1/2} \approx 2$ min) (95, 96).

Characterization of Synthetic Neutral Lipid Bodies

SNLBs were formed by depositing an appropriate blend of neutral lipid onto an aqueous layer. Confocal imaging of samples extracted from just beneath the surface confirmed that this composition of lipids spontaneously organizes into an emulsion (Figure 11). Orthogonal projections of these lipid droplets demonstrate formation of spherical lipid droplets with continuous, not hollow interiors (Figure 11a), similar to our previously reported study using pure monoglyceride (97). Visually, the SNLBs exhibited a size distribution of a few hundred nanometers to few microns in diameter. In the current study, a neutral lipid blend in the ratio reported by Sullivan and coworkers to be present in the parasite (4MSG:2MPG:1DOG:1DLG:1DPG) (57) was observed to spontaneously assemble into an emulsion with the lipid dispersed in a form resembling lipid droplets. These SNLBs displayed physical properties (i.e. spherical droplets with diameters in the range of hundreds of nanometers to a few micrometers) similar to those of its *in vivo* counterparts (72, 73), rendering them useful for investigation of their role in hemozoin formation. The polarity of this lipid environment was found to lie between that of acetone and that of octanol as determined by the fluorescence emission peak maximum position of NR.

To determine the uniqueness of the SNLB (differed from those of its individual components), differential scanning calorimetry (DSC) was performed on the lipid blend and its individual components. Ideally, if the heterogeneous lipid composition of the lipid blend provides better packing of lipids molecules through new bond formations, a detectable change in heat flux would be necessary to break these new bonds. Measured phase transitional peaks of the five neutral lipid samples were consistent with those of published values (98). Lipids containing saturated hydrocarbon chains (MSG, MPG, DPG) have a higher melting point than lipids with

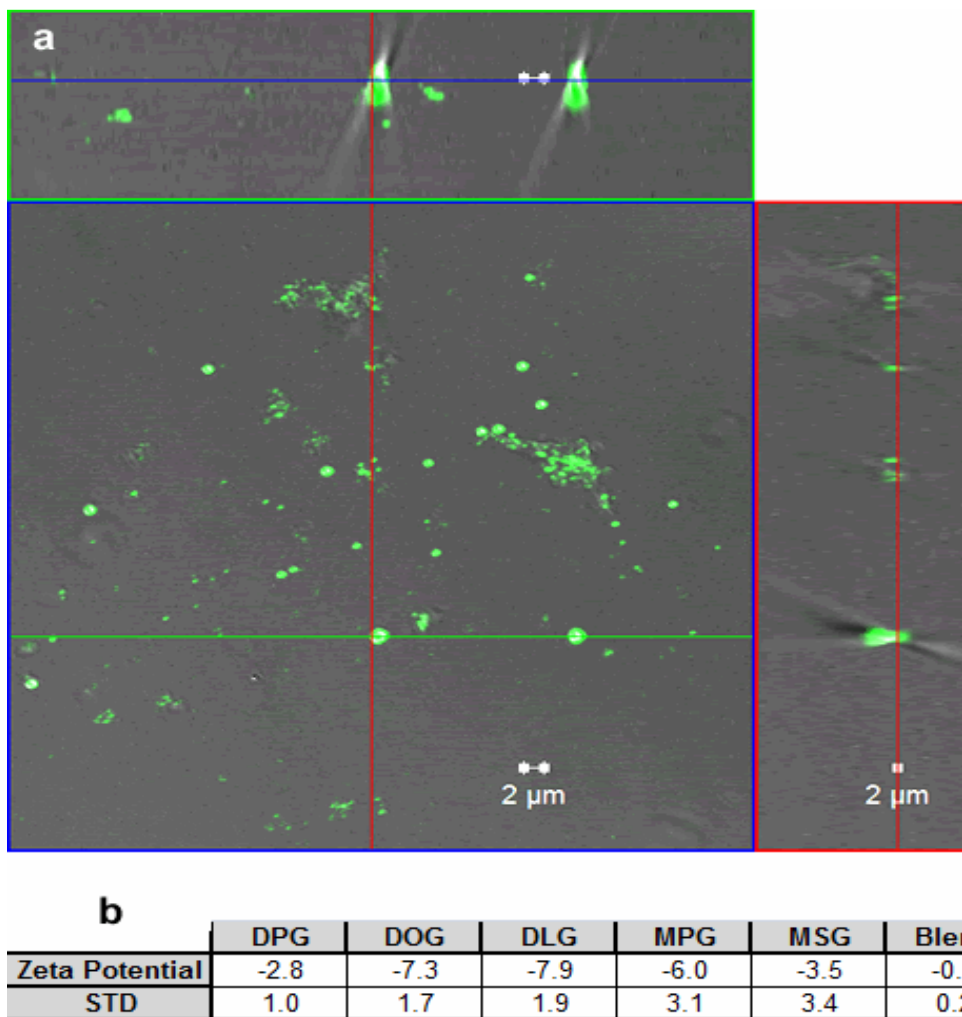


Figure 11. Confocal micrographs of SNLB and zeta potentials of SNLB and its components. (a) Confocal microscopy of NR labeled SNLB composed of the lipid blend 4:2:1:1:1 MSG/MPG/DOG/DLG/DPG demonstrates the presence of micron sized lipid droplets with continuous interiors. (b) Zeta potentials of the individual neutral lipids and SNLB are all close to zero as expected.

unsaturated chains (DLG and DOG). Upon heating of saturated lipids, MSG, MPG, and DPG, negative heat flow peaks were measured at 76, 74, and 74 °C, respectively (Figure 2a,b,c). These values matched those of published measurements (84) for corresponding melting temperatures. Cooling of the samples produced a positive heat flow at 69, 63 and 63 °C, corresponding to crystallization peaks of MSG, MPG, and DPG, respectively. In general, pure saturated asymmetric monoglycerides exist in three polymorphic forms, namely sub- α , α , and β (99). All polymorphs have a double chain length packing mode, characterized by a long spacing of about 50 Å for MSG. When monoglycerides, present in the α polymorph, are cooled 35-50 °C below the crystallization point of the α polymorph, they undergo a polymorphic transition to a reversible sub- α polymorph. Further cooling of MSG and MPG samples produced positive heat flow peaks at 40 and 36 °C. These peaks are interpreted as the transition point (α to sub- α form) for MSG and MPG and are consistent to transition temperatures published by Gunston and Padley (100).

Phase transition measurements for unsaturated diglycerides differed from those of saturated monoglycerides. Melting temperatures of 4.0 and 25 °C were measured for DLG and DOG, respectively (Figure 12d,e). Cooling of the samples produced positive heat flow peaks at -5 and 14 °C, respectively. DSC plot of individual components of the lipid blend were normalized to the biological ratio (20) and overlaid (Figure 12f). When compared to the overlaid plot (Figure 12g), DSC plot of the lipid blend exhibited new melting peaks that shifted to lower temperatures (5, 20, 63 °C). Instead of 4 crystallization peaks, the lipid blend contained two new peaks at 5 and 45 °C. In addition to DSC measurements, the zeta potentials of blend and its individual components were compared in order to explore the possibility that cations might accumulate around the head groups. However, true to its “neutral” lipid definition, no significant

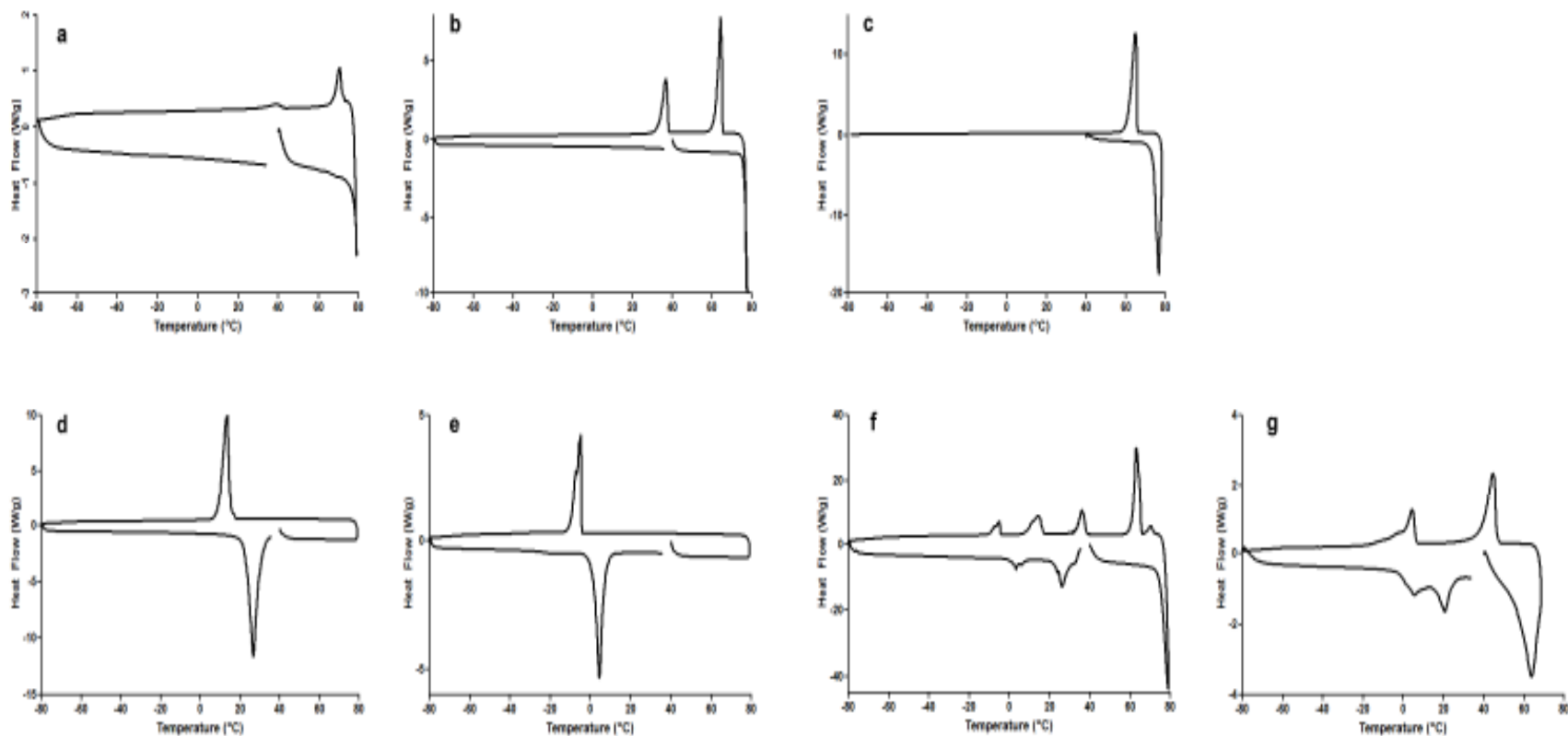


Figure 12. Differential scanning calorimetry of individual lipids and the lipid blend. The scans are for (a) MSG, (b) MPG, (c) DPG, (d) DOG, (e) DLG, (f) overlay of MSG/MPG/DOG/DLG/DPG normalized to the lipid blend ratio of 4:2:1:1:1, respectively, and (g) the lipid blend.

charge potential difference was observed for each individual component or the lipid blend composition (Figure 11b).

The SNLB provides a unique crystallization environment that differs from that of its individual components. The melting properties revealed by differential scanning calorimetry of the lipid blend are not merely an overlay of the phase transitions of each individual component. The interactions of the five neutral lipids produce two new crystallization and three new melting peaks, suggesting that the heterogeneous lipid population of the lipid blend facilitated a new molecular organization of lipids. A melting temperature shift to lower temperature suggests that less interaction is occurring between lipid molecules in the SNLB than in homogenous samples. This is evident in a comparison of melting temperatures between mono- and di-glyceride. In saturated MSG and MPG samples, measured melting temperature is higher than that of unsaturated DLG and DOG. This is likely a result of the presence of double bonds in the unsaturated lipids. These “kinks” will reduce the alignment of the hydrocarbon chains, producing a more fluid packing environment. Despite the lipid blend comprising of 2:1 monoglycerides to diglycerides, the presence of DOG and DLG reduced the primary melting peak. This lower melting point suggests that less stable or fewer interactions between lipid molecules are present in the SNLBs, which may result in a more fluid packing orientation.

The new organization of lipids in the SNLB is not entirely unexpected given the diversity in head group and in the saturation of hydro-carbon chain of the components of the lipid blend. It has previously been demonstrated that the temperatures at which lipids undergo phase transitions is dependent upon the head group, the hydrocarbon chain length, and the degree and type of unsaturation present (98). For example, the addition of double bonds, as in the case with DOG and DLG, reduces the hydrophobic interactions between lipid molecules thereby creating weaker

dispersion interactions. Berlin and Sainz's DSC examination of phase transitions and molecular orientation in the liquid state of sonicated dispersions of neutral lipids reported that the positioning of acyl moieties in glycerolipids reduces the fluidity of dispersed lipid micelles (84). The authors attributed this restriction in mobility to the interactions between adjacent acyl chains. By the same reasoning, lipid droplets composed of homogenous monoglycerides (MSG or MPG) are likely to exhibit more surface rigidity than lipid droplets composed of a heterogeneous composition, such as the lipid blend. The diversity in saturation of the components of the lipid blend will also contribute to the overall packing of the lipids in the lipid droplets, since unsaturated hydrocarbon chains do not pack as well as saturated chains. Together, DSC data demonstrates that the SNLBs are partly molten, a fact which may play a significant role in the biological function of the blend in hemozoin formation.

Kinetics of β -hematin formation.

Morphological, structural and spectroscopic analysis of the brown pigment formed by introducing soluble Fe(III)PPIX to the lipid blend emulsion unequivocally confirm the presence of β -hematin (Figure 13). SEM imaging of the product showed needle-like crystals resembling hemozoin in crystal habit (Figure 13c). TEM imaging of the largest face displayed electron dense crystals with a lattice spacing corresponding to the {100} face of hemozoin (Figure 13d). Infrared spectra exhibiting prominent peaks at 1662 cm^{-1} and 1210 cm^{-1} , corresponding to the presence of the C=O and C-O stretching vibrations of propionate linked hematin dimers, confirmed the formation of β -hematin (Figure 13b). These findings are further supported by pXRD exhibiting the three characteristic diffraction peaks of beta-hematin (Figure 13a).

Together, these results definitively confirm the ability of SNLBs to mediate β -hematin formation.

SNLBs successfully promoted β -hematin formation under physiologically relevant conditions (37 °C, pH 4.8) with a half life ($t_{1/2}$) 1.9 ± 0.01 min (Figure 14b). The activation energy of hemozoin formation mediated by SNLBs and each of the individual components were determined from Arrhenius plots. An examination of activation energy revealed that monoglycerides exhibited energy barriers higher than those of diglycerides. MSG and MPG have calculated values of 74.8 ± 5.3 kJ/mol and 60.4 ± 7.1 kJ/mol, respectively, while DLG, DPG and DOG showed lower values of 44.5 ± 15.4 kJ/mol, 35.2 ± 9.4 kJ/mol, and 37.7 ± 3.3 kJ/mol, respectively (Figure 14a). When the individual lipids are combined, the lipid blend revealed a much lower activation energy barrier of 27.8 ± 3.4 kJ/mol (Figure 14c). To evaluate the statistical significance of these relationships, t-test analyses were performed. Mean activation energies for the blend compared to those of MSG and MPG revealed 99.8% ($p = 0.002$) and 99.3% ($p = 0.007$) confidence levels, suggesting the observed relationships between the blend and monoglycerides are statistically significant. Similar observations were calculated for blend-DOG and blend-DPG with 98% ($p = 0.02$) and 93% ($p = 0.07$) confidence levels respectively. T-test evaluation for blend-DLG revealed an 86% confidence level ($p = 0.14$). The introduction of Fe(III)PPIX to the SNLB suspension successfully produced a brown pigment with a $t_{1/2}$ of 1.9 ± 0.01 min at 37 °C and pH 4.8, close to that reported for the malaria parasite DV(41, 42). This rate of heme conversion is well within the maximum half-life of 40 min previously estimated to be the maximum necessary to account for the observation that free heme in the parasite is limited to a maximum of 5% at 36 h in the lifecycle (95). Characterization using pXRD, FTIR, TEM and SEM clearly confirmed that the product was indeed β -hematin, demonstrating that SNLB-

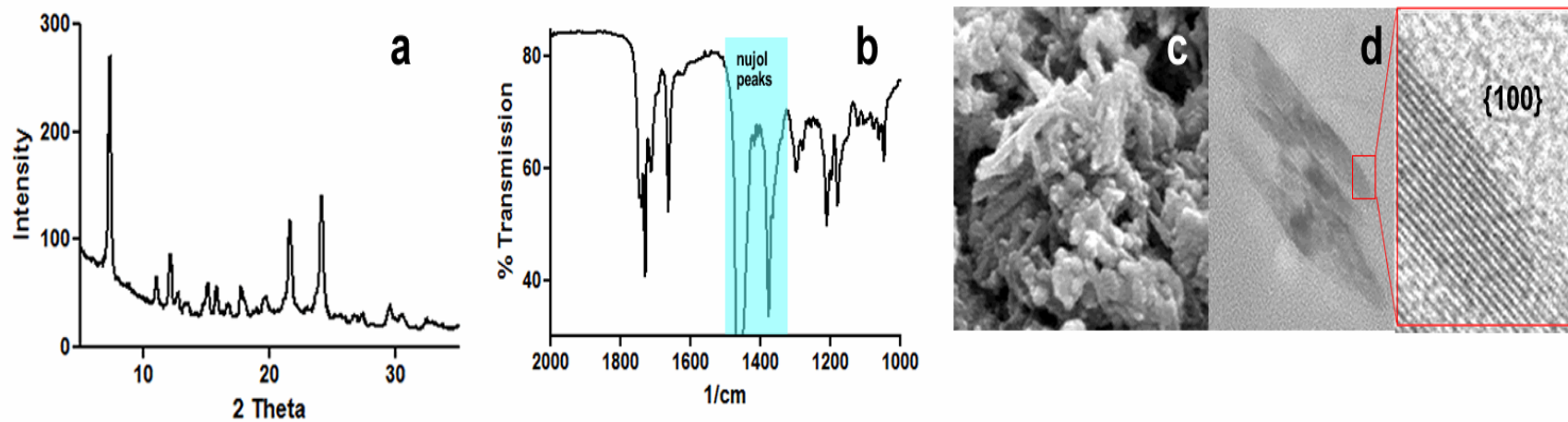


Figure 13. Characterization of beta-hematin produced using SNLB suspended in citric buffer, pH 4.8, 37 °C. (a) pXRD, (b) FTIR, (c) SEM and (d) TEM all show the characteristic features of beta-hematin. Fringes in the TEM in (d) exhibit the characteristic lattice spacing of the {100} face of beta-hematin.

mediated β -hematin formation is rapid and efficient under biologically realistic conditions. Such a rapid rate of heme conversion by the corresponding lipid blend in the parasite DV would therefore account for the fact that non-Hz Fe(III)PPIX is undetectable (i.e. makes up less than 5 % of total Fe) in the Mössbauer spectrum of late trophozoite stage parasites (101).

Kinetic studies revealed that the degree of saturation of the lipids influences the activation energy of β -hematin formation. SNLBs composed of just DPG, DOG, or DLG displayed lower activation energies than those of monoglycerides (MSG or MPG). The difference in molecular packing of the lipid molecules may be responsible for these measured differences. As explained above, DLG and DOG exhibit greater fluidity at the lipid body surface. This loosely packed surface may allow for faster organization of Fe(III)PPIX molecules, resulting in the measured lower activation energy. In the case of the lipid blend, the incorporation of a heterogeneous lipid population apparently alters the surface properties of the lipid body, with the differences in hydrocarbon chain length, degree of saturation and head group polarity all contributing to a more fluid and corrugated surface (84, 85) that is better able to template β -hematin formation. This surface may provide “pockets” for precursor heme dimers to intercalate in order to assemble, initiating hemozoin nucleation. Furthermore, the increase in packing fluidity may explain the complexity of the lipid blend associated with hemozoin in the parasite. If one type of lipid is sufficient to template hemozoin formation (58, 97), why does the parasite use a composition of five different lipid components? The answer is likely to be associated with the increase in surface energy associated with the template surface. This is evident in the observed lower activation energy. Further studies that include the examination of lipid packing are critical to further evaluate this hypothesis. Given that lipid peroxidation typically occurs at methylene groups adjacent to double bonds (102), making saturated lipids less

susceptible to oxidative damage than unsaturated lipids, the blend might also provide a means for the parasite to create an interface with hemozoin forming properties that resembles that of unsaturated lipids, while retaining a lipid mixture that is composed of almost 80% saturated lipids. In the strongly oxidative environment of the DV, this may reduce degradation of the lipid nanospheres and production of lipid peroxides.

Fe(III)PPIX Partitioning into Neutral Lipid Bodies

The fluorescence spectrum of NR is solvatochromic, with more hydrophobic solvents producing a shorter maximum intensity emission wavelength ($\lambda_{em(max)}$) than do more hydrophilic solvents (103). Examination of $\lambda_{em(max)}$ for a range of solvents exhibits a linear dependence of this parameter on the $E_T(30)$ of the solvent, a measure of microscopic hydrophobicity (Figure 15inset). The spectrum of NR in SNLBs (Figure 3) exhibits a $\lambda_{em(max)}$ of 617 nm, corresponding to an $E_T(30)$ of 45 ± 4 kcalmol⁻¹. This is slightly more polar than acetone (42.2 kcalmol⁻¹), but less polar than octanol (48.1 Kcal mol⁻¹) (104). It also definitively demonstrates that NR is incorporated into the SNLBs and does not reside in the aqueous solution, confirming the observations of the microscopy studies.

One leading hypothesis for hemozoin formation involves epitaxial nucleation at the lipid-water interface, extension of the crystal along the interface, and an interior movement of the hydrophobic crystal to the interior of the neutral lipid body (95, 96, 105). However, little is known about the partitioning of Fe(III)PPIX molecules into the lipid droplets. Using the unique selective neutral lipid staining property of NR, it has been possible to follow the partitioning of soluble Fe(III)PPIX into SNLBs (94, 103). Fluorescence calibration measurements reveal a linear relationship between the concentration of NR and measured fluorescence intensity (up to 1

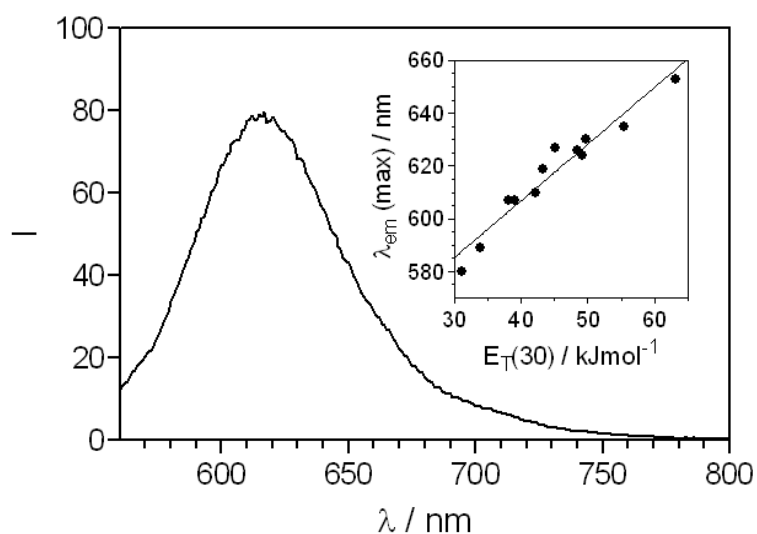


Figure 15. A typical fluorescence emission spectrum of NR in SNLBs dispersed in aqueous solution (pH 7.4, 25 °C, 0.02 M HEPES buffer). The excitation wavelength is 540 nm. The inset shows the correlation ($r^2 = 0.94$) between emission wavelength maximum of NR and the Dimroth-Reichardt hydrophobicity parameter $E_T(30)$ (104). The solvents are (from lowest to highest $E_T(30)$): dodecane, toluene, ethyl acetate, chloroform, acetone, dimethylformamide, dimethylsulfoxide, isopropanol, pentanol, butanol, methanol and water.

μM in a conventional cuvette and up to at least $12 \mu\text{M}$ when using a 96 well plate attachment) (Figure 16a). In all experiments presented here, the concentration of Nile Red used in experimental measurements was well within the linear fluorescence range. The introduction of soluble Fe(III)PPIX to an aqueous emulsion of the lipid blend containing NR resulted in concentration dependent quenching of fluorescence. This quenching was found to conform to the Stern-Volmer relationship up to at least $60 \mu\text{M}$ Fe(III)PPIX, indicating that the decrease in fluorescence intensity is a result of dynamic (collisional) rather than static quenching (Figure 16b inset). The latter would be expected to give rise to an upward deviation from linearity (106). The slope of the Stern-Volmer plot, K_{SV} , is dependent on pH of the aqueous medium (Figure 16c). Since K_{SV} is the product of the fluorescence lifetime of the fluorophore (τ_0) and the bimolecular quenching constant (k_q), it is not expected to change as a function of pH, because the interior of the NR labeled SNLB is not likely to be altered by the pH of the aqueous medium. The most likely explanation for the increase in K_{SV} with decreasing pH is therefore that the local concentration of Fe(III)PPIX in the SNLB particle increases with decreasing pH owing to increased partitioning of the partly protonated neutral form of Fe(III)PPIX into the hydrophobic lipid. Indeed, the data can be fitted to a protonation model with a single pK_a of 4.62 ± 0.09 , with a K_{SV} of $0.021 \pm 0.003 \mu\text{M}^{-1}$ in the deprotonated form and $0.124 \pm 0.007 \mu\text{M}^{-1}$ in the protonated form. Assuming that this difference arises solely as a result of increased Fe(III)PPIX concentration in the SNLB particle in the case of the protonated form, this indicates a 6 ± 1 fold accumulation of the protonated relative to the uprotonated form of Fe(III)PPIX in SNLB. Unfortunately, the absolute $\log D_{\text{lipid}}$ cannot be evaluated from these data. However, measurement of octanol-water partitioning of Fe(III)PPIX at pH 7.51 where it is soluble in both

media indicate a $\log D_{OW}$ of about 1.8. This suggests an approximate $\log P$ for Fe(III)PPIX in its neutral form of about 2.6.

This quenching of NR was visually corroborated using confocal microscopy. Immediately following the addition of Fe(III)PPIX to NR labeled SNLBs under physiological conditions, fluorescent quenching was observed (Figure 17a). In fact, the rate of Fe(III)PPIX partitioning into the SNLBs was found to be pH dependent. Under pH conditions (2.3, 4.8 and 5.5) that include the expected range for the parasite DV (107-109), NR quenching observed at 50 s after the first addition of 500 μ M Fe(III)PPIX was 74%, 78%, and 76%, respectively (Figure 17b). Interestingly, at pH 1.3, slightly less quenching was observed (26%), possibly because Fe(III)PPIX is entirely in its doubly protonated cationic form at this pH value. Likewise, significantly less quenching was observed (at 50 s) for pH 6.7, 7.3, and 8.1, respectively where the NR quenching was only 23%, 20% and 28%. At 150 s, the percent of total quenching for samples incubated in pH 2.3, 4.8, and 5.5 approaches their maximum value (90%, 92%, and 94%, respectively). These values do not increase significantly at 200 s. For quenching at pH 4.8, a final heme concentration of 0.22 mM was required to quench the interior of the SNLB-NR. Note that this value reflects the overall amount of Fe(III)PPIX introduced to the SNLB solution and not the amount of Fe(III)PPIX localized within the SNLB.

At 200 s, maximum quenching was observed for samples incubated at pH 1.3, 6.7, 7.3, and 8.1 of 80%, 89%, 87% and 57%, respectively. Location specific monitoring of fluorescence intensity during quenching experiments displayed selective localization of Fe(III)PPIX. Regions with no lipid present measured no significant changes in fluorescence. To ensure that the quenching effect was not due to photobleaching, the fluorescence intensity of labeled SNLBs was monitored. Mild quenching, specifically, a reduction of 2.0% in fluorescence intensity unit

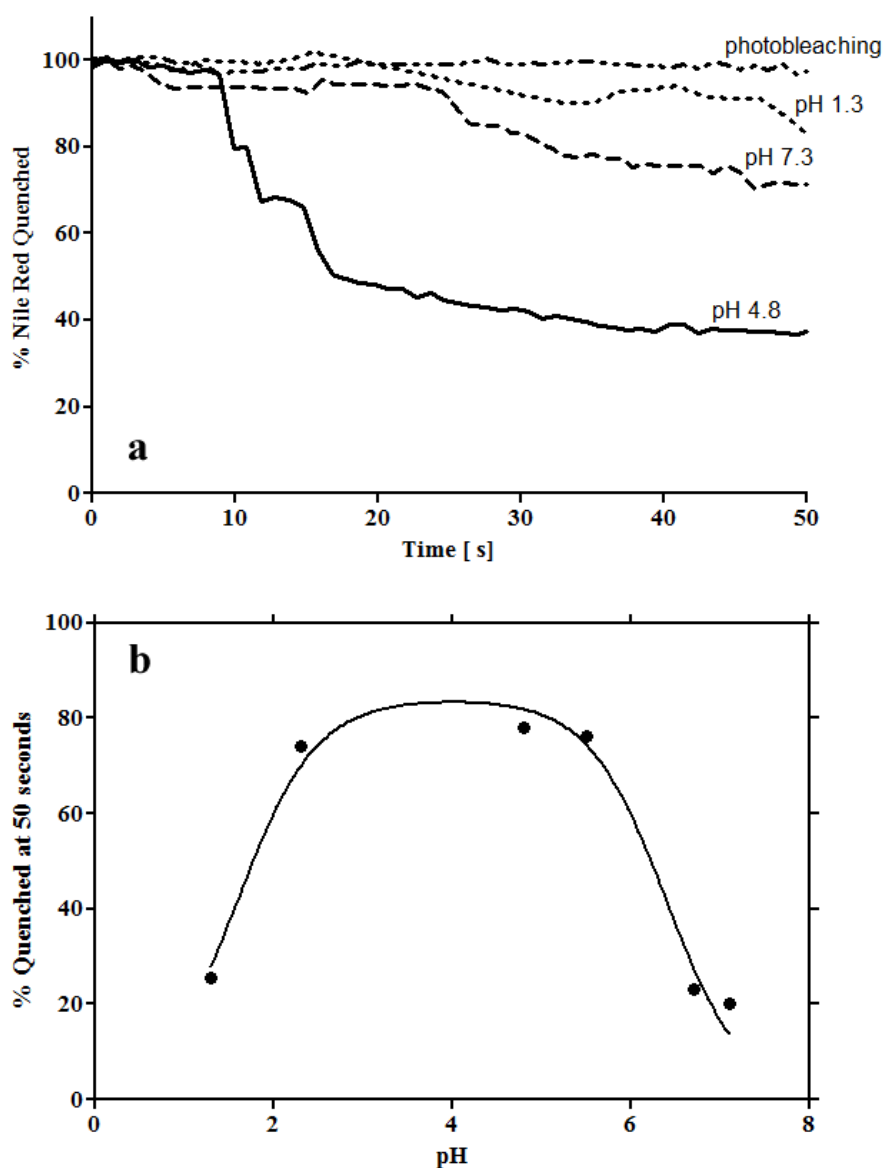


Figure 17. Rate of Fe(III)PPIX quenching of Nile Red(NR) labeled synthetic neutral lipid droplet (SNLB). At pH similar to that of the digestive food vacuole of *Plasmodium* (pH 4.8), Fe(III)PPIX rapidly partitions into SNLB, indicated by quenching of NR (a). At pH where the two propionate side group of Fe(III)PPIX is predominately unionized or ionized, the rate of NR quenching is slower (b).

was measured at after 50 s (Figure 17a) and 23 % at 200 s, suggesting that drastically decreased fluorescence intensities of SNLBs were indeed a consequence of the addition of Fe(III)PPIX and not photobleaching (Figure 17a). To confirm that the continual introduction of Fe(III)PPIX did not disrupt quenching measurements, Fe(III)PPIX was also added once to the SNLB-NR solution to produce a final Fe(III)PPIX concentration of 0.20 mM. Maximum quenching of this sample was still observed at the 200 s; however, a slower rate of partitioning was observed. At the 50 s time point, only 40% quenching was observed.

To explore the partition of Fe(III)PPIX into SNLBs, the hydrophobic dye, Nile Red, was employed. Conveniently, soluble Fe(III)PPIX was observed to be capable of quenching NR fluorescence. Linear Stern-Volmer plots indicate that this is a result of collisional quenching (106). These observations suggest about a 400-fold partitioning of the neutral form of Fe(III)PPIX into SNLBs relative to the aqueous medium. This phenomenon was visualized by confocal microscopy as a diminishing of fluorescence upon the addition of Fe(III)PPIX. In previous studies, TEM images of soluble Fe(III)PPIX introduced to SNLBs composed of MPG showed the localization of electron dense matter surrounding the lipid droplets (96). However, in the absence of elemental imaging, it could not be confirmed that this electron dense material was indeed heme. In this study, confocal microscopic studies confirmed that Fe(III)PPIX spontaneously localizes to SNLBs under physiologically relevant conditions. Visually, a dramatic reduction in fluorescence intensity of NR labeled-lipid blend was observed upon introduction of Fe(III)PPIX (please refer to supplemental section for video imaging of the described event). Further addition of Fe(III)PPIX resulted in almost complete quenching of the droplet fluorescence. This may be the first visual, real-time, evidence of heme partitioning into the neutral lipid droplets. Within the malaria parasite, heme is released as a consequence of

hemoglobin degradation in a continuous manner. The immediate localization of these heme molecules in the DV lipid nanospheres would be expected to encourage rapid crystallization of hemozoin. However, *in vivo* transport mechanisms remain unclear. No additional mediator was introduced to facilitate the trafficking of Fe(III)PPIX in the current study. However, the same spontaneous localization may not exist within the complex environment of the DV.

The rate of Fe(III)PPIX partitioning into the SNLBs observed using confocal microscopy appears to be pH dependent and seemingly parallels conditions required for β -hematin formation (96, 110, 111). In the pH range that encompasses that which promotes β -hematin formation *in vivo* (pH ~2.3 to 6.5), Fe(III)PPIX molecules partition rapidly into the SNLBs. Outside this range (pH 1.3, 6.7, 7.3, 8.1), the initial (50 second) quenching was dramatically lower. These observations can be attributed to the protonation state of Fe(III)PPIX (Appendix A). At low pH (<2.0), both propionates of Fe(III)PPIX are protonated and a water molecule is present as the axial ligand. In this environment, an overall charge of +1 substantially decreases the partitioning of Fe(III)PPIX into the SNLBs. Between pH 2.3 and 5.5, one propionate is presumably deprotonated, producing an overall neutral state which allows Fe(III)PPIX to enter the SNLBs to a greater extent. From pH 5.5 to 7.5, both propionates are likely ionized, with the water axial ligand remaining protonated and resulting in an overall charge of -1. Fe(III)PPIX again cannot easily partition strongly into the lipid. Above pH 7.5, the axial ligand is OH⁻ and the overall charge is -2 further inhibiting Fe(III)PPIX from entering the lipid. Interestingly, over a longer time period, there is a further increase in Fe(III)PPIX uptake under these conditions, indicating that the rate of Fe(III)PPIX partitioning is decreased. Only in the pH range of the digestive vacuole will released heme be able to rapidly enter the lipid droplets to a strong extent and convert to hemozoin, avoiding toxicity. This observed pattern of heme partitioning into the

SNLBs illustrates the ability of lipid droplets to control the site of hemozoin formation during heme detoxification. Similar pH trends of heme partitioning were observed for maximum quenching. Specifically, peripheral quenching, indicating that Fe(III)PPIX did not enter the interior of the SNLBs, was observed at pH 1.3 and pH 6.7 and higher.

Conclusions

In this study, confocal microscopic studies confirmed that Fe(III)PPIX spontaneously localizes to SNLBs under physiologically equivalent conditions. Visually, a dramatic reduction in fluorescence intensity of NR labeled-lipid blend was observed upon introduction of Fe(III)PPIX. Further addition of Fe(III)PPIX resulted in almost complete quenching of the droplet fluorescence. This may be the first visual, real-time, evidence of Fe(III)PPIX partitioning into the neutral lipid bodies. Within the malaria parasite, Fe(III)PPIX is released as a consequence of hemoglobin degradation in a continuous manner. The immediate localization of these Fe(III)PPIX molecules in the DV lipid bodies would be expected to encourage rapid crystallization of hemozoin. However, *in vivo* transport mechanisms remain unclear. No additional mediator was introduced to facilitate the trafficking of Fe(III)PPIX to the current study. However, the same spontaneous localization may not exist within the complex environment of the digestive vacuole.

The precise mechanism of formation of hemozoin remains an unanswered question. Paradigms from the field of biomineralization suggest that the process involves the supramolecular preorganization of an organic matrix (e.g. lipids or proteins) that provides a foundation for the second order assembly for inorganic species (*I*). In malaria, a growing body of evidence suggests that a lipid rich environment is essential for the formation of hemozoin (*57*,

73, 88). However, previous experimental data for beta-hematin formation under physiological conditions could not account for the speed of hemozoin formation *in vivo* or provide details of the nucleation and crystal extension process. In part I, lipid bodies were synthetically produced to serve as a model for the neutral lipid bodies that exist within the digestive food vacuole of *P. falciparum* and to shed light on their possible roles during hemozoin formation in nature. Experimental evidence provided here supports the hypothesis that the nucleation and extension of beta-hematin is localized at the interface of neutral lipid bodies and water and that these bodies are responsible for the reproducibility of the structural morphology and size of hemozoin crystals observed in nature. Based on these observations, beta-hematin formation schematically represented in Scheme 3 is proposed. This model accounts for the orientation and formation of beta-hematin crystals with respect to these bodies. In particular, the model stems from the observation made during these experiments, which revealed the presence of (i) heme localization and nucleation at the lipid-water interface, (ii) crystal extension along the interface, (iii) orientation of mature crystals and (iv), crystal sizes that appear to be limited by the size of the lipid bodies. Finally, it should be noted that it is likely that the transport and delivery of heme to the lipid droplets *in vivo* will differ in several respects. The extent of heme accumulation may be much lower, since in the current experimental setup the entire quantity of heme was introduced to the lipid system at once, whereas *in vivo* hemoglobin degradation results in the continuous release of heme. In addition, it is possible that proteins may play a role in the delivery of heme to the lipid droplets.

In part II, the partitioning of Fe(III)PPIX to the synthetic neutral lipid droplets at pH values close to those of the DV of *P. falciparum* was demonstrated. The neutral lipid blend reported to be present in the DV has unique properties which seem to strongly promote β -

hematin formation by drastically lowering the activation energy of the process relative to lipid emulsions containing monoglycerides. In particular, despite being composed largely of saturated mono- and diglycerides, it lowers the activation energy to a level similar to, but even lower than the unsaturated diglyceride DOG. This suggests that the particular composition of the blend plays a critical role in its biological function. Collectively, these findings strongly support the hypothesis that hemozoin formation is brought about by lipid droplets (lipid nanospheres) in the DV. It is noteworthy that the time period reported for NLB production *in vivo* coincides with that of the blood feeding stage of the *P. falciparum* life cycle. The relative abundance and localization of lipid bodies are stage dependent (112, 113) with a large numbers of lipid bodies found in the late trophozoite and early schizont stages of the intraerythrocytic cycle (113, 114). In addition, microscopic observations of lipid bodies during the course of intraerythrocytic development have been reported to reveal tiny Nile Red fluorescent dots ($<1\mu\text{m}$) in the early ring stage. These dots increase in size ($\sim 2\mu\text{m}$) as development proceeds to later stages (113). The overlapping of neutral lipid body production and hemoglobin degradation are unlikely to be coincidental and may indicate that neutral lipid droplets are important in sustaining parasite viability via heme detoxification through mediation of hemozoin formation.

Sectional Acknowledgements

Special thanks to the following collaborator: Dr. Timothy Egan (University of Cape Town(UCT), South Africa), Dr. Katherine De Villiers (University of Stellenbosch, South Africa), and Dr. Kanyile Ncokazi (UCT) for generously hosting me for four-five months in Cape Town and convincing me that great scientific research can be achieved with a uv-vis spectroscopy and a water bath. Special thanks to Rebecca Sandlin (Vanderbilt University) who have spent endless days performing kinetic experiments with me. Finally, thank you Aneesa

Omar (UCT), who I have met only through emails/chats, for her contribution during Stern-Volmer quenching experiments.

Chapter III

INTERACTIONS OF NEUTRAL LIPIDS AND FERRIPROTOPORPHYRIN IX DURING HEMOZOIN FORMATION IN LANGMUIR-BLODGETT FILMS

Fe(III)PPIX's potential role in a number of pathogenic conditions has produced an increased interest in its behavior in physiological conditions (i.e aqueous solutions) (115). Abnormal release of Fe(III)PPIX from protein degradation has been implicated in atherogenesis, cancer, hemolysis, and inflammation (116-119). Within the human host, blood feeding parasites, such as the pathogenic helminth *Schistosoma* and the protozoan malaria *Plasmodium*, degrade large quantities of host hemoglobin in order to utilize the protein's amino acids for maturation. As a consequence of this proteolysis, heme is released. In the "free" state, heme induces oxygen dependent free radical formation,(120, 121) lipid peroxidation(122, 123) and protein(124) and DNA(125) oxidation, all of which are deleterious to the parasite. Several blood-feeding organisms, namely, the malaria parasite *Plasmodium falciparum*, the worm *Schistosoma mansoni*, and the kissing bug *Rhodnius Prolixus*, have evolved efficient adaptations to circumvent the toxic effects of "free" heme (11). In these organisms, this process involves the crystallization of heme into hemozoin (126). Despite hemozoin's established role in the heme detoxification pathway, the precise molecular mechanism necessary for hemozoin formation remains unclear.

Recent investigations implicate neutral lipids as the *in vivo* mediator of hemozoin formation (57, 58, 97). Specifically, electron microscopy imaging of *P. falciparum*, *S. mansoni*, and *R. Prolixus* provide irrefutable evidence that hemozoin formation occurs in close association

with lipid bodies. (57, 77) Using the hydrophobic probe, Nile Red, Tilley and colleagues showed that these lipid bodies are closely associated with the digestive food vacuole of *P. falciparum* and that this lipid population measured about a few hundred nanometers in size (73) Sullivan and colleague later identified the composition of these lipid bodies as a specific lipid mixture: monoglycerols monostearoylglycerol (MSG) and monopalmitoylglycerol (MPG) and the diglycerols dilinoleoylglycerol (DLG), dioleoylglycerol (DOG) and DPG (dipalmitoylglycerol) in a 4:2:1:1:1 ratio, respectively (herein referred to as the lipid blend) (57). In addition, *in vitro* studies showed that beta-hematin is produced at the lipid-water interface at a rate sufficient to avoid heme toxicity (58, 97). Although neutral lipids involvement in hemozoin formation has been demonstrated, the exact molecular mechanisms involved are not well understood.

Works presented in previous chapters have demonstrated the biology realistic process of beta-hematin formation at the neutral lipid-water interface (58, 97). To better understand the molecular interactions of neutral lipids and heme, it is important to examine the lipid packing at the lipid-water interfaces. Traditional methods used to evaluate interface packing rely on concepts established in the early 1900's by Irving Langmuir which remain popular today. The surface pressure-area isotherm (π -A) of a floating LB monolayer allows for the systematic examination of the 2D interactions of the lipid-Fe(III)PPIX that would otherwise be much difficult to do in the hydrated bulk environment. LB techniques have been successfully applied to the study of human diseases. For example, Leblanc and colleagues investigated the origin of Alzheimer's Disease by examining packing properties of amyloids (127-129). Regen *et al.* (130) further examined oxysterol induced rearrangement of the liquid-order phase and its link to Alzheimer's Disease. In addition, Chimote and Banerjee investigated mycobacterial cell wall lipids notable in tuberculosis (131). In this study, the hypothesis that nucleation of hemozoin

occurs via the interaction of Fe(III)PPIX and neutral lipid. The molecular interactions of neutral lipids and Fe(III)PPIX molecules are examined to better understand the *in vivo* mechanism of hemozoin formation in malaria. π -A isotherms of the lipid blend and of each of its individual components were measured to determine the packing stabilities at the lipid-water interface. The Fe(III)PPIX-lipid blend interactions were investigated by compressing lipid blend with various substituted protoporphyrin. The molecular corporation of antimalarial drug with the Fe(III)PPIX-lipid interactions was examined using chloroquine. This study provides further insight into molecular arrangement on the behavior of Fe(III)PPIX and neutral lipid at the interface. Details of Fe(III)PPIX and lipid interactions is a prerequisite to elucidation of hemozoin formation in nature and provides guidance for new anti-malarial drug design.

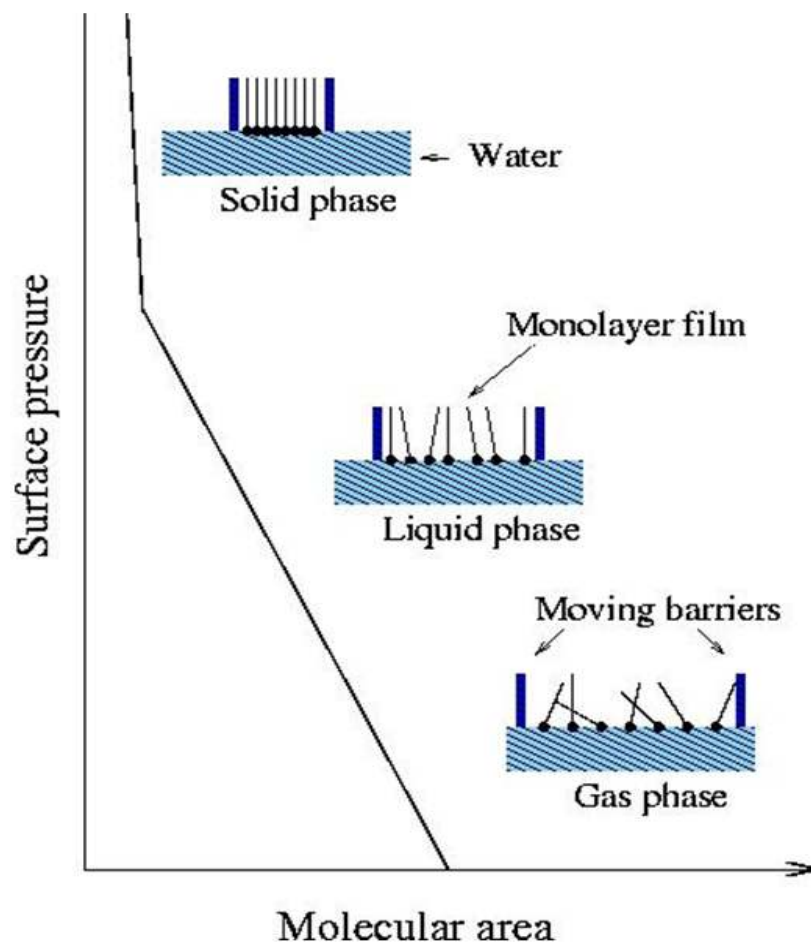
Experimental Methods

Langmuir Blodgett Theory

A molecular film at the air-water interface is called a Langmuir-Blodgett monolayer. This type of monolayer provides a unique approach to determine the chemical and physical behavior of monolayer of amphiphilic molecules at the phase boundary. An important advantage of investigating Fe(III)PPIX-lipid interactions using the Langmuir- Blodgett monolayer approach is that the range of molecular areas known to occur in natural neutral lipid bodies can be investigated systematically while avoiding the complication associated with the bulk hydrated dispersions *in vivo*. An amphiphilic compound of interest is dissolved in a volatile inert solvent. The solution is then spread uniformly at the air-water interface between two movable barriers. After the volatile solvent evaporated, a single monolayer film of the compound is formed at the

surface. The hydrophobic interactions between hydrocarbon tails and intermolecular interactions between the polar head group and the water subphase facilitate the stability of the monolayer. The monolayer is treated as a 2D solution and the molecular interactions of the deposited molecules are based on additivity relations of the components mean molecular area at various surface pressures (π) at constant area as a function of their composition. When the molecules are compressed, the molecules experience an increase of interactions with their neighbors. Conventionally, an air-water interface measures a force energy per unit area of 72 mN/m at 20°C. The deposit of an amphiphilic molecule to the interface will lower the surface tension. This measured surface pressure is the force per unit length with which the monolayer expand relative to clean surface (129). These interactions are represented in a π -A isotherm, a plot of the change in surface pressure (π) with relative to area (A) available to each molecule at the air-water interface (129). π -A isotherms are commonly recorded by measuring the surface tension γ directly (Wilhelmy plate method) or by measuring the difference $\pi = \gamma_0 - \gamma$ between the surface tension of the subphase and the surface tension of the subphase in the presence of a monolayer. π is then referred to as the film pressure or surface pressure.

The regions of a conventional isotherm include the gas (G), liquid (L), and solid (S) phases and have been reviewed in detail (Scheme 4) (132, 133) Briefly, when the molecules are positioned far apart, the film is said to be in the gaseous phase. In this state, no interactions occur between adjacent molecules. As the monolayer is compressed, the surface pressure rises and the area per unit molecule decrease, indicating the beginning of the liquid-expanded (LE) phase. During this phase, the hydrophobic tails begin to lift away from the subphase and weakly interact with adjacent tails. Under continued compression, the monolayer proceeds towards the liquid-condensed (LC) phase which is associated with short-range molecular interactions between

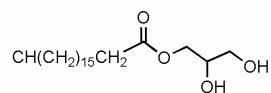


Scheme 4. Langmuir monolayer compression surface pressure-area (π -A) isotherm. When an amphiphilic lipid is deposited onto an aqueous surface, it is organized so that its polar head interacts with the water subphase and its hydrophobic tail oriented away from this subphase. As the barriers force the lipids together, a monolayer is formed. The lipid molecules go through a gas phase (G) in which minimal interactions occurs between neighboring molecules. Interaction between neighboring molecules occurs at the liquid phase. Maximum hydrophobic interactions occur when the hydrophobic tails are perpendicular to the subphase and lipid molecules are packed tightly together in the solid phase.

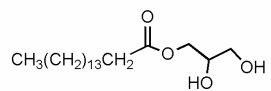
molecules. In this state, the molecules are ordered with the hydrophobic tails oriented to optimize interactions with neighbors. Further compression results in the solid phase when the hydrocarbon tails are perpendicular to the aqueous surface and maximum molecule-molecule interactions occur. Molecules in this phase have limited molecular motion and are packed into a rigid monolayer.

Reagents

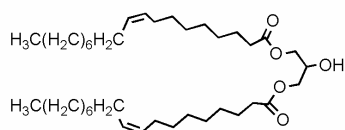
All lipids were obtained through Nu-Check Prep Inc. (Elysian, MN). The following neutral lipids were used: MSG – 1-monostearoylglycerol, MPG- 1-monopalmitoylglycerol, DOG – 1,3-dioleoylglycerol, DLG – 1,3-dilinoleoylglycerol, DPG – 1,3-dipalmitoylglycerol, and TPG- tripalmitoylglycerol. The lipid blend refers to the established biological ratio (by vol.) of 4:2:1:1:1 MSG:MPG:DOG:DLG:DPG, respectively.⁽⁵⁷⁾ A lipid blend stock solution of 3 mM in chloroform was prepared. A 3 mM stock solution of heme was also produced by dissolving appropriate hematin procine (Sigma-Aldrich) in DMSO. The heme solution was sonicated to ensure that all products went into solution. For compression experiments, the stock solutions were used to prepare samples of 100 μ M lipid blend and 100 μ M heme to make a final 100 μ L volume in chloroform. 50 mM citric buffer was used as the subphase at varying pH of 1.5, 3.0, 4.0, 5.0, and 7.0. The buffers were filtered three times using 0.2 μ m filter paper to remove impurities. This buffer does not promote beta-hematin formation and thus, is unlikely to disturb lipid and Fe(III)PPIX interaction¹⁸.



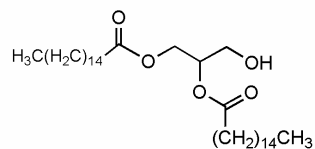
1-stearoyl-glycerol (MSG)



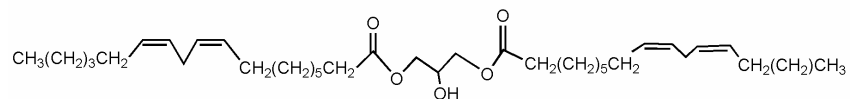
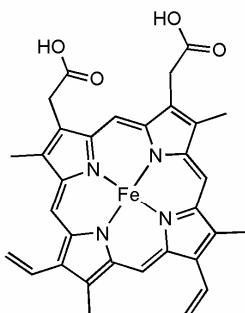
1-palmitoyl-glycerol (MPG)



1,2 dioleoyl-glycerol (DOG)



1,2-Dopalmitoyl-glycerol (DPG)



Scheme 5. The chemical formulas of the investigated compounds

Instrumental design

π -A isotherms were determined with a LB Teflon trough (Nima Model 612D) with a maximum area of 600 cm² and two mechanically coupled barriers. The surface pressure was measured by the Wilhemly plate method, using a filter paper of 1 cm width and Nima software. Prior to the measurements, the paper was rinsed and pre-wetted with the citric buffer (50 mM) subphase solution. Before each measurement, the subphase cleanness was checked for possible adsorbed impurities by measuring the surface pressure in the entire area interval. This pressure remained lower than 0.3 mN/m. All deposition was done using a 100 μ L microsyringe (Hamilton). Each compression was performed in triplicates to ensure reproducibility.

Langmuir-Blodgett π -A Isotherm

For neutral lipid compression studies, a 10 μ L solution of 100 μ M MPG, DPG, TPG, or lipid blend (4MSG:2MPG:1DOG:1DLG:1DPG) was deposited onto the citric buffer subphase. In this study, all measurements of π -A were collected under barrier compression speed of 20 cm²/min. To evaluate the interaction of the lipid blend-Fe(III)PPIX, a premixed solution containing 100 μ M of Fe(III)PPIX and lipid blend was made in chloroform. Ample time was allowed for the spreading solvent, CCl₃H, to evaporate before compression. To evaluate the effects of pH on the packing of lipid blend-Fe(III)PPIX, additional compressions were performed by spreading premixed solution onto citric buffer subphase at varying pH (1.5, 3.0, 4.0, 5.0, and 7.0). DMSO was employed to facilitate heme solubility. To investigate the molecular interaction of heme and lipid, compressions of the lipid blend and substituted protoporphyrin were performed. A solution of 10 μ L of 100 μ M lipid blend and Fe(III)PPIX was deposited onto clean citric buffer subphase. 15 minutes was allotted for the spreading solvent to evaporate

before compressing. This experiment was repeated with the substitution of protoporphyrin IX (PPIX), and ferriprotoporphyrin IX dimethyl ester for Fe(III)PPIX(Frontier Scientific). To ensure that DMSO did not contribute to the packing of Fe(III)PPIX-lipid, a control study was performed by premixing 3.3% DMSO in chloroform. 10 μ L of this solution was deposited onto clean citric buffer subphase and compressed. Less than 0.1 mN/m increase in surface pressure was observed, suggesting that minimal addition of DMSO did not disturb packing properties of molecules under investigation.

Antimalarial interactions

To examine the effects antimalarial drugs have on the lipid blend-Fe(III)PPIX packing, premixed solutions of 1:1:1 ratio of lipid blend:Fe(III)PPIX: chloroquine, all at 100 μ M, were compressed. Isotherms of lipid blend: anti-malarial were measured. Confocal analysis was employed to provide further insight into CQ mechanism of action at the lipid-water interface. Specifically, the hydrophilic dye Nile Red (NR)(73, 78) was used to determine the localization of CQ relative to the lipid surface. Synthetic neutral lipid bodies (SNLB) composed of the lipid blend was prepared by dissolving the proper ratio of lipid in a solution of 1:9 acetone to methanol (58, 97). 200 μ L of this solution was deposited onto the surface of 5mL citric buffer (50mM, pH 4.8) within a 15mL BD Falcon conical tube. The lipids are incubated at 37°C for approximately five minutes to allow for the spontaneous formation of SNLB. A 1 mM stock solution of Nile Red (MP Biomedicals) was prepared in acetone and used immediately. A proper volume of NR was then added to the SNLB solution to produce a 10:1 ratio of lipid to Nile Red. 180 μ L of the SNLB was transferred to a glass bottom microwell dish (35mm Petri dish and 14 mm microwell dish, MatTek Corporation). A 1 mM CQ solution was prepared in water. 20 μ L of

CQ solution was introduced to the SNLB-NR solution and imaged using a Zeiss LSM 510META upright confocal microscope (VUMC Cell Imaging Shared Resource) using the time series application with 63× oil(1.4) immersion objectives. Z-stacking was performed before and after quenching to ensure lipid bodies were not displaced during the experiment. Approximately 20 seconds after the first CQ addition, another 20 μL of chloroquine stock solution was added. This was repeated every 20 seconds for a total of 300 seconds and 625 μM . Images were prepared for publication using the LSM510 software. To confirm confocal data, fluorescence spectra were confirmed on the SNLB system. 20 μL of a 1mM lipid blend in 1:9 acetone to methanol solution was added to water. 2 μL of a 1 mM NR in acetone was added to the SNLB system. 5, 10, 50, or 100 μM of CQ was then added. The fluorescence spectrum was measured on a Varian Cary Eclipse fluorescence spectrophotometer. Both excitation and emission slit widths were set to 5 nm with a medium scan control and medium PMT detector voltage. The sample was excited at 590 nm and the emission spectrum was recorded from 650 nm. These fluorescence parameters for NR were previously reported by Greenspan (78).

Results and Discussion

Neutral lipid isotherm

A schematic representation of the lipid components is shown in Scheme 5. π -A isotherms, expressed by area (\AA^2) per lipid molecule, of mono-,di-,tri- palmitoyl glycerol and the lipid blend at physiological temperature (37°C) revealed that the lipid blend packs more similarly to mono-glycerol than di-glycerol (Figure 18b). MPG forms a typical liquid-condensed (LC) monolayer with a relatively steep rising π -A isotherm curve. This isotherm curve is shifted to higher molecular area by about 473 \AA^2 /molecule for DPG and about 735 \AA^2 /molecule for TPG.

More saturated molecules exhibited higher surface pressure maximums and a slightly steeper π -A curve. Given that the hydrocarbon tail length is constant in all three samples, the packing differences observed are attributed to the degree of hydrocarbon tail saturation. Increased saturation leads to better packing efficiency as a result of increased non-covalent interactions between the hydrophobic tails. Under compression, these more saturated molecules come into contact with neighboring molecules, maximizing their interactions. These interactions are represented by a steeper isotherm curve at higher molecular area for DPG and TPG (Figure 18a). The lipid blend π -A isotherm exhibited an expanded LE phase with a maximum pressure of 32 mN/m with a limiting area of 987 $\text{\AA}^2/\text{molecule}$, suggesting a disordered state with weak interactions between lipid molecules. Here, packing studies reveal that the lipid blend differs from its individual components. Differential scanning calorimetry (DSC) measurements of the lipid blend and its individual components may further corroborate the proposal that the lipid blend provides a unique hemozoin crystallization environment. By convention, the limiting area (A_{lim}) values correspond to the extrapolation of the lowest compressibility region or best packed phase of the isotherm to zero surface pressure. In the case of neutral lipid compression, these values represent the area corresponding to the transition from LE to LC phase. A linear trend was observed between glycerol saturation and corresponding A_{lim} values; more saturated glycerol experienced a phase transition (LE-LC) at higher area/molecule than the less saturated sample. A_{lim} values of 840, 1313, and 1575 $\text{\AA}^2/\text{molecule}$ were plotted against its corresponding lipid degree of saturation, MPG (1), DPG (2), TPG (3), respectively (Figure 18b). A linear relationship was observed for A_{lim} and degree of saturation ($y = 367x + 507$, $r^2 = 0.97$). The isotherm of the lipid blend displayed a A_{lim} value of 987 $\text{\AA}^2/\text{molecule}$. When this value was

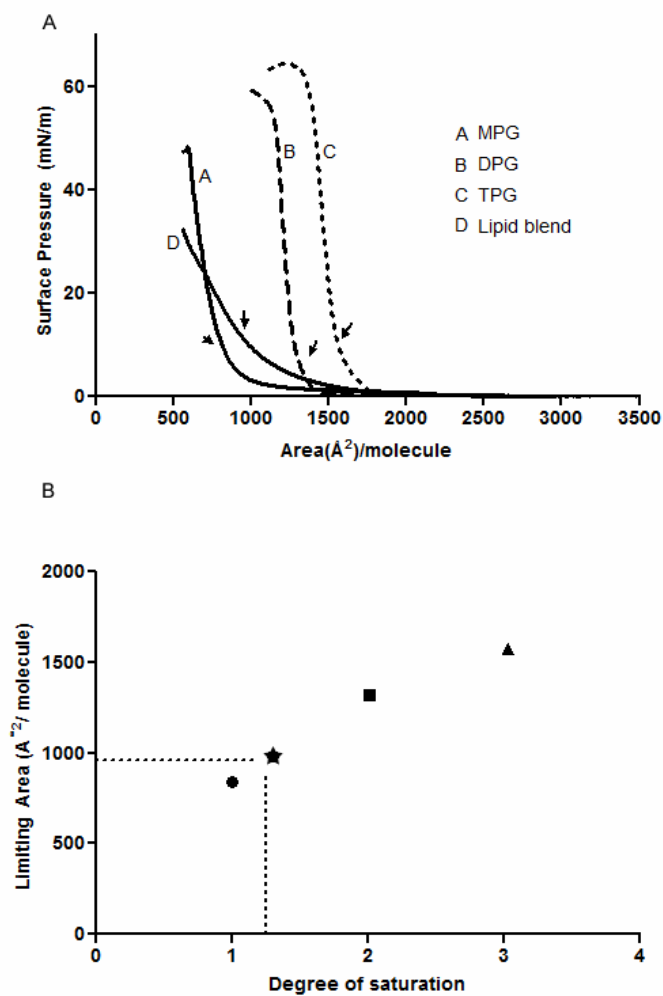


Figure 18. (a) Surface pressure-area (π -A) isotherms and (b) limiting packing area (A_{lim}) of mono-, di-, and tripalmitoyl glycerol (MPG, DPG, TPG, respectively) and the lipid blend. A_{lim} of MPG, DPG, and TPG was dependent on the degree of saturation (MGP=1, DPG =2, TPG =3)(b).

extended to the established linear relationship, the lipid blend exhibited a 1.3 degree of saturation, suggesting that the predominate molecules in the lipid blend, mono-glycerols, exhibited more influences on molecular orientation as the extrapolated degree of saturation is closer to that of MPG than DPG (Figure 18b).

The lipid blend which possesses varying degrees of saturation and hydrocarbon chain length, packs less rigidly than those of its individual components as evident of the extended LE in its π -A isotherm (Figure 18). This is not unexpected given the diversity in its composition. The differences in hydrocarbon length and kinks and head group polarity give rise to a more fluid and irregular templating surface. This corrugated surface(134) can provide “pockets” for precursor Fe(III)PPIX dimers to intercalate in order to assemble, initiating hemozoin nucleation. Furthermore, the increase in packing fluidity can justify the existence of the lipid blend complexity. If one type of lipid is sufficient to template hemozoin formation,(58, 97) why does the parasite command a composition of five different lipid components? The answer is likely to be associated with the increase in surface energy associated with the template surface. Ongoing research is being performed to examine the kinetics of beta-hematin formation under lipid blend mediation. Comparison of the rate and activation energy associated with the lipid blend to that of its individual components may explain the use and the uniqueness of the lipid blend during *in vivo* hemozoin formation.

Neutral lipid-Fe(III)PPIX packing

While Fe(III)PPIX is insoluble in aqueous solutions, it is soluble in lipid environments. Investigation of beta-hematin formation under lipid mediation revealed that crystallization occurs at the interface of lipid bodies and water. Importantly, the rate of Fe(III)PPIX conversion at the

interface is rapid enough to account for Fe(III)PPIX toxicity.(58, 97) However, on a molecular level, little is known about the interactions that occur during this process, especially during crystal nucleation. To further examine the behaviors of lipid and Fe(III)PPIX molecules at the interface, LB compressions were performed deposits of lipid blend-Fe(III)PPIX. The introduction of Fe(III)PPIX to the lipid blend resulted in shift to higher molecular area of the π -A isotherm (~ 1085 to $1353 \text{ \AA}^2/\text{molecule}$). This lipid blend-Fe(III)PPIX isotherm exhibited a much expanded LE phase (Figure 18). The transition from LE-LC of the mixed solution occurred at slightly higher area ($1303 \text{ \AA}^2/\text{molecule}$) than that of the lipid blend alone ($1078 \text{ \AA}^2/\text{molecule}$). However, lifting of the lipid blend-Fe(III)PPIX isotherm started at $2812 \text{ \AA}^2/\text{molecule}$, suggesting that the introduction of Fe(III)PPIX encouraged weak interactions between the lipid molecules at high molecular area. The maximum pressure increased by 8 mN/m , from 32 to 40 mN/m upon the addition of Fe(III)PPIX. Here, the early transition to the LE phase upon the incorporation of Fe(III)PPIX is interpreted as the interaction of Fe(III)PPIX to the lipid molecules.

Efficient interactions of lipid molecules and Fe(III)PPIX that promote crystallization favor a less organized lipid-Fe(III)PPIX packing state. This packing state is pH dependent (Figure 20). To examine the contribution pH to the packing of lipid-Fe(III)PPIX, compressions of premixed Fe(III)PPIX- lipid blend on citric buffer subphase at varying pH (1.5, 3.0, 4.0, 5.0, and 7.0) were performed. At pH 3.0-5.0, packing isotherms exhibited extended LE phase with a limiting area of roughly $824 \text{ \AA}^2/\text{molecule}$ (Figure 20), suggesting a loose ordered packing. Outside this pH range, pH 1.5 and 7.0, the isotherm curves shifted to the right with a limiting area of $940 \text{ \AA}^2/\text{molecule}$. The maximum packing pressure for the samples at pH 1.5 and 7.0 were nearly twice

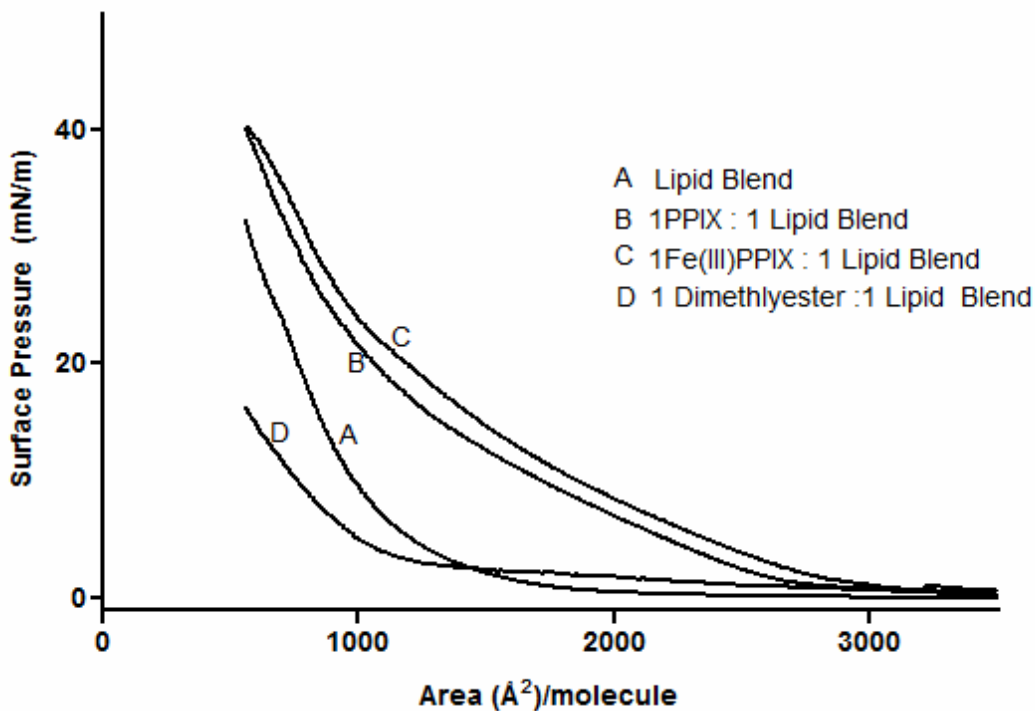


Figure 19. Pressure-area (π -A) of lipid blend and protoporphyrin-lipid blend mixtures at 100 μ M. Introduction of Fe(III)PPIX to lipid blend created an extended liquid expansion phase at higher molecular area. The removal of the iron center of Fe(III)PPIX produced little change to this shift. However, the replacement of the propionic group produced a shift to lower molecular area. Unlike the isotherm plot of the LB which exhibited a distinct liquid condense phase, the isotherm plot of dimethlyester PPIX-lipid blend revealed a more liquid-expanded phase, suggesting that Fe(III)PPIX-lipid interactions occur via the propionic group of Fe(III)PPIX and polar head group of the lipid molecules.

as those of pH 3.0, 4.0, and 5.0. Rigid packing was observed for compressed monolayer at pH 1.5 and 7.0. In conjunction to published *in vitro* studies of beta-hematin formation by monoglycerols that reported a pH bell-shape dependence (~2.5-6.0) for crystallization,(91, 97) packing studies presented here suggest that weak interactions between lipid molecules is necessary to template hemozoin formation. A_{lim} values of 894 and 888 Å²/molecule were extrapolated from π -A isotherms at pH 1.5 and 7.0. However, at pH 3.0, 4.0, and 5.0, A_{lim} values were 718, 743, and 750 Å²/molecule. At 1.5 and 7.0 pH, lipid molecules interact at higher molecular area, suggesting that at these pH, better packing existing between molecules. The solutions exhibiting high disorder include those with a pH similar to that of the parasite's digestive food vacuole (~4.8), the site of *in vivo* hemozoin crystallization. Under low pH condition (< 2), both propionic groups of Fe(III)PPIX are predominately un-ionized, giving the molecule an overall charge of +1. Under high pH (>6) condition, both groups are ionized, giving the Fe(III)PPIX an overall charge of -1. At pH 1.5 and 7.0, the charged molecules of Fe(III)PPIX are available to participate in electrostatic or salt bonding with the lipid molecules, resulting in stronger packed monolayer and LE-LC transition at higher molecular area. Beta-hematin crystallization occurs optimally under conditions in which one propionic acid is predominately ionized and the other predominantly un-ionized (pH 2.5-6.5).(90, 91, 97) Under conditions in which both groups are predominantly un-ionized (lower pH) and both are ionized (higher pH), no beta-hematin is formed. Only at the pH range of the digestive vacuole (~4.8) will Fe(III)PPIX be able to interact with the lipid molecules to form hemozoin.(91, 97)

To assess which component of the Fe(III)PPIX molecule interacts with the lipid bodies, π -A compression measurements were performed with the lipid blend and various substituted porphyrins. An isotherm similar to that of lipid blend-Fe(III)PPIX was measured for the

compression of lipid blend-PPIX (Figure 19). The molecular contact involved during Fe(III)PPIX-lipid blend interaction was preserved for the compression of PPIX-lipid blend, suggesting that the center iron does not interact with the lipid. However, the substitution of the dimethylester group for the propionic group produced an isotherm shift slightly to the left of the lipid blend isotherm curve. The lipid blend-dimethylester isotherm displayed an expanded LE phase with a reduced pressure maximum of 16 mN/m, indicating that limited interactions between molecules only occur at low molecular area. The lipid blend-dimethylester PPIX isotherm is interpreted as limited or no interaction occurring between lipid molecules and dimethylester PPIX. The removal of the propionic group disrupted this interaction, as evident with a strong shift of the isotherm curve to the left. Together, the substituted PPIX study proposed that lipid-Fe(III)PPIX interactions occur via the propionic group of the Fe(III)PPIX.

In light of recent investigations of neutral lipid mediation of beta-hematin formation at the lipid-water interface, (97) the substituted PPIX compression study provides further details of molecular interaction involved during this crystallization process. Experimental data provided here suggest that crystal nucleation begins with the anchoring of a Fe(III)PPIX precursor to the lipid group at the lipid-water interface. In an aqueous environment, where competing hydrogen bonds occur, molecular dynamic (MD) simulations reveal that the beta-hematin precursors rapidly rearrange to form π -stacked dimer of H₂O-Fe(III)PPIX (58). The formation of this beta-hematin precursor involves an increase in the lateral shift between the porphyrins and electrostatic interaction of the negatively charged propionate of one H₂O-Fe(III)PPIX with the positively charged Fe(III) center of the other. In this form, the propionate group interacts with solvent molecules rather than the

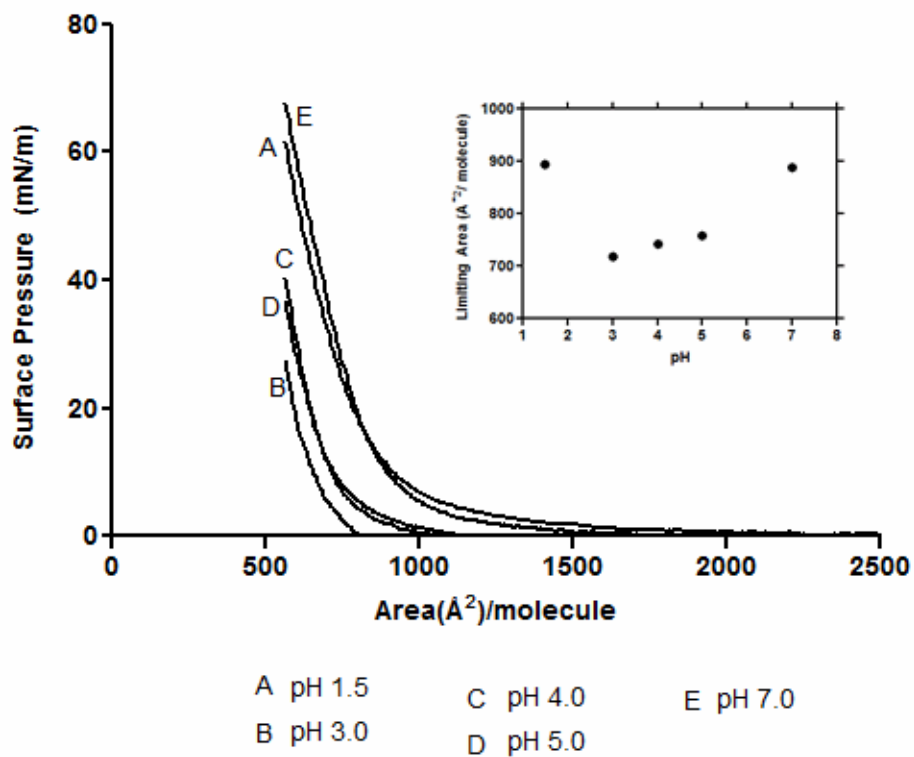


Figure 20. PH dependence of lipid blend-Fe(III)PPIX packing. Packing of Fe(III)PPIX-lipid blend is more ordered at pH 1.5 and 7.0. A more disordered packing was observed for pH 3.0, 4.0, and 5.0. Limiting area is highest at flanking pH (1.0, 7.0). In conjunction with *in vivo* examination of beta-hematin formation,(97) packing studies suggest that beta-hematin formation favors a disorder arrangements of lipid blend-Fe(III)PPIX.

Fe(III) center. Within the aqueous environment, the hydrophobic tail of the neutral lipids will likely favor an organization that includes the hydrophilic head group exposed to the aqueous environment with the hydrocarbon tail towards the interior of the lipid body. In this arrangement, the hydrophobic head group is available to anchor the precursor Fe(III)PPIX dimer, via the propionic group, to initiate crystal nucleation via the {100} or {010} faces (45, 89, 97). Conversion of the anchored dimer precursors to beta-hematin requires only a ligand exchange process with bond formation from the propionate O to Fe(III) with the displacement of the H₂O from the opposite face of each porphyrin (58). In the presence of completing water hydrogen bond to the axial center of Fe(III)PPIX unit, these units cannot coordinate to form the hemozoin Fe-O dimer precursor, as demonstrated by Egan *et al.* using computational modeling (58). Instead, in the aqueous environment, Fe(III)PPIX units form π dimers with water molecules acting at the axial ligand. However, within the hydrophobic environment of the lipid layer, the hydrophobic Fe(III)PPIX is sheltered from the water molecules, allowing the dimers to come together to nucleate the crystal. Crystal nucleation is likely to occur through seeding of anchored Fe(III)PPIX unit to the polar lipid head group. Crystal growth is then hindered by the geometry of the lipid bodies. The tapering off morphology and uniformity of hemozoin size in nature is likely a result of the curvature of these lipid bodies. This model, as depicted in Scheme 6, is an updated version of the model presented in chapter II (97). Though interfacial growth is a possible model, it seems unlikely in light of compression studies and Fe(III)PPIX partition data.

Anti-malarial interactions

Traditional anti-malarials, such as chloroquine (CQ), a drug that is no longer effective as a result of drug resistance, function by thwarting hemozoin formation. This process is proposed to

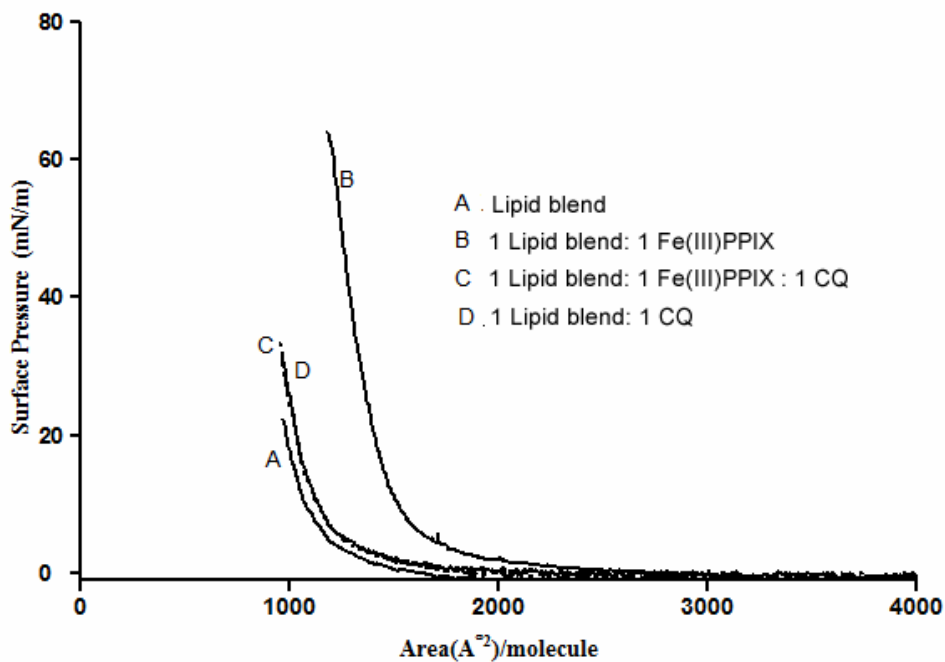


Figure 21. Langmuir compression of premixed CQ, Fe(III)PPIX, and lipid blend. The addition of Fe(III)PPIX to the lipid blend increased the lipid molecules packing stability, as indicated by an isotherm curve shift to higher molecular area (b). Compression of lipid blend-Fe(III)PPIX in the presence of CQ produced an isotherm similar to that of just the lipid blend (c), suggesting that CQ disrupts the Fe(III)PPIX-lipid interactions. Little interaction occurred between the lipid blend and CQ as indicated by the isotherm of premixed CQ and lipid blend resembling the isotherm of the lipid blend(d).

occur via formation of π - π complex between Fe(III)PPIX and these drugs in solution.(135) It is thought that CQ operates by intercalating its quinoline rings between the aromatic groups of the beta-hematin molecules and stereochemically capping onto the {001} surface of the crystal via (porphyrin) acid-amine (quinoline) salt bridge (45, 49). To examine the molecular interactions of CQ, lipids, and Fe(III)PPIX these samples were spread onto aqueous citric buffer subphase. The isotherm of the lipid blend-CQ displayed a slight shift to higher molecular area from the lipid blend π -A curve with a slight increase in maximum pressure (Figure 21). Interestingly, when Fe(III)PPIX was premixed with CQ and lipid blend, an isotherm identical to that of the lipid blend-CQ was measured. The compression of CQ and lipid blend produced an isotherm similar to that of just the lipid blend (Figure 21). These results suggest that the presence of CQ interrupted the interactions between lipid and Fe(III)PPIX and that minimal interactions existed between CQ and the lipid layer. Current proposal for hemozoin formation involves crystal formation in close association to lipid bodies within the digestive food vacuole of *P. falciparum*. Thus, for proper antimalarial functionality, CQ must partition into the lipid layer. To examine the localization of CQ to the lipid bodies, synthetic neutral lipid bodies (SNLB) were produced by depositing the lipid blend onto an aqueous buffer and were tagged with the hydrophobic dye Nile Red. Confocal imaging showed that these SNLBs were identical in shape, size, and composition as those in nature (Figure 22b,c) (57, 73, 97). The addition of approximately 625 μ M CQ to this SNLB system produced no significant fluorescence change (Figure 22b,c). Fluorescence spectra of mixed CQ and SNLB explained confocal observation. In particular, the addition of CQ to the SNLB-NR system produced an increase in NR fluorescence intensity (Figure 22a). The introduction of 100 μ M CQ to the SNLB-NR system resulted in an increase in fluorescence intensity by 43% (Figure 22a). Given the electron-rich structure of CQ, the close proximity of

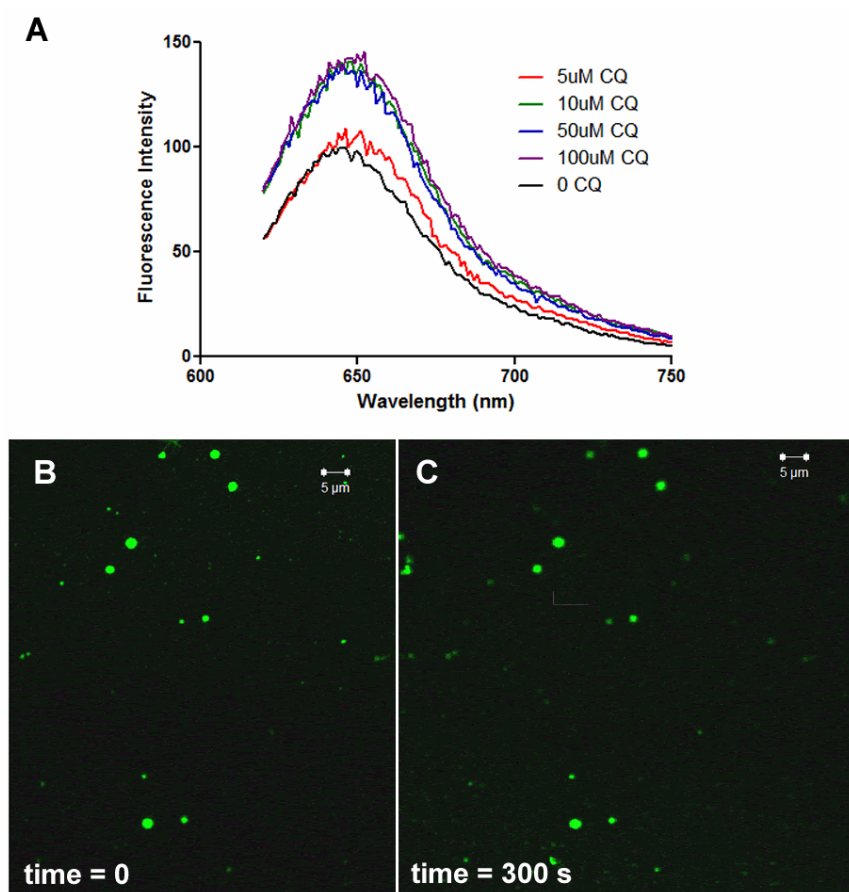


Figure 22. Fluorescence spectra of synthetic neutral lipid body (SNLB) tagged with the hydrophobic dye, Nile Red (NR). The addition of CQ to 100 μ M SNLB produced an increased in fluorescence intensity (a), suggesting the presence of an electron transfer from CQ to NR. Confocal imaging (b,c) confirmed fluorescence spectra analysis by demonstrating that the addition of 625 μ M CQ over the period of 300 second (c) does not significantly quench SNLB-NR fluorescence.

CQ and the π -acceptor NR, it is likely that a charge transfer from CQ to NR produced the observed fluorescence intensity increase. Here, the increased in NR fluorescence indicates that CQ spontaneously localizes to the SNLB. However, this scenario changed with Fe(III)PPIX was introduced to this system. When a premixed CQ and Fe(III)PPIX solution was added to the SNLB-NR, NR quenching was observed (Figure 23), suggesting an energy transfer from NR to Fe(III)PPIX. Previous infrared spectroscopy examination of CQ during beta-hematin formation revealed that Fe(III)PPIX and CQ form complexes (136) with a 2 equivalent of Fe(III)PPIX to 1 equivalent of CQ(137), preventing binding to Fe(III)PPIX from axial both face of Fe(III)PPIX. During the premixing stage, CQ and Fe(III)PPIX formed a complex that includes both axial face of Fe(III)PPIX capped by CQ (136, 137). When this solution was introduced to the SNLB-NR system, the hydrophobic CQ-Fe(III)PPIX-CQ complex favored a localization with the hydrophobic lipid environment as evident in observed NR quenching. Despite the localization of Fe(III)PPIX to the lipid bodies, no beta-hematin was formed. This is not unexpected given that beta-hematin is thought to be formed when two Fe(III)PPIX molecules complex to form a dimer. These dimers hydrogen bond with neighboring dimers to produce the macroscale crystal. In the presence of CQ, Fe(III)PPIX molecules are capped and cannot form the necessary bonds to initiate crystal nucleation. Together, compression studies of lipid and CQ in conjunction with fluorescence analysis provided further insight to CQ's mechanism of action. Here, data suggest that CQ functions *in vivo* by preventing crystal growth and not by direct interaction with lipid bodies. The interruption of Fe(III)PPIX-lipid interaction via CQ-Fe(III)PPIX-CQ complex, will inhibit crystal nucleation which leads to the accumulation of toxic Fe(III)PPIX, leading to the death of the parasite.

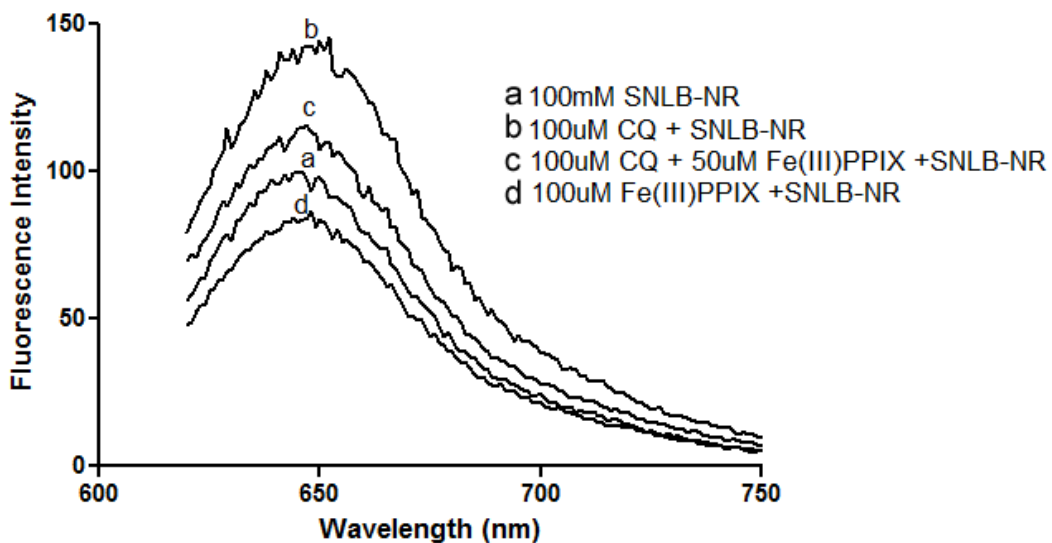
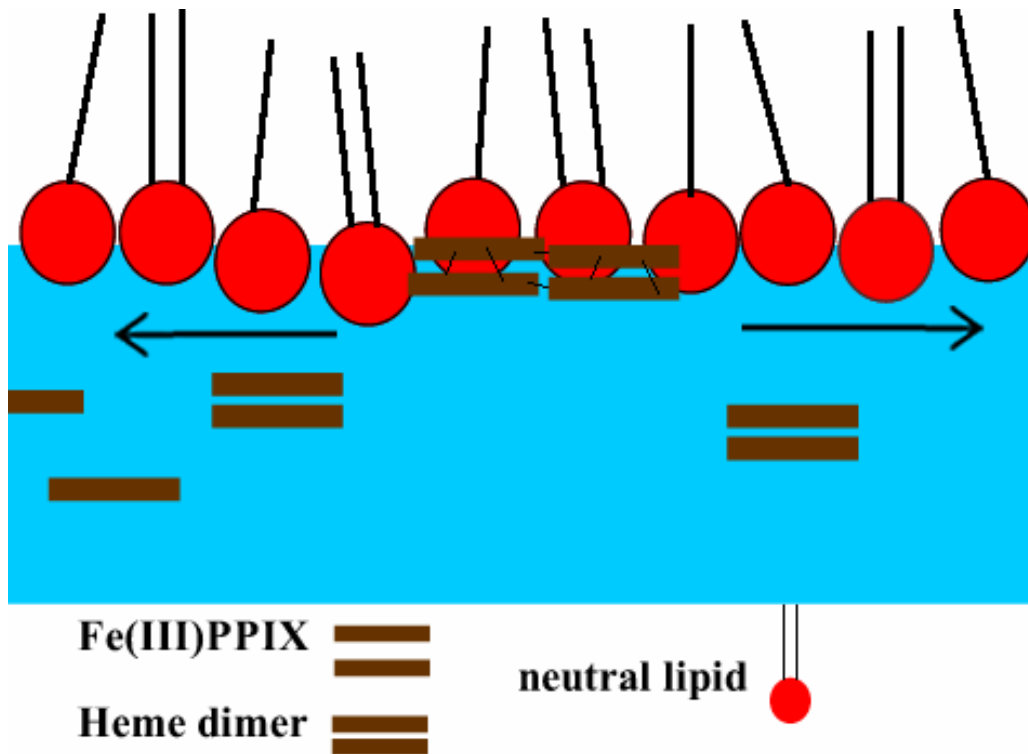


Figure 23. Fluorescence spectra of chloroquine (CQ) and Fe(III)PPIX and the Nile Red (NR) labeled synthetic neutral lipid body (SNLB) system. The introduction of CQ to SNLB-NR produced an increase in fluorescence intensity (a, b), suggesting that CQ spontaneously localized at the SNLB. The addition of premixed CQ and Fe(III)PPIX decreased this fluorescence (c); however, this fluorescence intensity is still more than that of just SNLB-NR and Fe(III)PPIX. Together, these data indicate that CQ functions by inhibiting hemozoin crystal nucleation. The pre-formed CQ-Fe(III)PPIX-CQ complex prevents Fe(III)PPIX molecules from assembling by capping both axial faces of Fe(III)PPIX.



Scheme 6. Proposed lipid-Fe(III)PPIX interaction during hemozoin formation. Precursor Fe(III)PPIX dimers are formed in the aqueous environment. In the absence of competing water molecules, hemozoin nucleation occurs when these dimers come together at the interface. Crystal growth occurs parallel to the interface.

Conclusion

The examination of interfacial packing of the lipid blend, a lipid mixture associated with the formation of the malaria pigment in nature, has demonstrated the uniqueness of this mixture. Namely, the lipid blend packs into an extended liquid expanded state with weak interactions between lipid molecules. The lipid blend's unique packing property is attributed to its complex composition. This high energy condition accounts for the low activation energy associated with *in vitro* synthesis of synthetic hemozoin, beta-hematin, under the mediation of the lipid blend by increasing the rate of crystal nucleation. In conjunction to reported studies of beta-hematin formation, less ordered packing of lipid molecules and Fe(III)PPIX is optimal for crystallization. This optimal packing occurs within the pH range of 3.0-5.0. Results from the substituted protoporphyrin IX (PPIX) study proposed that nucleation initiates via the anchoring of the propionic group of Fe(III)PPIX to the polar head group. Finally, this study provides preliminary details into the investigation of chloroquine interaction at the lipid-water interface. LB packing analysis reveals that minimal interaction exists between lipid and CQ and supports the current hypothesis that chloroquine functions by capping hemozoin extension (49, 135, 138). This study illustrates the effectiveness of LB techniques to investigate molecular interactions at the lipid-water interface during hemozoin formation.

Section Acknowledgements

The work in this chapter cannot be complete without the help of Dr. Xu Yan and Dr. Yibin Zhang. They have donated their time to train me on the LB. In addition, I also like to thank

Vanderbilt Institute of Nanoscale Science and Engineering (VINSE) for access to Langmuir-Blodgett trough which was donated by Bristol-Myers Squibb with help from Professor C. David Weaver. Special thanks to Leslie Hiatt for her detailed proof reading and fruitful data discussion.

Chapter IV

CRYSTAL ENGINEERING: SOLVENT EFFECTS ON BETA-HEMATIN FORMATION

Heme (ferriprotoporphyrin IX - Fe(III)PPIX) is an ubiquitous and essential molecule which plays key biological roles in processes like oxygen transport, respiration, photosynthesis and drug detoxification (28, 139, 140). Despite this, heme is also capable to cause a number of cellular deleterious effects (141). Blood feeding organisms implicated in malaria, schistosomiasis, and Chagas' disease, namely, the malaria parasite *Plasmodium falciparum*, the worm *Schistosoma mansoni*, and the kissing bug *Rhodnius Prolixus*, produces free heme as a byproduct of their digestion of large quantities of hemoglobin (Hb) to meet their nutritional requirements (15). It is believed that the same lipid composition is present in all model system. To circumvent heme toxicity, these organisms have evolved a detoxification mechanism that converts toxic heme into a non-toxic hemozoin (23, 142). Powder x-ray diffraction of this crystal revealed a triclinic unit cell with a space group of $P\bar{1}$ (41). The macroscopic crystal is comprised of heme (Fe(III)PPIX) dimers formed through reciprocal iron-carboxylate bonds (42), where the propionic side chain of a porphyrin coordinates with the axial Fe of another. The dimers then hydrogen bond to form an extended network of dimers (41). As previously previewed in chapter III, the significance of hemozoin lies in its association with antimalarial functionality. In *Plasmodium*, antimalarial key drugs such as chloroquine function by disrupting this heme detoxification pathway. Inhibition of heme conversion results in the accumulation of toxic free heme, which leads to parasite death. Understanding the molecular details of hemozoin formation may provide insight to future anti-malarial designs.

Due to the labor intensive process involved in obtaining hemozoin from model animals, the field of hemozoin research has relied heavily on synthetically produced hemozoin known as beta-hematin. Chemically (42) and structurally (41), hemozoin and beta-hematin are identical. Various synthetic routes have been proven successful in crystal mediation, including benzoic acid (90), acetic acid (91), neutral lipids (58, 73, 97), detergents (143), and alcohol (87) –based systems. All these methods require the introduction of soluble heme to a crystal mediating system. However, limited data is available on the comparability of beta-hematin produced using these various system. Hemozoin found in nature possesses a conserved molecular structure. Crystal morphologies differ significantly among *Plasmodium*, *Schistosoma*, and *Rhodnius*. Crystals obtained from *Plasmodium* are very regular in shape with well defined crystal faces. *S. mansoni* hemozoin are heterogeneous in size, ranging from 50 nm to a few micrometer in diameter, with a spherical shape (44, 77). Hemozoin crystals from *R. prolixus* exhibit irregular surface topography and are generally much larger than crystals obtained from *Plasmodium* (44, 144). The reasons behind this non-homogeneity in crystal morphologies remain unclear; however, it is likely related to the *in vivo* mediator of crystal formation.

This study provides a systematic approach for investigating the mechanisms of chemical reactions in solutions that lead to beta-crystal nucleation. The works presented in this chapter were performed in a collaborative effort with Dr. Marcus Oliveira and Renata Stiebler from Universidade Federal do Rio de Janeiro (Brazil) and Dr. Timothy Egan from The University of Capet Town (South Africa). This study investigates the role of increased dissociation of acid heme precipitates by reducing the medium polarity plays a role on *in vitro* beta-hematin formation. The data presented here support the notion that reduction in medium polarity

increases the steady-state levels of soluble heme in acidic milieu, accelerating heme crystallization. In addition, beta-hematin crystal morphologies were correlated to solvents' water miscibility and polarity properties. The controllability of crystal habits through the manipulation of solvent selection was also examined. The ability to control crystal morphologies during beta-hematin applications such as antimalarial drug screening (143, 145) and disease detection (146) may be advantageous. Solvent effects on crystal habits can be exploited to maximize molecular targets.

Materials and Methods

Materials

All materials used were of analytical grade or of the highest grade of purity available from commercial suppliers. HEPES, sucrose and *Polyethylene glycol (PEG)* (PEG 300; PEG 3.350; PEG 6.000; PEG 8.000; PEG 20.000; PEG 22.000) were purchased from Sigma Chemical Co. (St. Louis, MO, USA). Pyridine, acetonitrile, dimethyl sulfoxide (DMSO), sodium acetate, sodium bicarbonate, sodium acetate, glacial acetic acid, and others reagents were obtained from (Merck, Darmstadt, Germany) and used without further purification. All other reagents were of analytical grade. All water used in the study was of ultrapure grade.

For morphology studies, the following solvents were used: dimethyl sulfoxide (DMSO), dimethylformamide (DMF), tetrahydrofuran (*THF*), dichloromethane (DCM), acetonitrile (meCN), chloroform (CF), toluene, and hexane (Table 1). For all beta-hematin morphology studies, 1 mg of hemin chloride (Sigma) were used unless otherwise stated. Citrate buffer (CB) at pH 4.8 and 50mM was used as the aqueous medium in crystallization studies. Previous studies

by Egan(58) have shown that this buffer does not mediate beta-hematin formation and will not accelerate crystal formation as does the widely used acetate buffer (91).

Spectroscopy and electron microscopy studies

In PEG-induced reactions, the final products were purified by using 0.1M sodium bicarbonate buffer, pH 9.1 washing steps as previously described.(49) FTIR spectra of undried material were recorded between 2000 cm^{-1} and 1000 cm^{-1} and were carried out as Nujol mulls in a Thermo Mattson Satellite FTIR. XRD measurements of pigments induced by DMSO-driven reactions, were performed in undried samples in a Huber Imaging Plate Guinier Camera 670 (58) in the 2theta range $4\text{--}30^\circ$ using Cu-K α radiation ($\lambda=1.5418\text{ \AA}$) operating at 20 mA and 40 kV, with a step 75 resolution of 0.005° . For PEG-induced reactions, XRD analyses of purified dried pigments were performed using Cu K α radiation ($\lambda = 1.541\text{ \AA}$), with data collection on a Scintage Instrument with vertical goniometer in the 2theta range $5\text{--}40^\circ$ using a silicon sample holder. Scanning electron microscopy (SEM) was used to investigate the external morphology of the beta-hematin produced. Finely ground samples were sprinkled onto aluminum stubs pre-coated with an almost dry carbon and glue mix. Excess sample was then removed before the samples on the stubs were sputter-coated with gold–palladium, and finally examined with a Leica S440 Scanning Electron Microscope (for DMSO-induced pigments) and a Hitachi S-4200 (Japan) Scanning Electron Microscope (for PEG-induced pigments).

Heme solubility in solvent: aqueous system

The effect of different DMSO and polyethyleneglycols (PEG) on heme solubility was assessed by two different approaches: the first one by measuring the light absorption of Soret

band and the second one by using the alkaline pyridine method (147). For both methods, heme (100 μ M) was added to sodium acetate buffer containing DMSO or PEG in polypropylene (1.2 mL) tubes and were shaken for 10 minutes at room temperature. Then, the tubes were centrifuged for 10 minutes at 17.500 \times g and the supernatants collected. For the first procedure, all the supernatants were analysed by light absorption wavelength scan between 300 nm and 800 nm, which were carried out in a GBC-920 spectrophotometer (GBC, Australia). To quantify heme, an aliquot of 300 μ L from supernatants were added to 700 μ L of alkaline pyridine solution (20 % (v/v) of 1 M NaOH; 48 % (v/v) pyridine; 32 % (v/v) MiliQ water). The samples were analyzed by light absorption wavelength scan between 500 nm and 600 nm in a GBC-920 spectrophotometer (GBC, Australia).

The effect of different organic solvents on heme solubility was assessed by light absorption analysis. Hematin porcine was added to 1:1 CB: solvent (by volume) to produce a 100mM solution. The sample was centrifuged for 10 minutes and the supernatants were collected. UV-vis absorption as collected from 300-800nm using an Aligent 8453 spectrophotometer. To quantify light absorption results, the effect of different organic solvents on heme solubility was further assessed using the alkaline pyridine method.(147) Heme (100 mM) was added to CB containing DMSO, DMF, THF or MeCN (50% v/v) in polypropylene (1.2 mL) tubes and was shaken for 10 minutes at room temperature. Then the tubes were centrifuged for 10 minutes at 17.500 \times G and the supernatants were collected. To quantify unreacted heme, an aliquot of 300 mL from supernatants were added to 700 μ L of alkaline pyridine solution (20 % (v/v) of 1 M NaOH; 48 % (v/v) pyridine; 32 % (v/v) MiliQ water). The samples were then analyzed by light absorption (500nm-600nm) on a GBC-920 spectrophotometer (GBC, Australia). Due to the presence of a biphasic solution produced by toluene, DCM, and CF,

solubility measurement were performed only with water miscible solvents (DMSO, DMF, THF, and MeCN).

Beta-hematin formation and characterization

Spontaneous heme crystallization reactions under DMSO and PEG mediation were carried out in polypropylene tubes in the presence of 0.5 M sodium acetate buffer, pH 4.8, 100 μ M hemin, previously prepared in 0.1 M NaOH as 10 mM stock solutions, with a final volume of 1.0 mL. Tubes were kept for different times at 37°C. To evaluate the role of organic solvents on heme crystallization, different concentrations of DMSO, PEGs or acetonitrile were added previously to sodium acetate buffer before reactions were started. Then, the pH of all solutions were measured and adjusted to give an apparent pH 4.8, accordingly. The beta-hematin produced was determined by washing the pellet with “*extraction buffer*” (0.1 M sodium bicarbonate and SDS 2.5 %, pH 9.1), solubilizing it in 0.1 M NaOH and measuring the amount of heme spectrophotometrically at 400 nm (81). Kinetics of heme crystallization using Tween 20 were performed under the same conditions, at concentrations of 0.1 μ M, 2 μ M and 60 μ M.

Solvent effects on beta-hematin morphologies were investigated by adding 1mg of hematin porcine to a solution of 1:1 ratio of CB: solvent (by volume) in a glass vial. The sample was sonicated for 5 minute to help facilitate heme solubility and then placed in an incubator at 37°C for 12 hr. Products collected at the end of incubation period were characterized by Fourier transformed infrared (FTIR) spectroscopy of undried material as Nujol mulls. Powder X-ray diffraction (XRD) of the extensively washed dried product, and scanning electron microscopy (SEM) imaging of samples were also performed. XRD was carried out using Cu K α radiation ($\lambda=1.541 \text{ \AA}$), with data collection on a Philips PW1050/80 vertical goniometer in the 2 θ range 5

– 40° using an Al sample holder. Images of crystal products were obtained from a Hitachi S-4200 scanning electron microscope (SEM). To access the temperature's effect on crystal morphologies, 1mg of hematin porcine was added to 500 μ L CB: 500 μ L DMSO and allowed to incubate at room temperature (22 °C), 37 °C, or 80 °C for 12 hrs. Samples were washed and characterized as described above.

The rate of beta-hematin formation under solvent mediation was examined by combining 1mg of hematin porcine with 500 μ L CB: 500 μ L solvent (DMSO, DMF, THF, or MeCN). The solution was sonicated and centrifuged for 10 minutes to remove amorphous heme. The supernatant was collected and used as a stock solution. Aliquots of 100 μ L were transferred to 1mL glass vials and incubated at 37°C. The reaction was quenched at various time points by the addition of 20 μ L of a 30% pyridine solution (30% pyridine, 40% acetone and 200 mM HEPES buffer (HEPES - 4-(2-hydroxyethyl)-1-piperazineethanesulfonic acid, pH 7.5)). The sample was then transferred to a 1.5mL polypropylene tube and centrifuged. 50 μ L of the sample and 50 μ L of water were transferred to a 96 well plate with read at 405nm on a Biotek Synergy HT multi-mode microplate reader. The percentage of beta-hematin conversion was calculated as previously described(79) and analyzed using GraphPad Prism 4 to obtain the half-life of each solvent. All data sets were performed in triplicate.

For pH studies of solvent mediated heme conversion, similar experimental setup were performed for DMSO, DMF, THF, and MeCN. The final pH of the combined system was carefully adjusted using minimal solutions of sodium hydroxide (NaOH) and hydrochloric acid (HCl). The reaction was allowed to incubate for 12 hrs at 37 °C. Quenching and quantification of heme conversion was performed as described above.

Solvent surface tension measurements

Surface tension of citrate buffer (pH 4.8, 50mM), and a 1:1 ratio of citrate buffer: solvent (by volume) was measured. Measurements for water miscible solvents, DMF, DMSO, THF, and MeCN were performed using a Sigma 700 produced by Gamry Instrument with wetting depth set at 6.0 mm.

Osmolality measurement

Solutions with 1 and 10 % of DMSO was prepared in acetic acid butter pH 4.8. Measurements were performed on a VAPRO 5520 vapor pressure osmometer (Discovery Diagnostics, Canada).

Data analysis

Kinetics of beta-hematin reactions were analysed by using linear least-squares fitting methods with the program GraphPad ©Prism 5.0. The data were fitted according to Avrami equation [34]:

$$v = v_0 + \left[v_{\infty} \left(1 - e^{-zt^n} \right) \right]$$

where v is the amount of beta-hematin formed (in nmols), v_{∞} is the amount of beta-hematin present at the beginning of the reaction, v_{∞} is the amount of beta-hematin formed at completion of the reaction, z is the rate constant and n is the Avrami constant. For a process in which growth occurs along an interface between the two interconverting phases, as is likely to be the case for beta-hematin formation in this model reaction, n takes an integer ranging between 1 and 4. Water activity analyses were done by using the following equation (148):

$$a_w = 1000/MW_{water}/(1000/MW_{water} + Cosm),$$

where MW_{water} is the molecular weight of water and $Cosm$ is expressed in $Osmol\ kg^{-1}$.

Comparisons between groups were done by the non-paired Student's t-test or one-way ANOVA analysis of variance and *a posteriori* Tukey's test for pairwise comparisons. The results were expressed as mean±standard error and considered significantly different at $p < 0.05$ as indicated in figure legends. Student's t-test, ANOVA, Tukey's test and correlation analysis were performed by GraphPad Prism 5.0 software.

Results and Discussions

Part I) Increase on the steady-state soluble heme levels in acidic conditions is an important mechanism for spontaneous heme crystallization *in vitro*

Part II) Crystal Engineering: solvents effect on beta-hematin morphology

Part I

Increase on the steady-state soluble heme levels in acidic conditions is an important mechanism for spontaneous heme crystallization *in vitro*

DMSO promotes heme solubilization and further crystallization into beta-hematin.

It is well known that *in vitro* heme forms highly insoluble aggregates at acidic conditions, such as those found inside *Plasmodium* parasites food vacuoles.(49, 147) Among the physico-chemical requirements for heme crystallization, a pH close to the heme pK_a (4.8) is of foremost

importance (42, 91, 149). However, an interesting aspect related to heme crystallization reactions conducted in aqueous medium, is that amorphous heme precipitates are slowly converted into organized beta-hematin crystals, which presumably occurs by increasing heme solubilization (87, 91, 150). In fact, Egan and co-workers recently demonstrated that heme and water spontaneously form a complex in aqueous medium, which depends on the interaction of the carboxyl group with the central iron of heme (90). Therefore, a proposed model suggested that, to produce beta-hematin crystals, heme dimers bound to each other by means of reciprocal iron-carboxylate linkage, would require the displacement of the axial water molecule bound to the porphyrin. (58, 91) Strengthening this proposal, alcohols accelerated spontaneous beta-hematin formation *in vitro* (87, 151) in reactions that depend on the hydrophobicity of these compounds and their ability to solubilize heme (87). However, spontaneous heme crystallization was also promoted by benzoic acid in a mechanism that does not involve solubilization of acid heme precipitates (90). Therefore, to assess whether reduction of the medium polarity would influence spontaneous heme crystallization, the effect of the aprotic solvent DMSO on heme solubility in acid conditions was investigated. For this sake, heme was incubated in the presence of different DMSO concentrations (4,6 % to 27,7 %) in sodium acetate buffer at an apparent pH 4.8 during 10 minutes and then centrifuged. Figure 24a shows the UV-visible absorption spectra of the supernatant obtained after centrifugation of heme in the presence of different DMSO concentrations, acquired between 300 nm and 800 nm. UV-vis spectroscopy analysis demonstrated that DMSO increased the Soret absorption band of heme (around 400 nm) in a concentration-dependent manner, suggesting an increase of heme solubility in conditions of reduced medium polarity. In order to confirm this finding, quantification of heme in the supernatants by a more reliable method (the alkaline pyridin), indicated that DMSO increased in

about ten times the levels of soluble heme in acidic medium (Figure 24b). Also, a strong positive correlation ($r^2 = 0.6480$, $p < 0.0001$) between the amount of solubilized heme and the DMSO

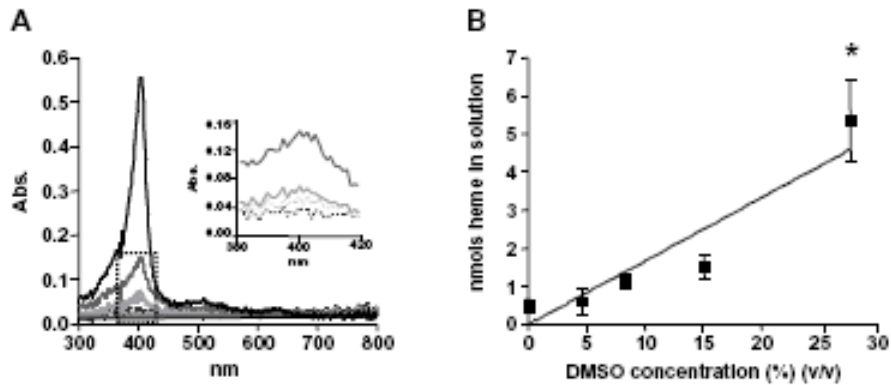


Figure 24. DMSO promotes spontaneous heme solubilization. (A) Different concentrations of DMSO in 0,5 M sodium acetate buffer pH 4,8 and 100 μ M heme were shaken for 10 minutes and centrifuged at 10.000 x g. for 10 min. The supernatants were analyzed by uv-visible spectroscopy between 300 nm and 800 nm. A magnification of the dotted box is shown in the inset. Dashed line black: control; dashed line gray: 4.6 % DMSO; pale gray: 8.3 % DMSO; dark gray: 15.1 % DMSO; black: 27.7 % DMSO. (B) Heme content in solution was quantified using the alkaline pyridine method. Data are expressed as mean \pm SEM, of three different experiments in A and B.

concentration was achieved, strongly indicating that reduced polarity promotes heme solubilization in acid conditions. Next, ability of DMSO to facilitate spontaneous beta-hematin crystallization was examined. Figure 25a shows that incubation of heme for 24 h in the presence of 27.7% DMSO strongly stimulated ($p < 0.0001$) the formation of an insoluble heme pigment *in vitro*. FTIR spectroscopy analyses of this material show the transmission peaks at 1211 cm^{-1} and 1664 cm^{-1} which designate the characteristic peaks of the iron-carboxylate bonds of beta-hematin (Figure 25b). Additionally, XRD analyses of this material (Figure 25c) demonstrated the presence of sharp Bragg diffraction peaks corresponding to a crystalline material, which is structurally and chemically identical to beta-hematin.(152) SEM analysis of product revealed a crystal morphologies that are very regular (Figure 25d), which markedly resemble those of synthetic beta-hematin(77). Curiously, the crystals produced by DMSO are extremely large compared to those found biologically(77, 153) and reaching up to $55\text{ }\mu\text{m}$ in length (Figure 25d). These results unambiguously identify the product of heme precipitation induced by DMSO as true beta-hematin.

DMSO accelerates spontaneous heme crystallization.

In order to further understand how DMSO stimulated heme crystallization, kinetics of spontaneous beta-hematin formation reactions were carried out in the presence of different DMSO concentrations. Figure 26a shows that beta-hematin formation occurs through a sigmoidal shape curve in such a way that higher DMSO concentrations caused the most powerful effects on driving heme crystallization. No appreciable product was observed in the control or in lower DMSO concentrations (4.6 % or 8.3 %). In addition, about 50 % of heme was converted into beta-hematin at 27.7 % DMSO 15 h after reaction start time. The Avrami equation is

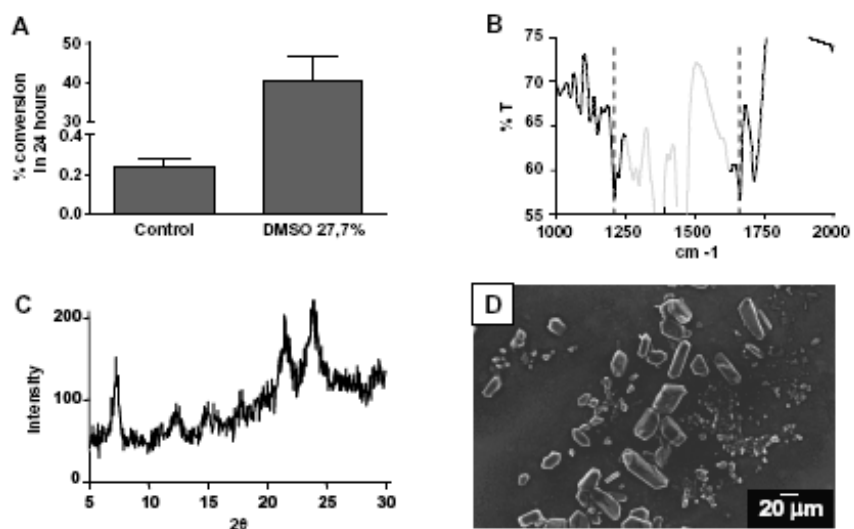


Figure 25. DMSO promotes spontaneous heme crystallization. (A) Spontaneous heme crystallization was performed from a 100 μM solution at different concentrations of DMSO in 0.5 M sodium acetate buffer pH 4.8, over 24 h at 28 °C. Data are expressed as mean ± SEM, of three different experiments. (B) The final reaction products were then characterized by FTIR spectroscopy. The large Nujol peaks in the region between 1320 cm⁻¹ and 1550 cm⁻¹ are depicted in light gray whereas the key beta-hematin peaks are shown at 1664 cm⁻¹ and 1210 cm⁻¹. (C) X-ray powder diffraction (XRD) was also used to confirm the identity of beta-hematin. (D) Scanning electron microscopy (SEM) was used to investigate the external morphology of the beta-hematin produced.

commonly used to model many different solid-state processes that involve nucleation and growth (91). In this equation, (see the methods section), the n values represent a function of the dimensionality of the growth process (assumed to be spherical, circular, or linear) and the type of nucleation (instantaneous or sporadic) (91). The exponent of Avrami is influenced by the type of nucleation, crystal morphology and the occurrence of secondary crystallization. Kinetics data from reactions with DMSO were fitted to the Avrami equation, and gives the r^2 values for the four possible values of the Avrami constant ($n = 1, 2, 3$ or 4) indicating that heme crystallization performed in these conditions involves nucleation and growth. Considering the reactions with 15.1 % DMSO, a reliable fit to kinetic equations was not possible. In the case of 27.7 % DMSO, the reaction has progressed significantly and the kinetics could be fitted to the Avrami equation. The fits of kinetic traces obtained for this condition was the following: $n = 1, 0.8393$; $n = 2, 0.9429$; $n = 3, 0.9682$ and $n = 4, 0.9863$. Therefore, the best fit obtained was for $n = 4$, which indicates that DMSO promotes beta-hematin formation by sporadic nucleation (nucleation occurs throughout the process) and spherical (or 3-dimensional)

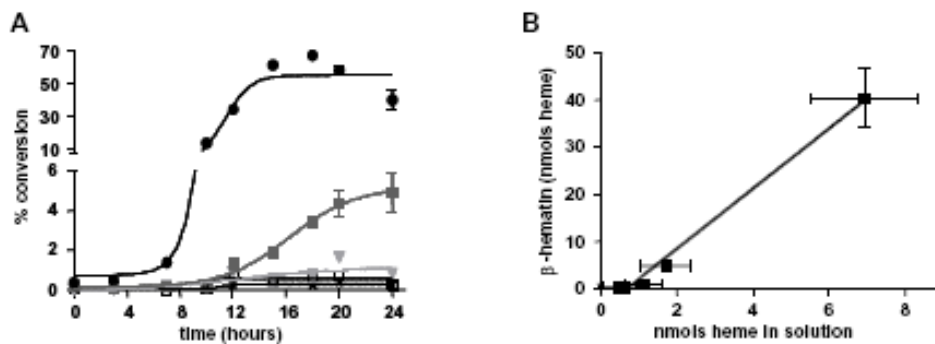


Figure 26. Increase in DMSO content promotes spontaneous heme solubilization and crystallization. (A) Kinetics of spontaneous heme crystallization were performed at different concentrations of DMSO with 100 mM over 24 h using 0.5 M sodium acetate buffer, pH 4.8 at 28 °C. Data are expressed as mean \pm SEM, of least three different experiments. Open square: control; open triangle: 4.6 % DMSO; inverted gray triangle: 8.3 % DMSO; dark gray square: 15.1 % DMSO; black circle 27.7 % DMSO. (B) Correlation of spontaneous beta-hematin formation at 24 h with heme solubilization at different DMSO concentrations ($r^2 = 0.8791$).

growth from these nucleation points. This pattern is consistent with reactions induced by acetate and benzoic acid as previously reported (90, 91). The rate constant (z) for this condition is $3.2 \pm 0.3 \times 10^{-5} \text{ h}^{-4}$ (or $9.3 \pm 0.9 \times 10^{-14} \text{ min}^{-4}$), proceeding in a very much slower way than with 4.5 M acetate, where $z = 2.3 \times 10^{-10} \text{ min}^{-4}$ at 37 °C (91) and even 0.050 M benzoic acid ($4.8 \times 10^{-12} \text{ min}^{-4}$ at the same temperature) (90). Therefore, these data strongly suggest that lowering the dielectric constant of water plays a significant role on the kinetic of heme crystallization. Just as a comparison, the rate constants obtained using total lipids extracted from regurgitates of adult *S. mansoni* females gave rate constants of $74 \pm 18 \text{ h}^{-2}$, but Avrami constant, $n = 2$. Finally, to establish a relationship between the initial heme solubilization and corresponding heme conversion, a linear regression analysis was applied to measured beta-hematin formation. Figure 26b shows that these two parameters are strongly correlated ($r^2 = 0.8791$; $p < 0.0001$).

Reduction in medium polarity by polyethers drives spontaneous heme crystallization.

To gain insight over the physico-chemical requirements on spontaneous beta-hematin formation, we performed heme crystallization reactions in the presence of different polyethers, such as polyethylene glycols (PEGs) of six different side chains (300, 3.350, 6.000, 8.000, 20.000 and 22.000), as well as the organic solvent acetonitrile, at 4.7 % (w/v) as final concentration. Figure 27a shows the FTIR spectra of pigments isolated after five days of reactions induced by PEG 300, 3.350, 6.000, 8.000 and 20.000. The characteristic beta-hematin transmittance peaks at 1210 cm^{-1} and 1664 cm^{-1} were seen in all PEGs-derived samples, with exception of PEG 300. Interestingly, this pattern was also observed in the XRD spectra of all these pigments, in which the 7.4° , 21.7° and 24.3° Bragg diffraction peaks characteristic of beta-hematin are present in all PEG-derived pigments, but not in PEG 300 samples (Figure 27b).

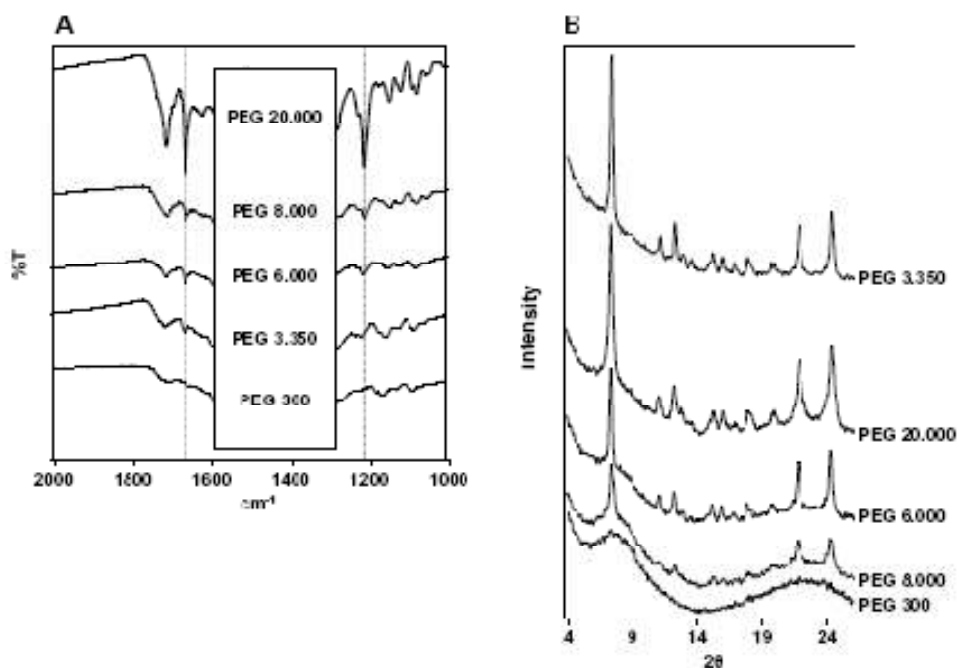


Figure 27. PEGs are able to induce beta-hematin formation under acid conditions. Spontaneous heme crystallization was performed in the presence of 4.7 % of different PEGs with 100 μ M, in 0.5 M sodium acetate buffer pH 4.8, over 5 days at 28 $^{\circ}$ C. Samples were centrifuged and the pellet washed in 0.1 M sodium bicarbonate buffer and 2.5 % SDS, pH 9.1, until the solution was almost clear. (A) Pellets were then characterized by FTIR spectroscopy. The large Nujol peaks in the region between 1300 cm^{-1} and 1600 cm^{-1} are obscured by the labels, but the key beta-hematin peaks are clearly seen at 1664 cm^{-1} and 1210 cm^{-1} . (B) X-ray powder diffraction (XRD) confirms the identity of beta-hematin.

Similar to DMSO, polyethers with molecular weight higher than 300 Daltons were able to trigger heme crystallization. Interestingly, morphological examination of dried product revealed crystals with a high frequency of brick-shaped crystalline structures in reactions performed in the presence of PEGs 3.350, 6.000, 8.000 and 20.000 and in a much lesser extent in PEG 300 (Figure 28). Although some of the dried heme reaction products of PEG 300 resemble superficially to crystals, the XRD pattern shown in Figure 27b unambiguously demonstrate that this material is essentially amorphous. The surface appearance of these crystalline structures are quite similar, if not identical, to those exhibited by natural hemozoin(77) and beta-hematin.(77, 91) Compared to the crystals produced by DMSO (Figure 25d), the size of crystals produced by PEGs was considerably smaller exhibiting the classical regular brick-shaped crystals and with lengths ranging between 2.5 μm (for PEG 3.350) and 3.91 μm (for PEG 6.000). The density of regular brick-shaped crystals also varied between 5.7 crystals/field (for PEG 20.000) and 27 crystals/field (for PEG 6.000). A kinetic investigation of PEG-induced beta-hematin formation was conducted over 7 days. Figure 29a show that in the absence of any additive (control), heme crystallization becomes evident only after five days of reaction. However, even after 7 days, the reaction has not proceeded far enough to allow a reliable fitting from kinetic equations. Also, four of the five PEGs investigated, were sufficient at promoting large quantities of beta-hematin. Interestingly, only polyethers with molecular weight higher than 300 Daltons were able to induce significant ($p < 0.05$) heme crystallization. As demonstrated in figures 27 and 28, incubation of heme with PEG 300 did not result in substantial beta-hematin formation, and in figure 29a it is

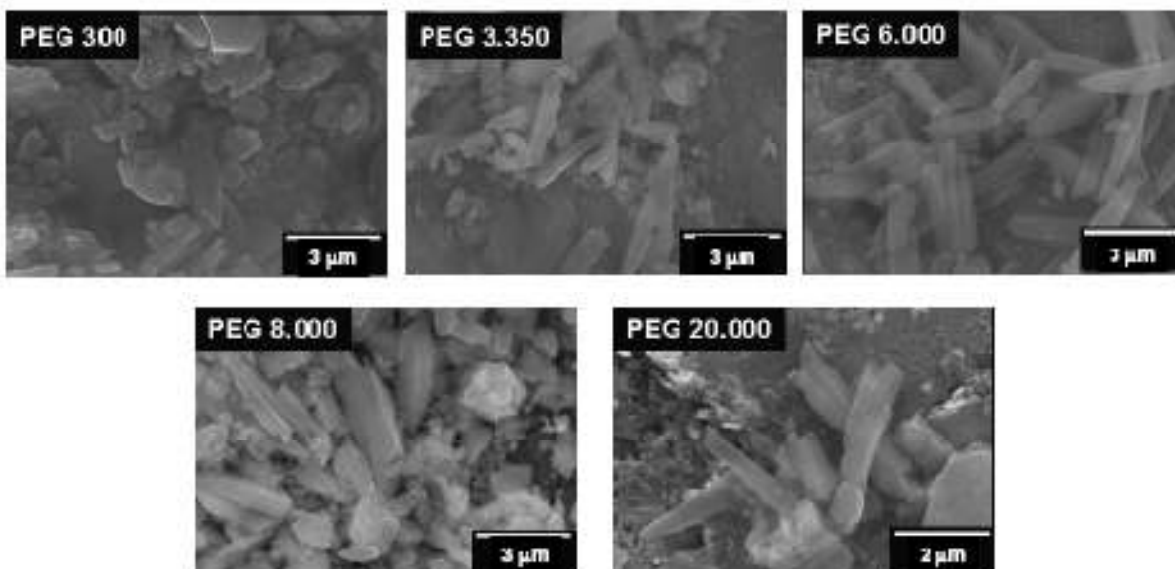


Figure 28. Scanning electron micrographs of beta-hematin induced by PEGs. Scanning electron microscopy (SEM) was used to investigate the external morphology of the β -hematin crystals produced by different PEGs. Well formed crystals are seen in the presence of PEGs 6.000, 8.000 and 20.000 which closely resemble hemozoin. Less regular crystals appear to be formed by PEG 3.350 and few if any are formed in the presence of PEG 300.

evident that this polyether specifically inhibited the process. The amount of crystals after 7 days was significantly lower ($p < 0.05$) than the control. In the case of PEG 3.350 the kinetics appear to conform to $n = 3$ or 4 , as is the case in acetate, benzoate and aqueous DMSO (with the same interpretation as indicated above for DMSO). Since there is almost no difference in the fit of $n = 4$ and 3 , it is likely that the former is consistent with the other systems. The rate constants for beta-hematin formation in the presence of PEGs were the following: PEG 3.350 = $3.7 \pm 0.8 \times 10^{-7}$; PEG 6.000 = $8 \pm 1 \times 10^{-4}$; PEG 8.000 = $4.7 \pm 0.7 \times 10^{-4}$; PEG 22.000 = $2.4 \pm 0.6 \times 10^{-4}$. It is important to note that direct comparison of the rate constants for reactions with different n values is not possible. The data show that kinetics in the presence of 4.7 % PEG 3.350 is considerably lower than in 27.7 % DMSO ($k = 3.7 \pm 0.8 \times 10^{-7} \text{ h}^{-4}$ vs. $3.2 \pm 0.3 \times 10^{-5} \text{ h}^{-4}$). The other PEGs tested promote beta-hematin formation, showing best fits with $n = 2$. This result can be interpreted in two ways, being either instantaneous nucleation (all nucleation sites present at the beginning of the process) and two-dimensional (disc-like) growth, or sporadic nucleation and needle-like growth. The latter would seem more likely in this case because it is difficult to imagine that PEGs would provide direct nucleation sites for epitaxial growth (which is thought to happen with lipids).(58) In fact, the brick-shaped crystal structure shown in figure 28 strengthens this concept. The reactions triggered by acetonitrile gives a best fit with $n = 2$, very similar to those found for three PEGs (please refer to part II of this chapter for more details on acetonitrile's effect on beta-hematin formation). An important observation to consider in the kinetic studies is related to the autocatalysis of beta-hematin formation, which was proposed to be one of the mechanisms of crystal production, based on the observation that purified beta-hematin could itself promote crystal growth as described in the literature.(48) However, in all

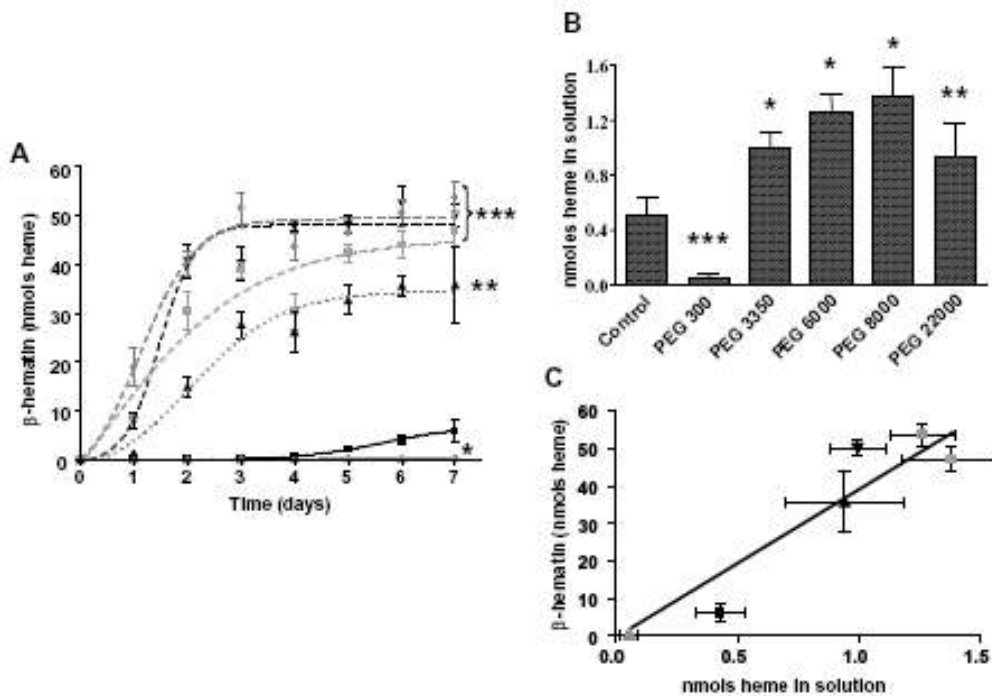


Figure 29. Prior heme solubilization by PEGs and organic solvents promote spontaneous heme crystallization. (A) Kinetics of spontaneous heme crystallization were performed in the presence of 4.7 % of different PEGs with heme 100 μ M over 7 days using 0.5 M sodium acetate buffer, pH 4.8 at 28 $^{\circ}$ C. Data are expressed as mean \pm SEM, of least three different experiments ($^* p < 0.05$, control vs. PEG 300; $^{**} p < 0.01$, control vs. PEG 22.000; $^{***} p < 0.0001$, control vs. PEG 3.350, PEG 6.000, PEG 8.000). Black square: control; gray triangle: PEG 300; inverted black triangle: PEG 3.350; gray circle: PEG 6.000; gray square: PEG 8.000; black triangle: PEG 22.000. (B) Heme content in solution was quantified by the alkaline pyridine method. Data are expressed as mean \pm SEM, of three different experiments in A and B, ($^* p < 0.05$, control vs. PEG 300, PEG 8.000, PEG 22.000). (C) Correlation of spontaneous beta-hematin formation after 7 days and heme solubilization in the presence of different PEGs and organic solvents ($r^2 = 0.8940$). Black square: control; gray triangle: PEG 300; inverted black triangle: PEG 3.350; gray circle: PEG 6.000; gray square: PEG 8.000; black triangle: PEG 22.000; inverted gray triangle: acetonitrile; black circle: DMSO.

systems tested in this work (Figures 26a and 29a) and in others (91, 149), the reactions become less efficient in later times, indicating that autocatalytic crystallization should play a negligible role in these conditions. DMSO solubility data indicate that the sufficiency of a promoter to facilitate heme crystallization rest heavily on its ability to promote heme solubility. To examine whether this holds true for PEGs, heme solubility within various PEG system was examined. Figure 29b shows that PEG 8.000 and 22.000 significantly ($p < 0.05$) increased the levels of soluble heme compared to control. Also, PEG 300 significantly ($p < 0.05$) reduced heme solubility in acidic conditions, re-enforcing the concept that previous solubilization is an important requirement to allow further heme crystallization *in vitro*. PEG 6.000 and 8.000 were the most potent compounds to promote heme solubilization. Figure 29c show a linear regression analysis indicating that, similarly to DMSO, beta-hematin formation and heme solubilization are strongly correlated ($r^2 = 0.8940$; $p < 0.0001$).

Previous evidence have demonstrated that beta-hematin crystals can absorb up to 14 % of its mass in water and the reversible crystal hydration affect the unit cells in such a way that rehydration results in a smaller cells (154). This suggests that water would participate on heme crystallization by providing the ordering of heme molecules, possibly between the layers of hemes. However, it is still unknown where water molecules are adsorbed, but these may include intercalation between the layers or adhesion to the crystallite surface (154). On the other hand, molecular dynamics simulations demonstrated that H₂O–heme molecules interact quite fast, producing the beta-hematin dimer by means of reciprocal iron-propionate linkage between heme molecules.(58) Then, conversion of this precursor to beta-hematin dimer would require only a ligand exchange process with bond formation from the propionate to iron and subsequent displacement of H₂O from the opposite face of each porphyrin. Since beta-hematin dimers

rapidly form hydrogen bonds between the protonated propionic acid groups, it seems unlikely that such interactions are expected to occur in water because of competitive hydrogen bonding.(58) Therefore, to gain insight over the role of water on heme crystallization, the medium osmolality in acetate buffers containing 1 % and 10 % DMSO were measured. In the absence of DMSO, osmolality was 86.6 mmol/kg whereas in 1 % and 10 % DMSO the values were 213,3 mmol/kg and 1448,6 mmol/kg, respectively. These values were used to estimate the water activity in these solutions as previously reported (148). In fact, the estimated water activity in 1 % DMSO was 0.9961 and 10 % DMSO was 0.9745 (data not shown). Finally, using reported water activity values of aqueous DMSO solutions at pH 7.4 (155), the degrees of heme solubility, the amount of beta-hematin produced was compared. Figure 30 shows that decrease in water activity is positively correlated with heme solubility ($r^2 = 0.9001$, $p < 0.05$) and beta-hematin formation ($r^2 = 0.8317$, $p < 0.05$).

Recently, Huy and colleagues (87) showed that promotion of heme conversion by alcohols is related with their degree of hydrophobicity and to their ability to solubilize heme, suggesting that dissociation of aggregated heme, and consequently the increase of heme monomers, are key physico-chemical factors in beta-hematin formation. In addition, alcohols can reduce the surface tension of a solution, thus lowering the energy barrier for creating a critical nuclei (87). Dorn and colleagues also observed that in acetate concentrations lower than 4.5 M, spontaneous beta-hematin formation was too slow to account for biological heme crystallization (138). This is probably because that acetate solubilizes hematin in acidic solution, and there is an indication that both the nucleation and linear growth rates of beta-hematin depend on acetate concentration (91). However, considering that acetate increase heme solubility, this would not reach the levels required to drive substantial beta-hematin formation since our kinetic studies

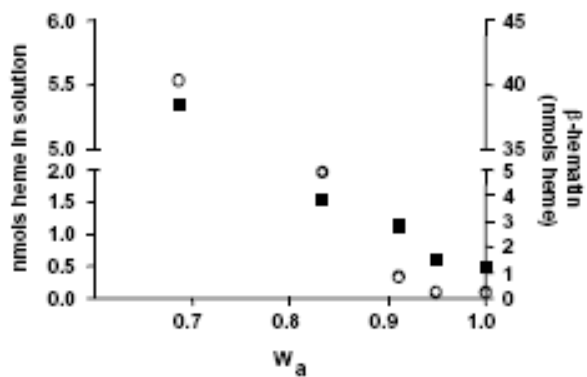


Figure 30. Heme solubility and beta-hematin produced in DMSO solution increase with reduced water activity. Values of heme in solution was obtained from Figure 24b and values of beta-hematin produced was obtained from Figure 24a. Water activity was calculated based on values obtained in Dupont and Pougeois, 1983 (155).

demonstrates spontaneous crystallization only after five days of reaction (Figures 26a and 29a). Only compounds that reduce the water content in a given concentration in the medium exhibited clear inducible effects on beta-hematin formation *in vitro*. In fact, Mössbauer analysis of *R. prolixus* midgut four days after blood meal provides compelling confirmation that at least 97 % of all iron-containing species present in that compartment are hemozoin (149), strengthening the concept that physiological levels of “free” soluble heme are very low. Conceivably, once hemoglobin is digested by proteases, and heme molecules released, these must reach a critical concentration in solution to allow its further crystallization that is provided by an amphiphilic structures such as lipid droplets in *S. mansoni* (156) and in *Plasmodium* (57) or by phospholipid membranes in *R. prolixus* (14, 82, 149) These biological and chemical hydrophilic-hydrophobic interfaces would act by allowing heme accumulation at the surface of these structures which would then favours the contact between heme molecules in an environment chemically suitable to drive the nucleation of unit cells of beta-hematin. This CB:DMSO system was successful at mediating the crystallization of Mn(III)PPIX (Appendix B).

Part II

Crystal Engineering: Solvent effect on beta-hematin morphology

A hallmark of hemozoin produced by *Schistosoma* and *Rhodnius* is the close association between crystals arranged into a larger roughly spherical structures composed of regularly shaped crystalline units.(77) At a magnified scale, these crystalline assemblies are composed of regular brick-shape crystals approximately 200 nm long. In *Plasmodium*, hemozoin morphologic shape varies between species. For example, *P. falciparum* hemozoin are closer in appearance to other mammalian *Plasmodium* species than in the avian *Plasmodium* species. Hemozoin from

mammalian *Plasmodium* species exhibit regular, brick-like features with smooth sides at right angles,(44) while crystals from *P. vivax* are larger and can be very thin.(44) It is possible that this discrepancy in hemozoin morphologies may be a result of *in vivo* crystallization parameters. To assess the morphological effects of crystallization parameters, various solvents were employed to evaluate beta-hematin crystallization. Changes in solvent composition is likely to change the driving force for crystallization due to altered Fe(III)PPIX solubility and may influence crystal shape.

Solvent promotion of Fe(III)PPIX solubility and spontaneous beta-hematin crystallization

Hemozoin is formed within the acidic aqueous (pH 4.8) environment of the digestive food vacuole of *P. falciparum* (20). However, Fe(III)PPIX is insoluble in water at pH 4.8. Its dissolution is believed to be the rate-limiting step for beta-hematin formation (90). Part I of this chapter has demonstrated the importance of Fe(III)PPIX solubility in beta-hematin formation. To assess the heme solubility properties in the presence of water miscible solvents (Table 1), heme was incubated in various mixtures of solvent and aqueous citrate buffer (CB) at pH 4.8. The addition of solvents (DMSO, DMF, THF, and MeCN) to buffer containing Fe(III)PPIX increased Fe(III)PPIX solubility. Figure 31b shows the UV-visible absorption spectra (400nm) of the supernatant collected after centrifugation of heme in the presence of various DMSO concentrations in CB. The introduction of DMSO increased the Soret absorption band of heme in a concentration-dependent manner. In particular, the introduction of a 10% DMSO to a solution

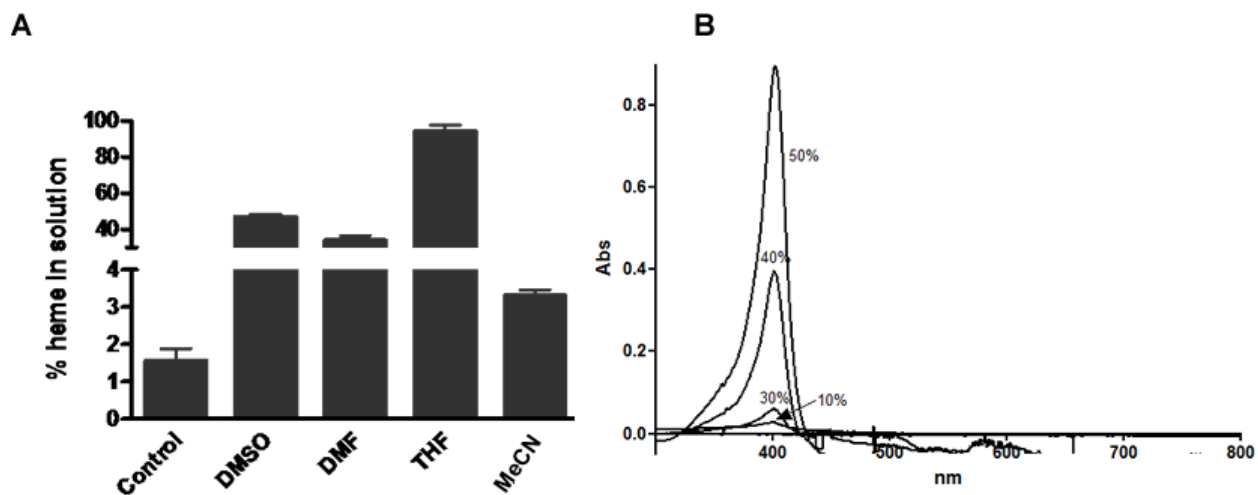


Figure 31. The addition of DMSO, DMF, THF, MeCN to a solution of aqueous Fe(III)PPIX increased heme solubility. This increased solubility was quantified using the alkaline pyridine assay(b)(147). Uv-visible spectra showing the solubility of heme in a CB:DMSO system as a function of DMSO concentration (b).

of Fe(III)PPIX in CB measured a Soret absorbance of 2.5×10^{-2} absorbance units (AU). However, when the volume of DMSO was increased to 50%, the Soret peak was increased by 35X to 8.9×10^{-2} AU. To quantify the degree of heme solubility, the percent of heme in solution was measured using the alkaline pyridine assay.(147) The addition of DMSO, DMF, THF or MeCN increased heme solubility to 46.5 ± 4.5 %, 33.7 ± 7.1 %, 93.8 ± 8.5 %, and 3.7 ± 0.3 %, respectively (Figure 31a). The percentage of soluble heme in the acidic CB, control sample, measured 1.5 ± 0.9 % heme was in solution (Figure 31b). Due to the biphasic solutions that are formed with CB mixed with DCM, CF or toluene, heme solubility in these systems could not be measure. Together, these data suggest that the introduction of water miscible solvents promoted heme solubility within the solvent:CB system.

Effects of solvent on beta-hematin crystal morphologies

The 12 hr incubation of Fe(III)PPIX in the water-solvent system at 37°C produced a water insoluble, brown product. These products were characterized morphologically by SEM, chemically by IR, and structurally by XRD (Figure 32). SEM analysis shows that, in general, crystals formed processed a needle-like structure with tapered ends. However, 3D growth in these crystals varied with mediating solvents. All samples exhibited prominent FTIR peaks at 1210 cm^{-1} and 1664 cm^{-1} , indicating significant formation of beta-hematin.(42) At the atomic level, the structures of crystals produced under the CB-solvent system exhibited the same XRD pattern as those of hemozoin which includes characteristic beta-hematin diffraction peaks at 7, 22, 24 2 θ .(41) Together, these results unequivocally confirmed the successful formation of beta-hematin.

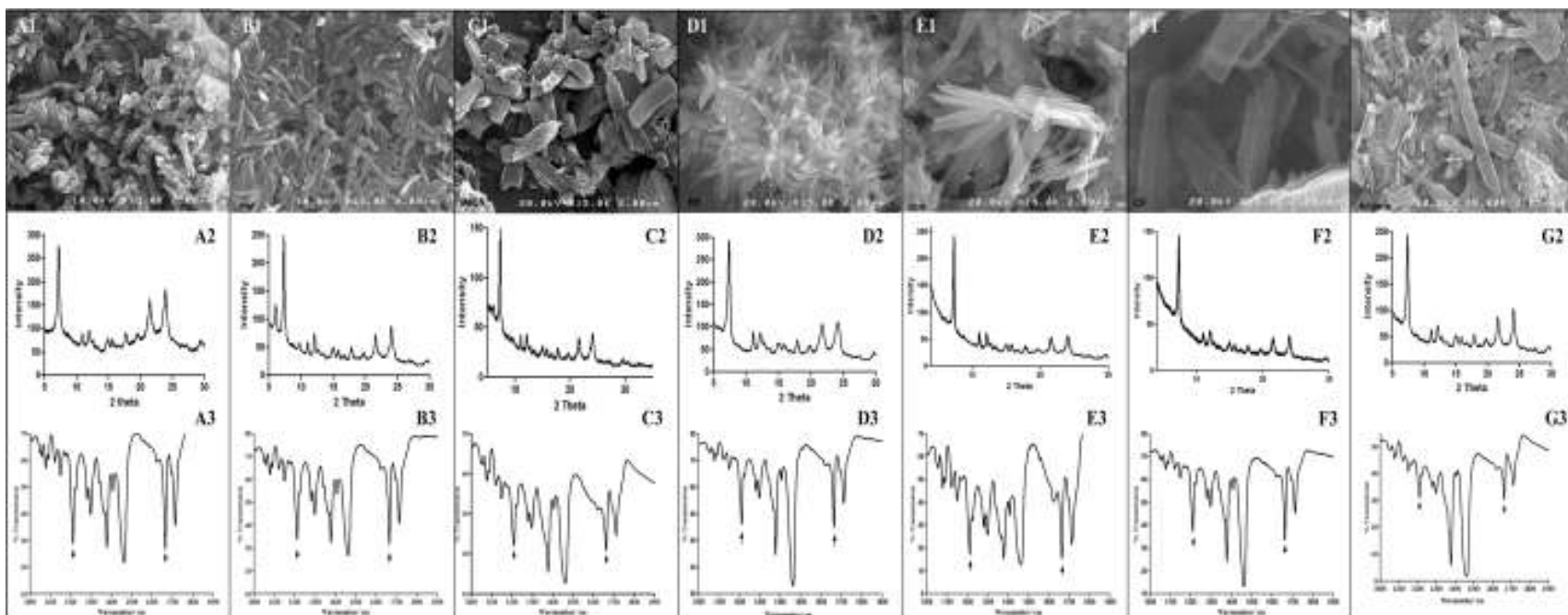


Figure 32. Product characterization of crystals formed under citrate buffer: solvent system. Crystals formed under DMSO (A), DMF (B), and MeCN (C) exhibited brick-like crystal habits (top row). Crystals formed under THF (D) and CF(E) displayed less thickness while crystal grown under CF(F) and toluene(G) are more smooth, plate-like. XRD (2, middle row) and FT-IR(3, bottom row) analysis unequivocally confirmed the presence of beta-hematin.

Unlike beta-hematin formed under other solvent systems,(157, 158) which produce homogenous, brick- like crystals resembling hemozoin from *P. falciparum*(44, 49), crystals produced in the current system exhibited morphologies that are dependent on solvent conditions. Crystals formed Under DMF, DMSO, and MeCN mediation exhibited morphologies that are regular in shape with the longest dimension being a few microns (Figure 32). These crystals have tapered ends that parallel hemozoin extracted from *P. falciparum* as reported by Sullivan *et al.* and Noland *et al*^{(49),(44)}. Much less size homogeneity was observed for crystals formed under CF and toluene. The tapering effects are still present but less frequent. Overall, these crystals appear more plate-like (Figure 32); however, crystals in the CB:toluene system appears to be much more thin than those from CB:CF system. Furthermore, SEM analysis of toluene mediated crystals showed structures that were nearly 6 times longer than those under mediation of DMF and DMSO. Beta-hematin from the CB:DCM and CB:THF system both exhibits some level of crystal thickness with a smooth surface. No apparent organization was observed with the exception of beta-hematin formed with THF. These crystals are organized into clusters with one end of each individual crystal sharing the same origin with other crystals in the cluster as if growth started at the center of the origin and elongated outward (Figure 31).

Interestingly, a relationship was observed between crystal morphologies and water miscibility of solvents. Solvents that are miscible in water (i.e. DMSO, DMF, and MeCN) produced crystals that resembled hemozoin from *P. falciparum* (Table 1). Hexane, a solvent that is immiscible with water was not able to mediate beta-hematin formation (Figure 31). As the solvent becomes less miscible (i.e. in decreasing order : DCM, CF, and toluene) the crystals become less uniform in sizes but smoother and more plate-like. In these solvent systems, 2D beta-hematin crystal growth is favored as a consequence of Fe(III)PPIX's reduced exposure to

water. It is speculated that within these less water miscible system, crystal formation takes place at the interface. These observations indicate that the presence of water is necessary to produce crystal with *P. falciparum*'s hemozoin morphologies.(157) Previous investigation of water behavior during hemozoin formation demonstrated that beta-hematin absorbs up to 14% of its mass in water and that reversible crystal hydration altered the unit cell of the crystal. Rehydration of these crystals produced crystals with a smaller unit cell(154) These observations suggest that water functions by ordering heme molecules; however, the molecular interaction of this phenomenon remains speculative. In fact, recent molecular dynamics simulations revealed that in the presence of water, two H₂O-Fe(III)PPIX molecules spontaneously interact to form the beta-hematin dimer(58). The conversion of this precursor to beta-hematin requires only a ligand exchange process with bond formation from the propionate O to Fe(III)and the displacement of H₂O from the opposite face of each porphyrin. However, in the presence of competing hydrogen bonds in water, this interaction is unlikely. Within the solvent environment- away from water- the interactions of dimers can occur more readily. Furthermore, the formation of beta-hematin under DMF, DMSO, and THF at various pH exhibited a bell shape curve dependence, with pK_{A1} at 2.5 ± 0.2 and pK_{A2} at 6.5 ± 0 (Figure 33). Maximum heme conversion occurred at a pH similar to that of the digestive food vacuole, pH 4.5 ± 0.1 . This observation can be explain by the protonation state of Fe(III)PPIX. At pH 4.8, the precursor dimer is likely to be a neutral (H₂O-Fe(III)PPIX)₂ species with only one propionic acid group on each porphyrin ionized and the other not.(150) As a matter of fact, this neutral species is critical for dimerization to occur because only in the protonation state can Fe(III)PPIX precursor assemble to nucleate crystallization.(58) The observed effect of pH on solvent mediated beta-hematin supports this notion.

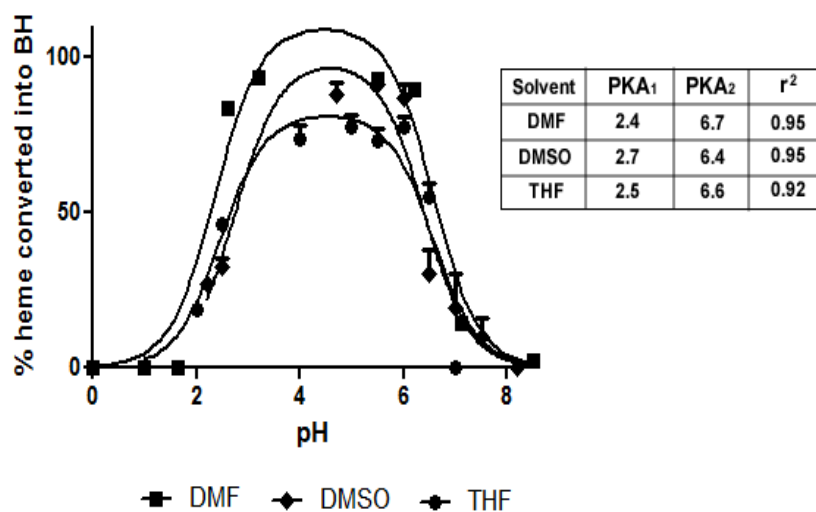


Figure 33. pH effects of beta-hematin formation under DMF, DMSO, and THF. Maximum heme conversion occurs at approximately pH 4, with pKA₁ at 2.5 ± 0.2 and pKA₂ at 6.5 ± 0. This acidic environment parallels that of the digestive food vacuole, the site of hemozoin formation, within *P. falciparum*. At pH 4.8, the Fe(III)PPIX molecule is likely to be a neutral (H₂O-Fe(III)PPIX)₂ with only one propionic acid group on each porphyrin ionized and the other not. Only at this protonation state can precursor Fe(III)PPIX assemble to initiate crystal nucleation.

Interestingly, the morphologies of beta-hematin formed under DMF mediation was not influenced by the temperature at which it was synthesized in DMF (Figure 34). Beta-hematin formed at 22, 37, 80 °C all exhibited crystals resembling hemozoin crystals form in *P. falciparum*, suggesting that the observed morphological differences are likely to be a chemically derived rather than thermodynamically driven. In fact, Orlov proposed that the effect in crystal habit is likely to occur if the dissolved substance reacts chemically with the solvent.(159) In aqueous DMSO, it is known that DMSO coordinates to Fe(III)PPIX.(160, 161) Resonance Raman data of Fe(III)PPIX solubilized in neat DMSO revealed that the complexes formed are six-coordinate high-spin (DMSO)₂Fe(III)Porphyrins.(162, 163) In light of Egan's modeling study,(58) this process may involve a Fe(III)PPIX preformed dimer. The presence of water completing for the axial Fe will prevent Fe(III)PPIX dimers from assembling into beta-hematin. DMSO, a stronger Lewis base than water, is likely to displace water as the axial ligand.(160) Ligand coordination likely occurs between the axial site of the Fe(III)PPIX iron and the sulfonyl oxygen.(164) It is speculated that nucleation begins when the propionic group of another precursor unit displaces the axial DMSO. As more monomeric units are assembled into the growing crystal, the rate of elongation decreases due to the lack of available monomers in solution. In the case of less miscible solvents, the crystals appear to be elongated and two dimensional. This suggests that within these systems, crystal growth occurs along the interface. In addition, coordination capabilities of the solvent will affect the rate of crystal formation. For example, in the toluene:CB system, coordination of the ligand most likely occurs through beta-stacking of the aromatic toluene with the p-system of the Fe(III)PPIX. Coordination could also occur between the p-group and the Fe, however sterics would only allow an π - π interaction

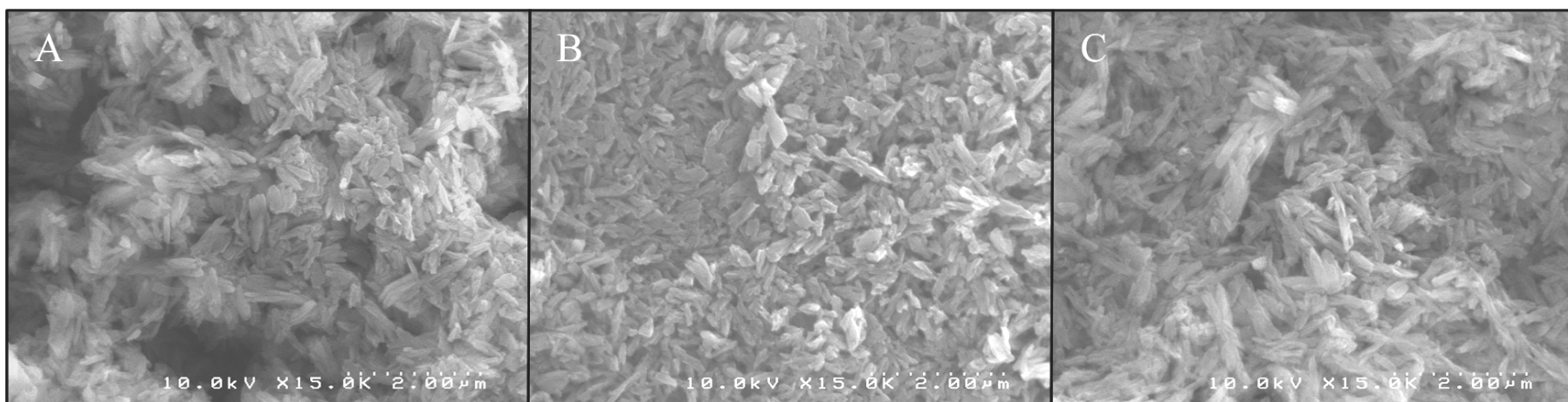


Figure 34. Effect of temperature on beta-hematin morphologies. Using DMF as the model organic solvent, beta-hematin was synthesized at 22°C (a), 37 °C (b), and 80°C (c). Crystals formed under these temperature exhibited no observed differences.

rather than a more favorable ada-6 (i.e. ferrocene). Chloroform and DCM both are aprotic polar solvents that can coordinate only through their chloro groups. At the interface, these ligands can displace water when in high concentrations, allowing for the formation of the dimers and subsequent assembly. Because of their limited solubility, growth occurs fastest along the interface, resulting in elongated thin crystals. The polarity of the solvent may lead to preferential adsorption at selected face of the solute by altering the surface roughness of the growing crystal (87, 165). When the degree of polarity for each solvent, given in terms of dielectric constant, is compared between experimental solvents, crystals produced using solvent with high dielectric constants (Table 1). (MeCN, DMF, DMSO) closely resembled *Plasmodium* hemozoin (166). A similar finding was reported by Huy *et al* (87) who employed alcohol to demonstrate a correlation between alcohols' degree of hydrophobicity and their ability to solubilized heme during beta-hematin formation, supporting the idea that heme solubility is a key physio-chemical factor in beta-hematin formation (157). In addition, the solvents effect on crystal habits, i.e., the ratio of growth rates of their various faces, is related to the changes of surface tension of the various faces (44). Huy *et al.* further demonstrated that reduction of surface tension facilitated heme conversion by lowering the nucleation energy barrier (87). Similar trends were measured for solvents used in this study. The measured surface tension of aqueous citrate buffer was 72.9 ± 0.3 mN/m (Table 2). Upon the addition of the solvent (1CB: 1 solvent), this value was dramatically reduced. The addition of DMSO or DMF to CB resulted in a surface tension reduction to 56.4 ± 2.4 mN/m and 46.3 ± 0.1 mN/m(Table 2). More drastic surface tension reduction of CB was observed for the addition of THF and MeCN, 29.2 ± 0.3 and 33.1 ± 0.1 mN/m, reducing the energy barrier for nucleation. Not surprisingly, in the current system, the percentage of beta-

Table 1. Properties of solvents (DMSO, DMF, MeCN, THF, DCM, CF, toluene) used to investigate beta-hematin morphologies.

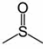
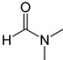
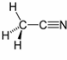

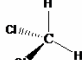
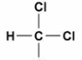
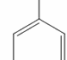

Properties	DMSO	DMF	MeCN	THF	DCM	CF	Toluene	Hexane
Solubility in Water	miscible	miscible	miscible	miscible	13 g/L	8 g/L	0.47 g/L	immiscible
Dielectric Constant	47	38	37	7.5	9.1	4.8	2.4	0
Structure								

Table 2. Measured surface tension of citrate buffer: solvent system

Crystallization System	Surface Tension (mN/m)
CB	72.8 ± 0.3
CB:DMF	46.3 ± 0.1
CB:DMSO	56.4 ± 2.4
CB:THF	29.2 ± 0.3
CB:MeCN	33.1 ± 0.1

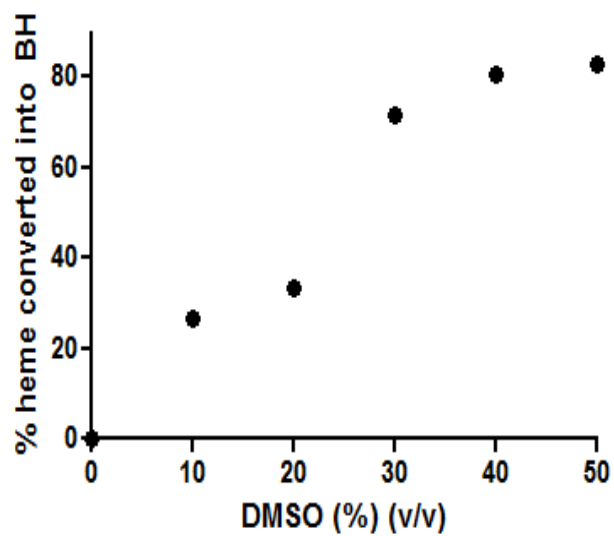


Figure 35. Effects of solvent concentration of beta-hematin formation. Increased concentration of DMSO in DMSO:CB system corresponded to increased percentage (%) of crystal formed within that system.

hematin formed is dependent on the percentage of solvent (Figure 35). Measurements of heme Soret absorption showed that increased volume of miscible solvent in the crystallization system increased heme solubility (Figure 31). In addition, at higher concentration of solvent, the surface tension may be reduced even further. A 10% DMSO (by volume) system resulted in about 28% conversion. However, when the percent of DMSO was increased to 50%, beta-hematin formation was increased to 82%. Thus, the morphological variation observed among the various solvent systems is a consequence of solvent parameters.

Effects of solvent on kinetics of beta-hematin formation

To further evaluate the role of solvents have in heme conversion, the kinetics of beta-hematin formation was measured under mediation of DMSO, DMF, THF, and MeCN. DMSO produced crystals with a half life ($t_{1/2}$) of 139.8 ± 2.2 min (Figure 36). Reactions under DMF and MeCN produced similar $t_{1/2}$ of 37.5 ± 2.1 and 30.9 ± 3.1 min, respectively. Beta-hematin formation under THF had the fastest rate of $t_{1/2}$ of 13.3 ± 3.0 min. These kinetic data strongly suggest that lowering of the dielectric constant (Table 1) of the solvent:CB system significantly increase the rate of beta-hematin. Of the four reaction conditions measured, DMSO has the highest dielectric constant of 47 also has the slowest rate of heme conversion. Likewise, THF, with a dielectric constant of 7.5, has shortest measured $t_{1/2}$. Results from these kinetic studies further support the role of low dielectric mediator for hemozoin formation. As discussed above, the presence of water is necessary for the synthesis of beta-hematin crystals exhibiting crystal morphologies mirrored to those in nature. Despite THF's miscibility in water, beta-hematin formed under its mediation does not have the same degree of thickness as crystals form under DMSO and DMF. However, THF dielectric constant is similar to that of CF, a less water

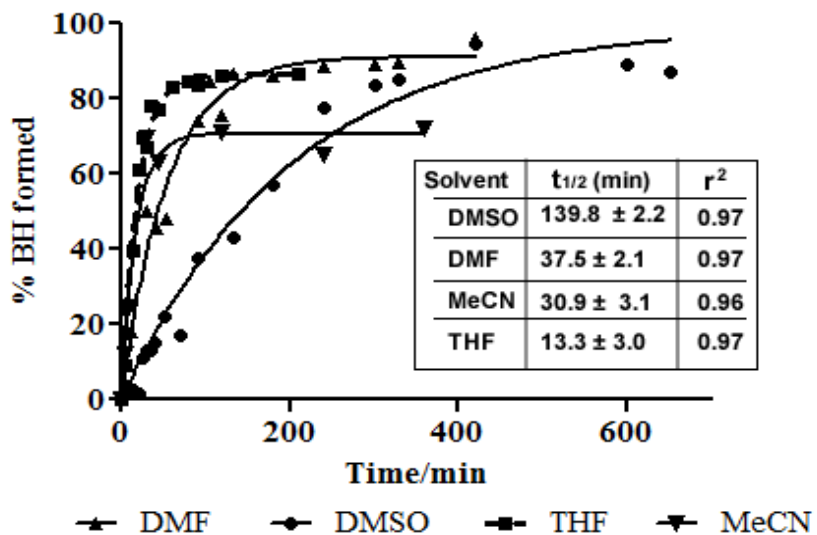


Figure 36. Kinetics of beta-hematin formation under solvent: CB system. Solvents with low dielectric constant, such as THF, produced hemozoin more rapid than solvents with higher dielectric constant, such a DMSO.

miscible solvent. Indeed, THF and CF crystals morphologies are practically identical, suggesting that the mediator polarity (i.e dielectric properties) plays an important role in deciding the morphology of the developing crystal. However, the introduction of soluble Fe(III)PPIX to water does not result in toluene, kinetic measurements of beta-hematin formation under these solvents were not successful.

Controllability of Beta-hematin crystal habits

To assess the controllability of beta-hematin morphologies, crystallization parameters containing mixed solvents were experimented. Successive additions of DMF (10%, 25%, 50%, 75%) were premixed with toluene and added to amorphous heme. SEM analysis revealed that alterations of solvent condition were successful in changing crystal morphologies (Figure 37). At 10% DMF, crystals exhibited morphologies that mirrored those of crystals formed in complete toluene (Figure 37a). These crystals are more plate-like and less regular than those at higher concentration (>50% DMF) (Figure 37c,d). At high concentration of DMF, crystal sizes are uniformly about 1 micron in length and exhibited more surface roughness. These results not only highlight the importance of synthesis design, but also hint at the crystallization parameters that controls hemozoin in nature. Beta-hematin synthesized with MeCN, DMF, and DMSO produced crystals that resemble *P. falciparum* hemozoin while THF, CF, and DCM produced more thin crystals similar to those in *P. vivax*. In the present study, the driving parameter that leads to these morphological differences appears to be related to the dielectric constant associated with the mediator. Likewise, the crystal morphology and organization discrepancy between the above mentioned organisms indicate that hemozoin formation in *S. mansoni* and *R. prolixus* differs

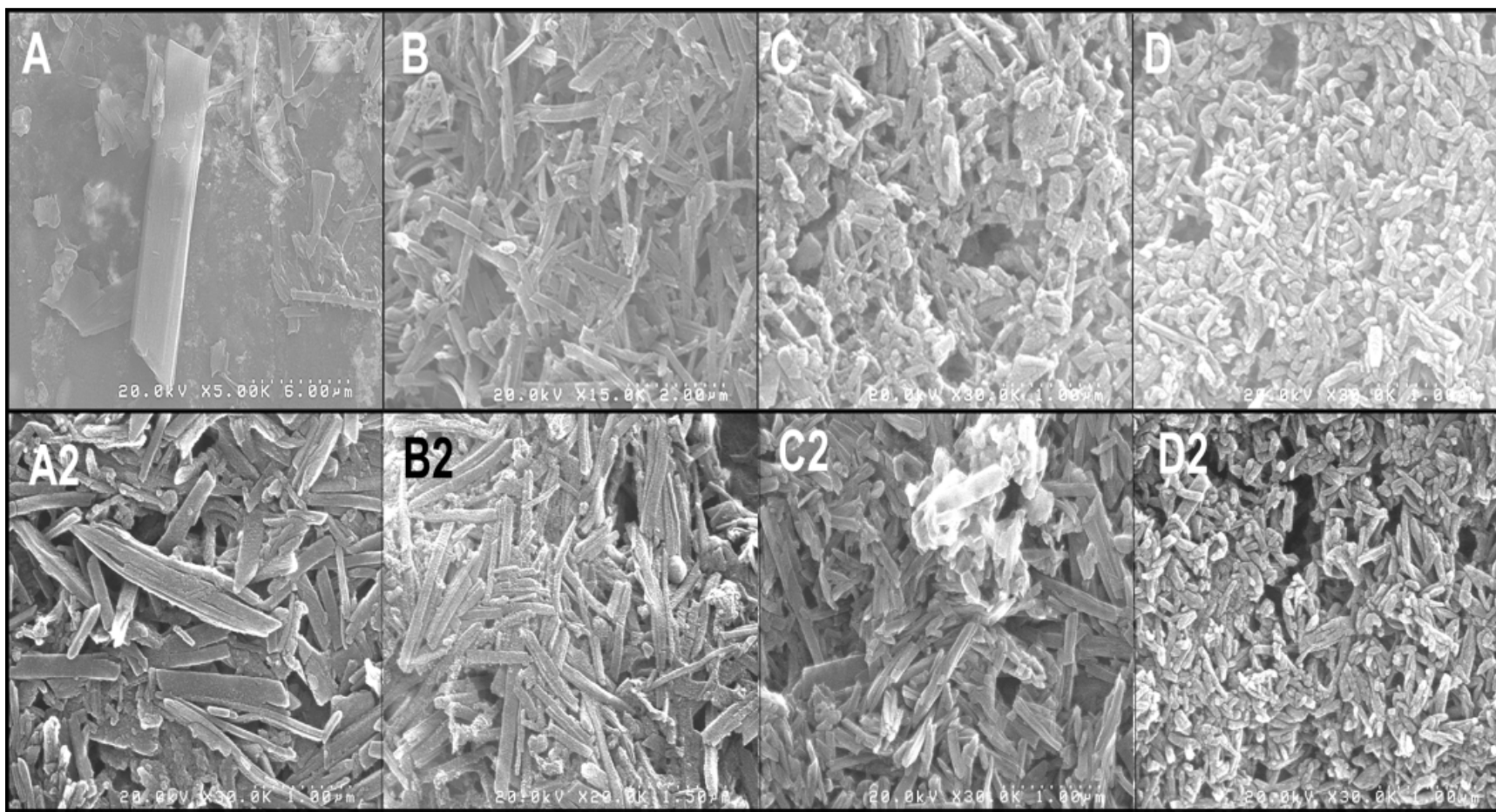


Figure 37. Formation of beta-hematin using mixed solvents. SEM images of crystals formed with 10% DMF and 90% toluene (a), 25% DMF and 75% toluene (b), 50% DMF and 50% toluene (c), and 75% DMF and 25% toluene (d). Crystal morphologies differed based on solvent condition.

from crystallization process that takes place in *P. falciparum*. For example, in *S. mansoni* and in *R. prolixus*, perimicrovillar membrane-derived vesicles present in the gut is proposed to provide attachment for free heme or a microenvironment in which heme remains soluble in an acidic milieu (77), a pre-requisite observed here for heme conversion. In addition, electron microscopy imaging of *P. falciparum*, *S. mansoni*, and *R. prolixus* provide irrefutable evidence that hemozoin formation occurs in close association with lipid bodies (57, 77, 156, 167). Specifically, hemozoin crystallization occurs at the interface of lipid bodies and water within the digestive food vacuole of the parasite (57, 58, 97). In fact, when Fe(III)PPIX is introduced to the interface of synthetic lipid bodies-water, beta-hematin is converted at a rate probably sufficient to account for heme toxicity within the parasite (97). In light of the current study, it is likely that these low dielectric organic mediators serve the same crystallization function as solvents do: lowering energy barrier for hemozoin formation. On that note, the triple localization of hemoglobin degradation, lipid bodies, and hemozoin within the acidic digestive food vacuole within *P. falciparum* may not be merely coincidental. And that, perhaps, lipid bodies may be produced by blood feeding organisms specifically for the purpose of heme detoxification.

Conclusion

The present study provides a systemic approach to beta-hematin crystal engineering. The introduction of heme to aqueous systems containing water miscible solvents (DMSO, DMF, THF, or MeCN) or PEG increased heme solubility and promoted spontaneous beta-hematin crystallization. The present study demonstrate that increase on the steady-state levels of soluble heme in acidic conditions, by reducing medium polarity, plays a critical role to determine

spontaneous heme crystallization *in vitro*. Morphological analysis of these crystals demonstrated brick-like structures, resembling hemozoin produced in *P. falciparum*. Less water miscible solvents (DCM, CF, or Toluene) formed beta-hematin exhibiting plate-like structures, similar to hemozoin found in *P. vivax*. Of significant, this study presents the first systemic approach for engineering of beta-hematin morphologies. Through the proper selection of solvents, the macroscopic crystal morphologies were successfully manipulated. These results demonstrate the success of controllability of beta-hematin morphology and illustrate the importance of beta-hematin synthesis approach. The heme conversion pathway is a target for anti-malarial drug design and hemozoin can serve as an indicator for diagnostic detection. In both examples synthetic hemozoin is often used in experimental analysis. Hence, special care must be taken to properly select solvent conditions during pre-formulation to help maintain batch-to-batch uniformity to ensure reproducibility of results. These data represent a significant advance for understanding the mechanisms involved in heme crystallization and may open new perspectives for the rational intervention of this process.

Section Acknowledgements

The work in this project would be incomplete without the contribution of Professor Kane Jennings, Peter Ciesielski, Brandon Booth from Vanderbilt Department of Chemical Engineering for providing instrumental help and access to surface tension instrument (Gamry Instruments). Special thanks to Josh Swartz for his contribution in SEM imaging, Rebecca Sandlin for fruitful mechanistic discussion, Leslie Hiatt and Jennifer Merritt for their proof reading assistants. In addition, the assistant of Mr. João V. de Oliveira Neto for his technical assistance is greatly appreciated.

Chapter V

PHAGE DISPLAY APPLICATION TO BETA-HEMATIN

The morphology of hemozoin (*P. falciparum*) and its synthetic counterpart, beta-hematin, consists of needle-like structure extended along the c-axis, exhibiting dominant {100} and {010} side faces, a less-developed {011} and minor {001} face.(41, 45) Modeling calculations of crystal face attachment energies, E_{att} , of beta-hematin formation revealed that crystal growth occurs the fastest at the {001} face as reflected by the highly negative attachment energy ($E_{att} = -101.5$ kcal/mol)(45). This face makes up the ends of the crystal and is speculated to be corrugated with O-H \cdots O hydrogen bond between the propionic acid groups of neighboring molecules along the $-a$ $+c$ direction. It is believed that traditional antimalarials such as chloroquine, amodiaquine, quinine, and mefloquine, all of which are protonated at the nonprimary exocyclic amine, and are thought to target hemozoin. These compounds then function by intercalating its quinoline rings between the aromatic groups of the beta-hematin molecules (Figure 3) and stereochemically capping onto the {001} surface of the crystal via (porphyrin) acid-amine (quinoline) salt bridge.(45) In addition, π - π interaction between drug compound and the crystal {010} further limits crystal extension. Molecular analysis of chloroquine and beta-hematin interactions shows that optimal beta-hematin inhibition occurs at a 2:1 chloroquine to heme interaction, suggesting that both axial face of the heme molecule is blocked from neighboring heme precursor by chloroquine.(137)

The highly structured, repetitive crystal habits of hemozoin are exploited by chloroquine to inhibit hemozoin formation.

Chloroquine binding to the highly structured, repetitive crystal habits of hemozoin inhibits the crystal extension.(49) Likewise, hemozoin can serve as a substrate for protein recognition, making it a good candidate for phage display application. Phage display technology utilizes the self-assembly nature of the viral capsid structures of M13 bacteriophage. In this approach, M13 viruses are reengineered to express select short peptides on their coat proteins. Generally, the peptide inserts are displayed on the virus PVIII or PIII coat protein. In the later case, the peptides are expressed on the outer surface of the phage, displaying five copies of the same peptide on its PIII coat protein. A phage library, comprising of $\sim 10^9$ peptide diversity, is then introduced to beta-hematin. This high diversity of peptides will increase the probability of finding or “panning” for a short sequence that specifically recognizes a select beta-hematin crystal face. Phage that binds tightly to the crystal can be amplified by exploiting its virus nature by allowing it to infect *E. coli*. In this example, the DNA sequences of select peptides are genetically fused to the PIII gene. Thus recovery of the phage DNA allows the amino acid sequence of the selected peptide to be deciphered.

Similar to chloroquine functionality, a peptide that selectively binds to the fastest growing face of beta-hematin may possess antimalarial properties. Likewise, peptides that specifically recognizes the {100} or {010} face may be a beta-hematin mediator by stabilizing the growing nuclei. In several phage display studies, researchers demonstrated that amino acids, such as aspartic acid, arginine, cysteine, glutamic acid, histidine, lysine, methionine, and tryptophan, selectively recognized certain inorganic substrates (168-170). These identified peptides can function as template for inorganic crystal growth and nucleation(170). Studies have revealed materials-specific peptides that have preferential bindings (171), promote precipitation of nanoparticles(172, 173), and control the morphologies of these particles (174, 175). For

example, it has been demonstrated that tyrosine plays an important role in the reduction of Au³⁺ to Au⁰ by a number of tyrosine-containing peptides, though most are limited to simple dipeptides and tripeptides. By controlling the sequence of these peptides, the researchers were successful at manipulating the sizes, morphology, and irregularity of the growing gold nanoparticles.(176-180) In addition, phage derived peptides were demonstrated to bind with high selectivity. For example, peptides panned against the {100} face of GaAs bound specifically to GaAs {100} but not to Si {100}. And in complementary fashion, peptides screened against the {100} Si surface showed poor binding to the {100} GaAs surface. Furthermore, panned peptides also promoted and control macroscale ordering of monomers. For example, the addition of poly(L-lysine) of greater than 100 residue inhibits spherical silica particle growth along the c-axis, forming hexagonal silica platelets (174).

In this study, phage display technology was employed to pan for a 7-monomer peptide that recognizes beta-hematin crystal face. The specific binding of peptide to the fastest growing face of beta-hematin may inhibit the growth of the crystal and thus, may express antimalarial properties. On the other hand, peptides that bind to dominant beta-hematin crystal face may exhibit crystal mediating properties.

Material and Methods

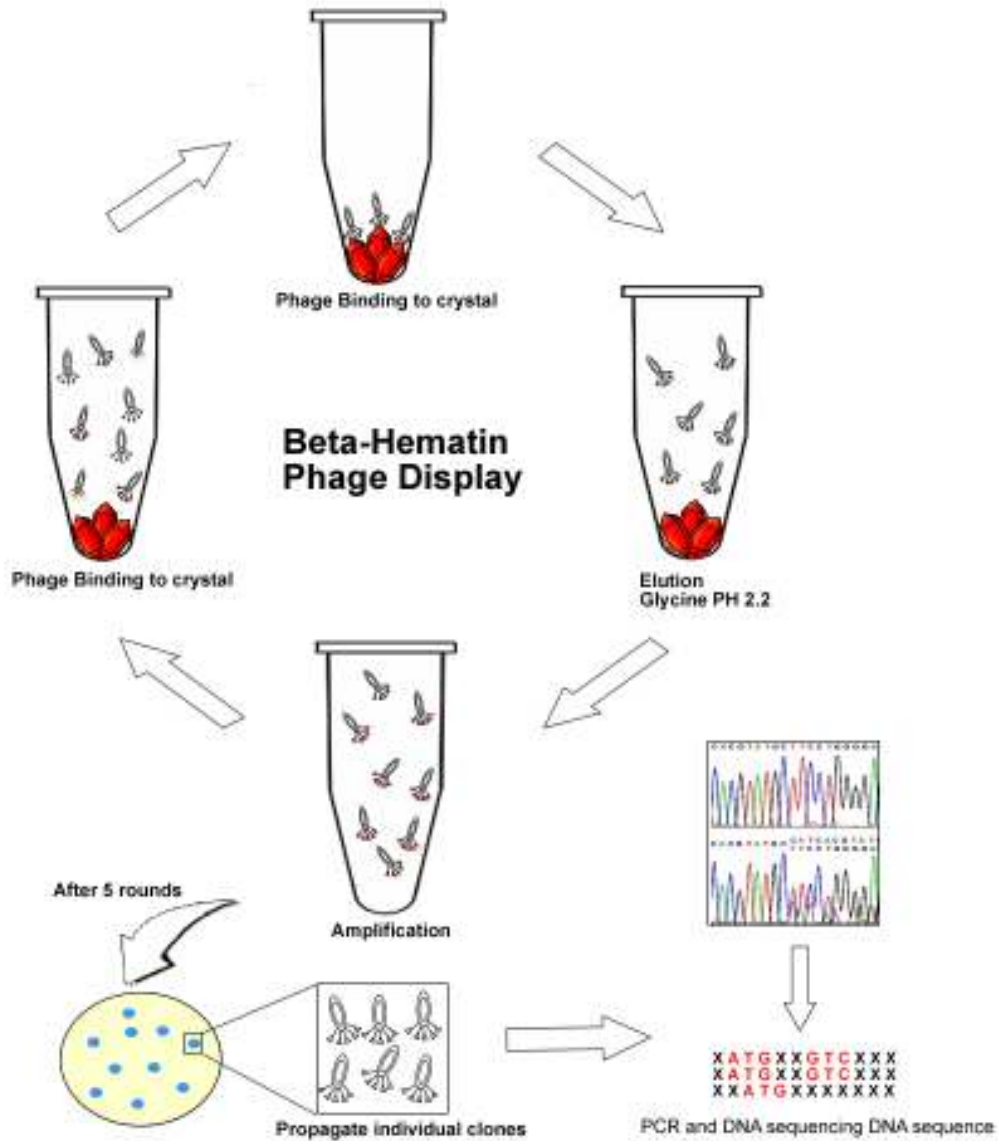
Beta-hematin synthesis and characterization

Beta-hematin was synthesized via dehydrohalogenation of hemin, as described by Bohle.(158) Briefly, in an inert atmosphere, hemin porcine (Sigma) is dissolved in a minimal amount of 2,6-lutidine. A 50:50 mixture of anhydrous methanol: dimethylsulfoxide (DMSO) was added and the reaction vessel was sealed and protected from moisture and ambient light for

approximately three months. After the incubation time, the product was filtered and the precipitate was washed exhaustively with methanol, 0.1M sodium bicarbonate (pH 9.1) and deionized water. The purified product was dried under vacuum at 150°C for 48 h and stored under desiccant. The cleaned product was characterized via infrared analysis (IR) and X-ray diffraction (XRD). The IR peaks of 1210 cm⁻¹ and 1664 cm⁻¹ and XRD peaks of 7, 22, 24 2theta confirmed the presence of beta-hematin.

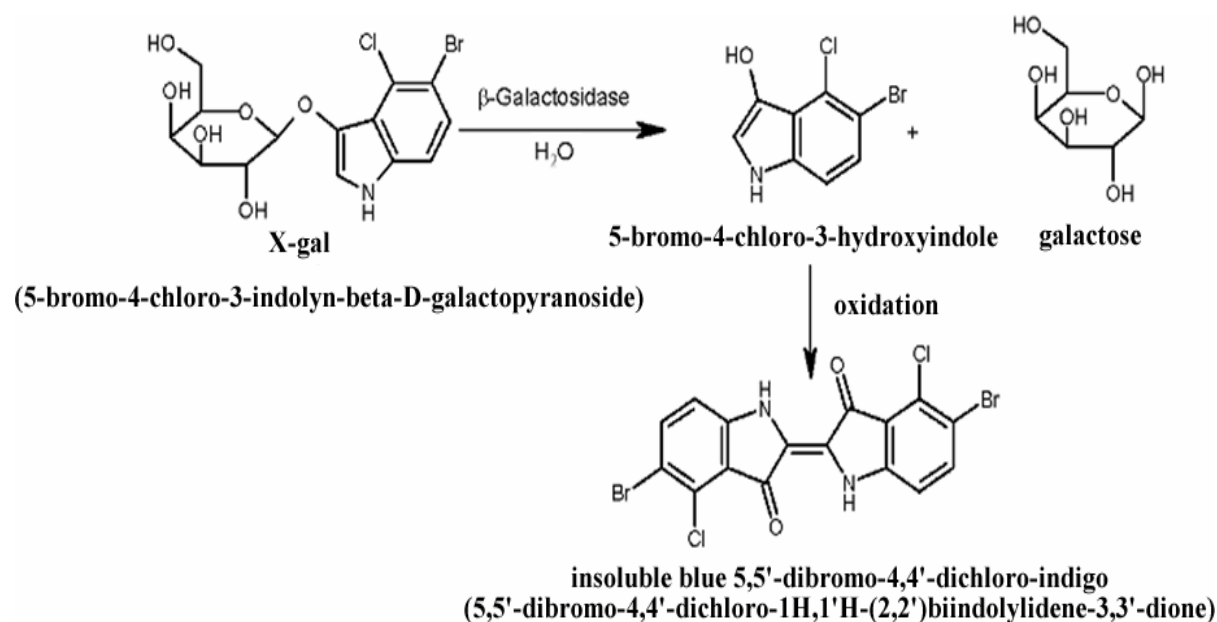
Beta-hematin Peptide panning

Beta-hematin recognizing peptides were panned using a 7-monomer, PIII phage display library obtained from Dr. Mario Geysen from the University of Virginia (Charlottesville, Virginia). Panning experimental procedures are displayed in Scheme 7. 100 µL of stock phage



Scheme 7. Beta-hematin phage display experimental procedure. A library of 7-mer phage was incubated with beta-hematin crystal. Nonspecific viruses are washed away, leaving behind phage that binds to the crystal. The beta-hematin-specific phages are amplified overnight in *E.coli*. The amplified viruses are then subjected to several additional rounds of panning to ensure the selection of beta-hematin specific phage. DNA of phages from the final round of panning are sequenced to determine the beta-hematin-specific peptide sequence.

library was introduced to 2 mg of beta-hematin in 400 μ L sterile PBS solution containing 0.5% Tween (PBST). The solution was incubated at 37 °C for 6 hours under gentle agitation. Beta-hematin was previously blocked (1 hr) with a PBS solution containing 0.5% Tween and 2% BSA(PBST-BSA). After incubation, the beta-hematin was washed several times using PBST to remove nonspecific phages. Bound phages were eluted from beta-hematin crystals by the addition of 150 μ L of an acidic glycine buffer (pH 2.2, 200 mM) for 15 minutes. The eluted phages were then transferred to a fresh tube and neutralized with a Tris buffer (pH 8.0, 2 mM). Eluted phages were amplified overnight via infection into *Escherichia coli* host cells to yield approximately 10^{11} copies of output phages. 100 μ L of amplified phages was used for the next round of panning. In total, five (5) rounds were completed with each round containing more phage expressing peptides that are more specific for beta-hematin (Appendix C). To select for individual phage, a diluted solution of panned phage are plated on Luria Broth plates containing *E. coli*, 5'-bromo-4-chloro-3-indolyl- β -D-galactoside (X-gal, Fischer Scientific, Fair Lawn, New Jersey) and isopropyl β -D-thiogalactoside (IPTG, Fisher Scientific, Fair Law, New Jersey) (Appendix D). Phage from the panning library produces a nonfunctional fragment of the β -galactosidase enzyme. In the presence of X-gal, this enzyme breaks X-gal into galactose and a byproduct, 5-bromo- α -chloro-3-hydroxyindole. The byproduct immediately oxidized into an insoluble compound that can be visualized as a blue pigment. *E.coli* used in this study produces another fragment of a nonfunctional β -galactosidase enzyme. The successful infection of *E.coli* by the phage with the 7mer insert will result in the assembly of a functional β -galactosidase enzyme. Selection for individual phage is then achieved by isolating individual blue colonies (Scheme 8).



Scheme 8. Selection and amplification of individual phage. A diluted solution of panned phage are plated on Luria Broth plates containing *E. coli*, 5'-bromo-4-chloro-3-indolyl-β-D-galactoside (X-gal) and isopropyl -v-D-thiogalactoside (IPTG). Phage from the panning library produce a nonfunctional fragment of the β-galactosidase enzyme. In the presence of X-gal, this enzyme breaks X-gal into galactose and a byproduct, 5-bromo-a-chloro-3-hydroxyindole. The byproduct immediately oxidized into an insoluble compound that can be visualized as a blue pigment. *E.coli* used in this study produces another fragment of a nonfunctional β-galactosidase enzyme. The successful infection of *E.coli* by the phage with the 7mer insert will result in the assembly of a functional β-galactosidase enzyme. Selection for individual phage is then achieved by isolating individual blue colonies.

Confirmation of panned phage recognition of beta-hematin crystals using Quartz crystal microbalance (QCM)

QCM techniques were used to confirm and quantify the recognition of panned virus to beta-hematin crystals. QCM is based on some materials exhibiting piezoelectric properties, the ability to generate an electric potential in response to applied mechanical stress. The quartz crystal naturally generates an electric field in response to an applied mechanical stress (181, 182). The QCM device operates by sending an electrical signal through a gold-plated quartz crystal, which generates a vibration at a specific frequency. The interaction of targeted molecules with the anchored probes will yield in a mass loading, detected by a decreased in frequency and increased in resistance by the QCM. The changes in frequency and resistance is used to calculate the mass loading or amount of antigen binding via the Saubery equation(1) (183). In this equation, Δf is the change in frequency (Hz), C_f is the sensitivity factor (various based on crystal properties), and Δm is the change in mass.

$$\Delta f = -C_f \Delta m \quad (1)$$

When used as a biosensor, probes (i.e. protein, antibodies, chemical) specific for the target molecule are immobilized on the surface of the gold-plated crystal. Generally, an aqueous sample which contains the target molecules is flow across the functionalized crystal surface. Recognition of the target molecule by the anchored probe is detected as a decreased in oscillating frequency. The sensitive piezoelectric property of the QCM allows for the detection of monolayer surface coverage by small molecules, a useful advantage for working within the scale of biological recognition. The QCM acoustic system has many practical advantages over the more mainstream methods, including portability, low limit of detection, lower expense, moderate

degree of training, and label-free quantization (181). In addition, signal transduction by the piezoelectric mechanism operates well in complex, often optically opaque solution media.

All experiments were performed using a Maxtek QCM system. Beta-hematin layer by layer assembly were produced on 5MHz QCM crystals, containing a gold deposit of 2,000Å^o in thickness. Crystals were initially cleaned three times using a piranha solution (3:1 solution of sulfuric acid and hydrogen peroxide) and dried under nitrogen. The assembly procedure for the beta-hematin layer by layer assembly production is illustrated in figure 38. Methods for producing poly (L-lysine) coated SAM were obtained from Frey and Corn (184). Briefly, cleaned crystals were immersed into a 1 mM ethanolic 11-mercaptopundecanoic acid (MUA) for at least 24 hr before being rinsed with ethanol and then soaked in water for 5 min. SAM crystals were rinsed with ethanol and dried under nitrogen prior to the addition of each new reagents. N-hydroxysulfosuccinimide (NHSS) ester was formed by exposing of the MUA SAM to an aqueous solution of 75 mM 1-ethyl-3-[3-(dimethylamino)propyl]carbodiimide hydrochloride (EDC) and 15 mM NHSS for 1 hour. These samples were then immersed in an aqueous solution of poly(L-lysine) (10mg/mL) for 1 hour. An aqueous solution of 100 mM beta-hematin was introduced to the SAM for an additional hour. Unbound beta-hematin was removed during ethanol washes. FTIR of beta-hematin functionalized QCM were obtained to confirmed presence of crystals. These beta-hematin layer by layer assembly were used for QCM measurements for determining the affinity of round five phages to BH crystals. Beta-hematin used in QCM studies was obtained from Bohle synthesis described above (158).

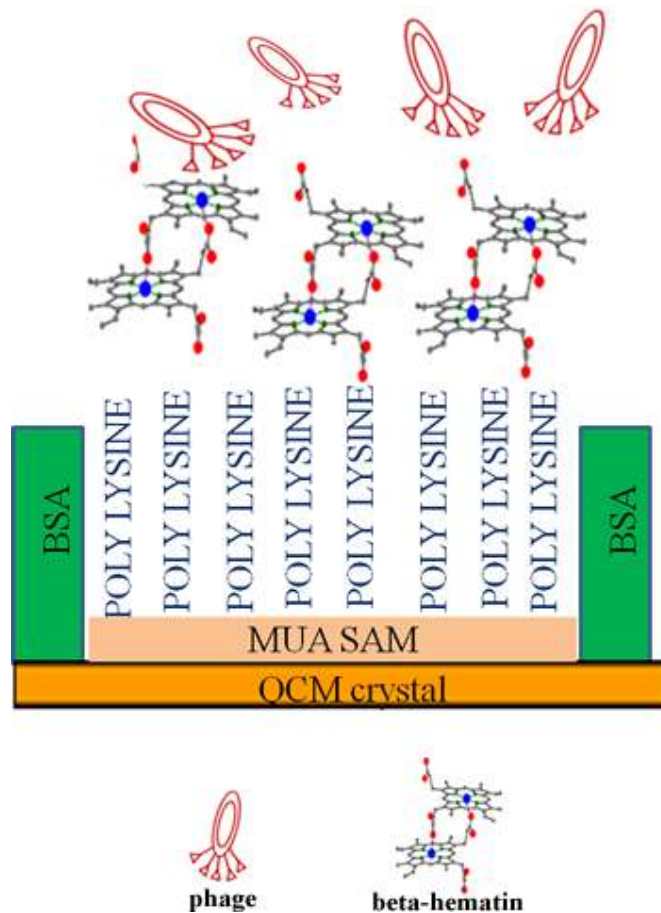


Figure 38. Beta-hematin self assembled monolayer. Beta-hematin crystals are functionalized on QCM crystals via a poly lysine layer. The assembly begins with the addition of a 11-mercaptoundecanoic acid (MUA) monolayer. This MUA layer was converted to the active intermediate N-hydroxysulfosuccinimide (NHSS) ester. The addition of poly lysine to this intermediate formed a layer of poly lysine that is covalently attached to the crystal surface via the MUA. The incubation of the poly lysine SAM to beta-hematin formed a beta-hematin layer by layer assembly.

QCM measurements

QCM measurements were performed using a Maxtek Quartz Crystal Microbalance system. 5MHz or 9MHz Matex crystals were used. All reagents were introduced to a tubing system (0.25 mm) at a flow rate of 35 μ L/min. The crystal containing functionalized beta-hematin was first stabilized in TBS buffer (~1 hr), followed by flushing the system with 1mg/mL BSA in TBS until binding reaches an equilibrium. Unbound BSA was washed from the experiment chamber with TBS. Next, the phage solution was introduced to the sample chamber until binding reaches equilibrium. Unbound phage was washed away with TBS. This was repeated for each phage sample. To ensure that phage was bounded to beta-hematin crystal and not exposed poly-lysine or BSA, phage solution was flowed over poly-lysine coated QCM chip.

DNA sequencing of phage from random peptide libraries

Individual phage were selected from blue and white screen process from round 5 samples. These individual viruses were isolated and amplified. Polymerase chain reaction (PCR) technique was used to amplified 7-mer peptide target region (on PIII coat protein). Purified PCR products were sequenced to determine the beta-hematin specific peptide sequence.

PCR technology review

PCR allows for the production of large quantities of a specific DNS from a complex DNA template of simple enzymatic reaction (185). Two oligonucleotide primers, short DNA fragment, are designed to be complementary to the ends of the targeted DNA sequence. These primers will mark the beginning and end of the targeted region. The DNA template containing the targeted amplification region is then introduced into a buffer solution with the primers, DNA polymerase, and deoxyribonucleotides. Immediate cooling then allowed the primers to anneal to

its complementary region on the single stranded template. The primers are positioned so that when each is extended by the action of a DNA polymerase, the newly synthesized strands will overlap the binding site of the opposite oligonucleotide (Figure 39). As the process of denaturation, annealing, and polymerase extension is continued the primers repeatedly bind to both the original DNA template and complementary sites in the newly synthesized strands and are extended to produce new copies of DNA. The end result is an exponential increase in the total number of DNA fragments that include the sequences between the PCR primers, which are finally represented at a theoretical abundance of 2^n , where n is the number of cycles.(186, 187)

In this study, the Qiagen RotorGeneQ 5-Plex thermocycler was used for DNA amplification. After PCR reaction is complete, electrophorese 3-5 μ l of the 50 μ l reaction on a 0.8-1.0% agarose gel, comparing PCR product using ssDNA template. The presence of an amplified fragment of approximately 240bp indicate the successful amplified of 7mer peptide insert. PCR products were purified using PCR purification kit from Promega. This step removes salts, unused primers, dNTPs, and enzyme for subsequent sequencing reactions.

The following PCR conditions were used:

1. *DNA template*: Pick plaques using a wide-bore 200 μ l pipette tip
2. *Primers*:

Forward	5'- TTTTTTTAGGAGATTTTCAACGTG -3'
Reverse	5'- CCCTCATAGTTAGCGTAACG -3'

PCR Reaction:

Amount	Reagent
5.0 μ l	5 μ l of lysate
4.0 μ l	Forward primer (5 μ M)
4.0 μ l	Reverse primer (5 μ M)
5.0 μ l	10X reaction buffer
1.0 μ l	dNTPs 10 mM each
30.5 μ l	H ₂ O
0.5 μ l	Polymerase

50.0 μ l

3. Thermocycle:

95°C	1.5 min	27-30 X
94°C	30 sec	
50°C	30 sec	
68 or 72°C	30 sec	
68 or 72°C	1 min	

Sequencing PCR samples

The forward and reverse primers, listed above, with the DNA template for PCR reaction was submitted for fluorescent dideoxy sequencing. Sequencing was performed by GenHunter Corporation (Nashville, TN). Sequencing results were identified by locating the forward primer, reverse primer, and signal sequence. The insert 7mer peptide is inserted following the PIII signal sequence.

M13KE DNA sequence:

Upstream DNA sequence

...GCTCAGCGACCGAATATATCGGTTATGCGTGGGCGATGGTTGTTGTCATTGTCGGCGCAACTATCGG
TATCAAGCTGTTAAGAAATTCACCTCGAAAGCAAGCTGATAAACCGATAACAATTA

pIII forward primer

AAGGCTCCTTTGGAGCCTTTTTTTTGGAGATTTTCAACGTGAAAAAATTATTATTCGCAA

gIII DNA sequence:

pIII SIGNAL SEQUENCE

V K K L L F A I P L V V P F Y S H S A

GTGAAAAAATTATTATTCGCAATTCCTTTAGTGGTACCTTTCTATTCTCACTCGGCCNNKNN

DNA insert

KNNKNNKNNKNNKNNKNNKNNKNNKGAAACTGTTGAAAGTTGTTTAGCAAAATCCCATACAG

-96 primer

AAAATTCATTTACTAACGTCTGAAAGACGACAAAACCTTAGATCGTTACGCTAACTATGAG

GGCTGTCTGTGGAATGCTACAGGCGTTGTAGTTTGTACTGGTGACGAACTCAGTGTTACGG
TACATGGGTTCCCTATTGGGCTTGCTATCCCTGAAAATGAGGGTGGTGGCTCTGAGGGTGGCG

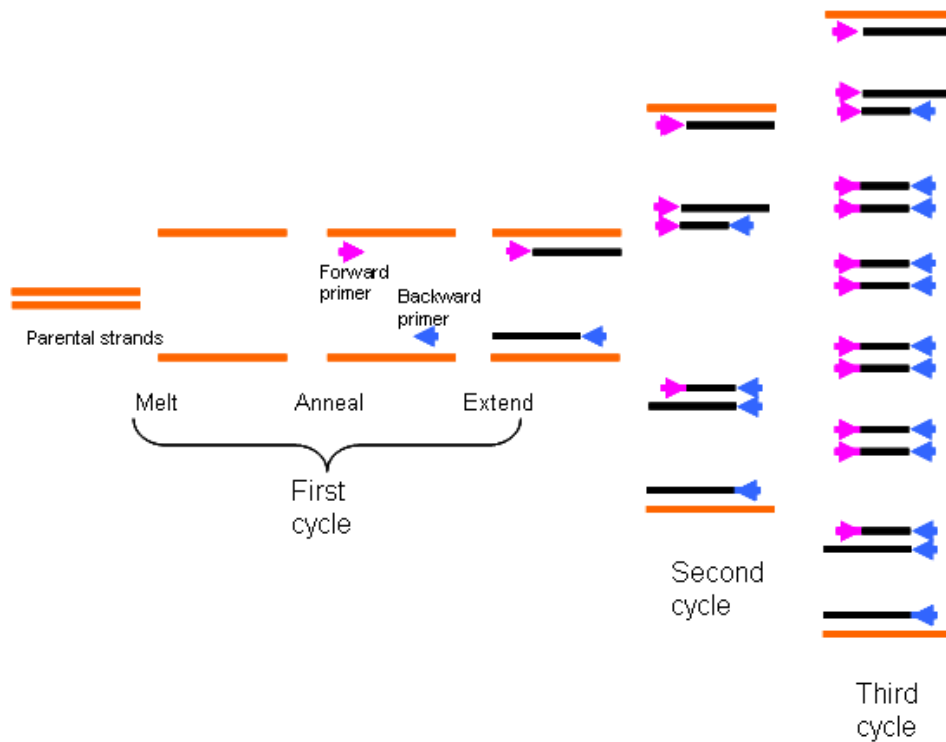


Figure 39. Polymerase chain reaction (PCR) is a method to amplify select DNA sequence using cycles of repeated heating and cooling. In the first step, the sample is heated to denature the double stranded DNA template. Immediate cooling allows for the primers to anneal and mark the region to be amplified. The temperature is then heated again to allow DNA polymerase, an enzyme, to extend the primer. As PCR progresses, the DNA generated is itself used as a template for replication, setting in motion a chain reaction in which the DNA template is exponentially amplified.(186)

Synthesis of protein mimics

All peptides were synthesized using standard Fmoc solid phase synthesis methods using an Apex 396 peptide synthesizer (Aapptec). All peptides were synthesized using a Rink amide resin. The N-terminus of each peptide was acylated using DCM:acetic anhydride (1:1). Cleavage was performed by treating the functionalized resins with Reagent R (90:5:3:2 TFA:Thioanisole:Anisole:EDT) and precipitating the peptides in cold ether. Purification was performed using a reverse-phase HPLC (Waters Prep LC 4000) with a Waters 2487 dual wavelength detector and C18 column.

Identification of peptide functionality

Stock solution of Fe(III)PPIX was made by dissolving 16.39 mg hemin chloride in 1 mL Dimethyl sulfoxide (DMSO). This sample was sonicated, vortexed and filtered through a 0.2 μm acetate syringe filter (Fisher Scientific). Stock solution of peptide was made in aqueous acetate buffer (2 M, pH 4.8) or citric buffer (50 mM, pH 4.8) at 1mM concentration. To determine the functionality of identified peptides, the detergent assay optimized in the Wright Lab by Dr. Melissa Carter and Rebecca Sandlin was applied to the peptides. 177.8 μL of stock Fe(III)PPIX solution was added to 20 mL of buffer solution and immediately used. 20 μL of stock peptide, 90 μL Fe(III)PPIX solution, 90 μL diH₂O was added to 96 well plates. Reactions containing no peptides and reactions using Nonidet P-40 (NP40) served as controls. NP-40 has been previously demonstrated in the Wright research group to be very successful for the mediation beta-hematin formation. In NP40 reaction, 84.9 μL of manufactured NP40 solution (ThermoFisher, 10% solution) was added to 45 mL diH₂O. 18.4 μL of this solution was added to 90 μL of Fe(III)PPIX, and 916 μL diH₂O to make up the control reaction. The reaction was

incubated at 37 °C for 12 hr. In addition, three scrambled, random 7 amino acid peptides were generated to serve as control reactions. To ensure reproducibility, each reaction was performed in triplicates. These reactions are repeated in citric buffer. To determine if peptides had beta-hematin inhibiting properties, 30.5 μM of chloroquine was added to 100 μM peptide and 100 μM Fe(III)PPIX in a 200 μL reaction volume. As control, NP40, Fe(III)PPIX and CQ was reacted. All reactions were performed at 37 °C for 12 hr in triplicate.

Quantification of Beta-hematin formation

To quantify percentage of beta-hematin form, pyridine assay reported by Egan *et al.* was used (79, 97). Briefly, the introduction of an aqueous pyridine (5%, v/v, pH 7.5) to the reaction sample results in a low-spin pyridine-hematin complex. This complex does not form with beta-hematin. Its absorbance obeys Beer's law, making it useful for quantitating hematin concentration in hematin/beta-hematin mixtures.(79) The reaction was quenched with the addition of 40 μL of an aqueous solution containing 30% pyridine, 10% HEPES buffer (2.0 M, pH 7.5), and 40% acetone (v/v).

The percentage of unconverted Fe(III)PPIX was determined by performing colorimetric measurements of the samples. 50 μL of the sample and 50 μL of water were transferred to a 96 well plate with read at 405nm on a Biotek Synergy HT multi-mode microplate reader. The percentage of beta-hematin conversion was calculated as previously described(79) and analyzed using GraphPad Prism 4.0 to obtain the half-life of each peptide.

Peptide orientations

To determine orientations of peptides in aqueous solution, dynamic light scattering (DLS) measurements were performed on 1 μ M and 10 μ M peptide buffer solution. A 1M solution of acetate buffer adjusted to pH 4.8 was used. Measurements were performed in triplicates using the Malvern Zetasizer instrument.

Results and Discussion

Selection of beta-hematin specific phage

Phage display techniques were successfully applied to beta-hematin crystal to select for beta-hematin specific peptide sequences. The first round of panning used a phage library that contained approximately 10^9 peptide diversity. After five rounds of panning, the large phage library was reduced to approximately 200 potential viruses that demonstrated recognition of the beta-hematin crystal (Figure 40). Note, this does not translate to 200 different peptides. In fact, this 200 phage may be the duplicates of only a few distinct viruses. QCM analysis was used to confirm the specificity of these isolated phages. Beta-hematin crystals used for panning requires a three month synthesis, thus growing crystals directly onto the QCM crystal was not an option. Instead, beta-hematin were functionalized onto QCM crystals via a layer by layer assembly. The assembly of beta-hematin QCM chips was monitored real-time via QCM (Figure 41). The reaction began with a NHSS ester SAM pre-formed overnight on a QCM crystal. The flow of poly lysine to the SAM surface resulted in the binding of approximately 60 ng poly lysine (Figure 41a). Following a buffer wash, a solution of beta-hematin was introduced to the poly lysine SAM, resulting in a 25ng coating to the surface. Excess crystals were removed via another buffer wash. Maxtek QCM crystals used in this study have an estimated $3.42 \times 10^7 \mu\text{m}^2$ available surface for surface assembly. The largest face of beta-hematin formed under Bohle

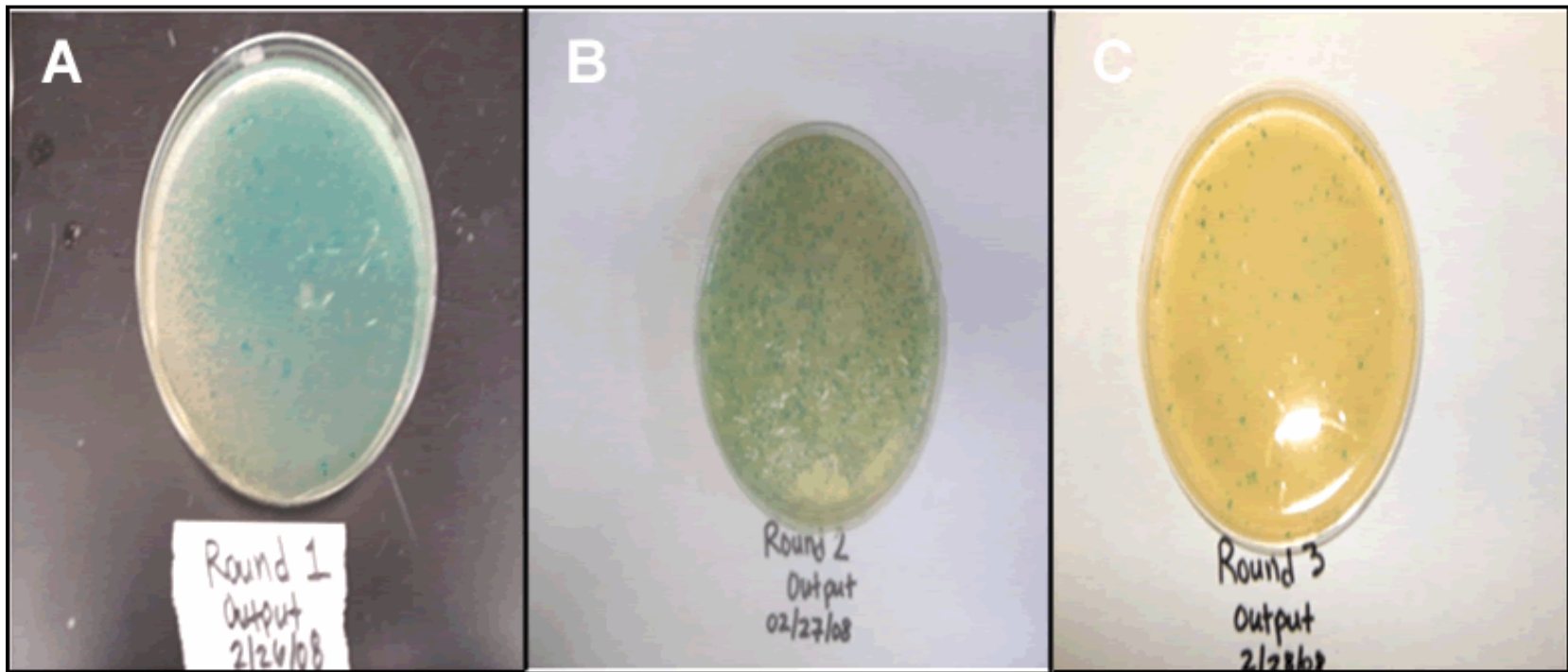


Figure 40. Increased panning rounds reduces non-specific phage. Each green spot corresponds to one phage. Increased panning cycle reduced the number of unspecific phage particle. A) round one , b) round two, and c) round three.

synthesis(158) are approximately $5\mu \times 1\mu \times 0.5\mu\text{m}$. Theoretical values were calculated using beta-hematin density values($1.45\text{g}/\text{cm}^3$) estimated by Pagola.(41) If all crystals were to interact with the poly-lysine surface through its largest crystal face, {100}, a maximum surface coverage (100% binding efficiency) would equate to a mass loading of 0.25mg or 6.8×10^6 crystal. However, if all deposited crystals were aligned along its end, a maximum mass loading of 2.478mg or 6.8×10^7 crystals is expected. The experimental mass loading of 25 ng (figure 41) is estimated to be a less than 0.1% surface coverage. Despite this low coverage rate, reflective IR measurement of the crystal surface confirmed the presence of peaks at 1210 cm^{-1} and 1664 cm^{-1} , confirming the attachment of beta-hematin to the poly-lysine surface (Figure 41b).

To validate the success of the phage panning series, an isolated phage particle from round 5 was amplified and QCM was used to quantify its beta-hematin recognition (Figure 42). The flow of aqueous poly-lysine over MUA functionalized QCM crystal resulted in approximately 206 ng binding, suggesting strong anchoring of poly-lysine to MUA surface. Once poly-lysine loading leveled off, TBS buffer was used to wash off excess substrate. Approximately 34 ng of beta-hematin crystals bound to the poly-lysine surface. The introduction the solution of round five phage produced approximately 20 ng mass loading, confirming the ability of panned phage to recognize beta-hematin crystal surface. Based on a $930\text{nm} \times 7\text{nm}$ M13 phage dimensions (188, 189), a theoretical maximum loading of 0.35mg was calculated for uniform attachment of phage virus laying on its side (not ends). A mass loading of 20 ng is about 0.05% binding efficiency. This was not unexpected given the low efficiency of beta-hematin binding onto the poly-lysine surface. To ensure that the phage used in QCM quantification was indeed binding with beta-hematin crystals and not exposed poly-lysine or BSA layer, a control was performed (Figure 43). Round 5 phage was introduced to the surface of BSA blocked poly-lysine layer.

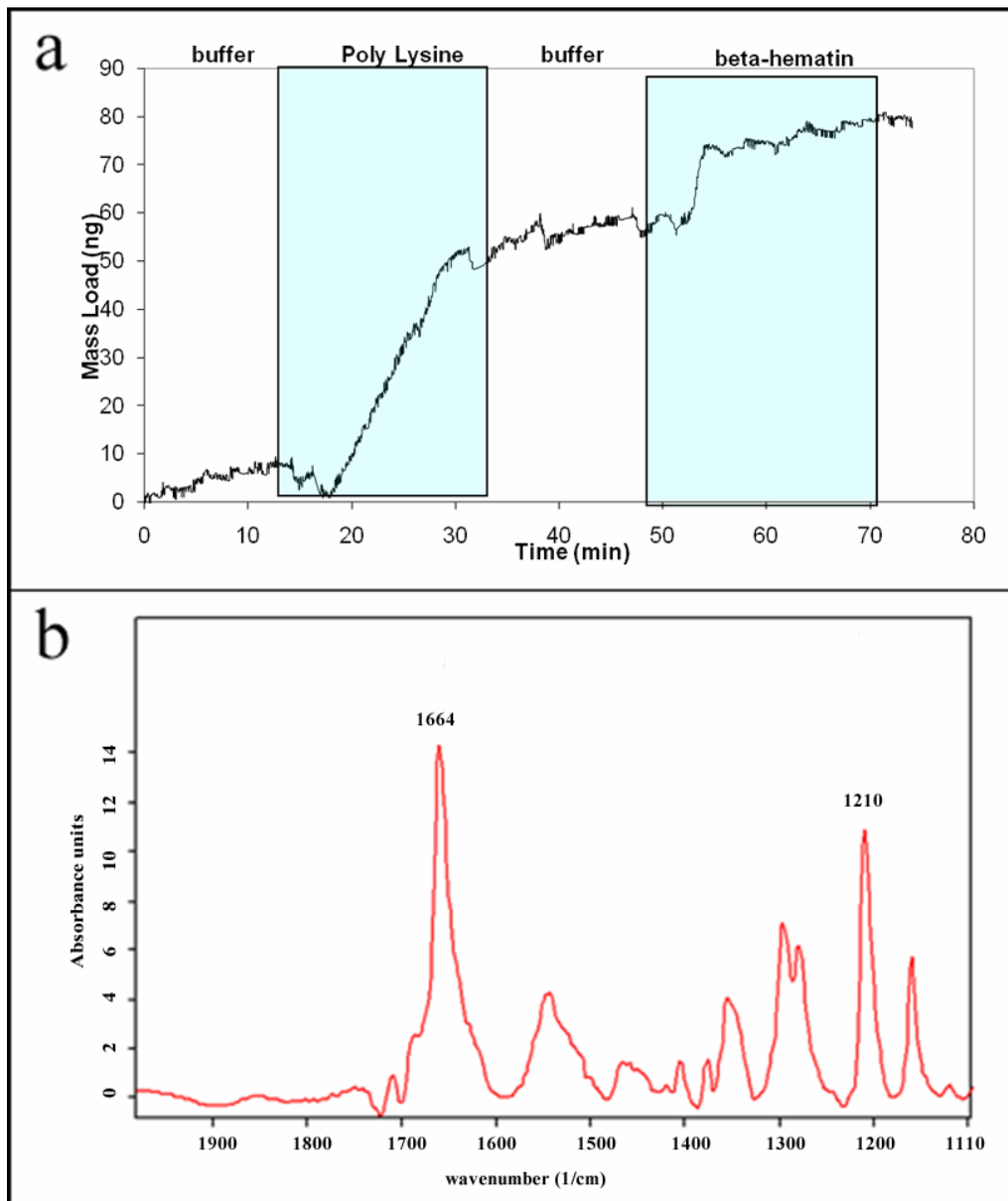


Figure 41. Functionalization of beta-hematin crystal onto QCM chip. Approximately 60 ng of poly-lysine covalently attached to the MUA SAM. Introduction of beta-hematin to poly-lysine surface produced a mass loading of approximately 25ng mass loading (a). The successful binding of beta-hematin to the poly-lysine surface was confirmed by the presence of FTIR peaks at 1664 cm^{-1} and 1210 cm^{-1} .

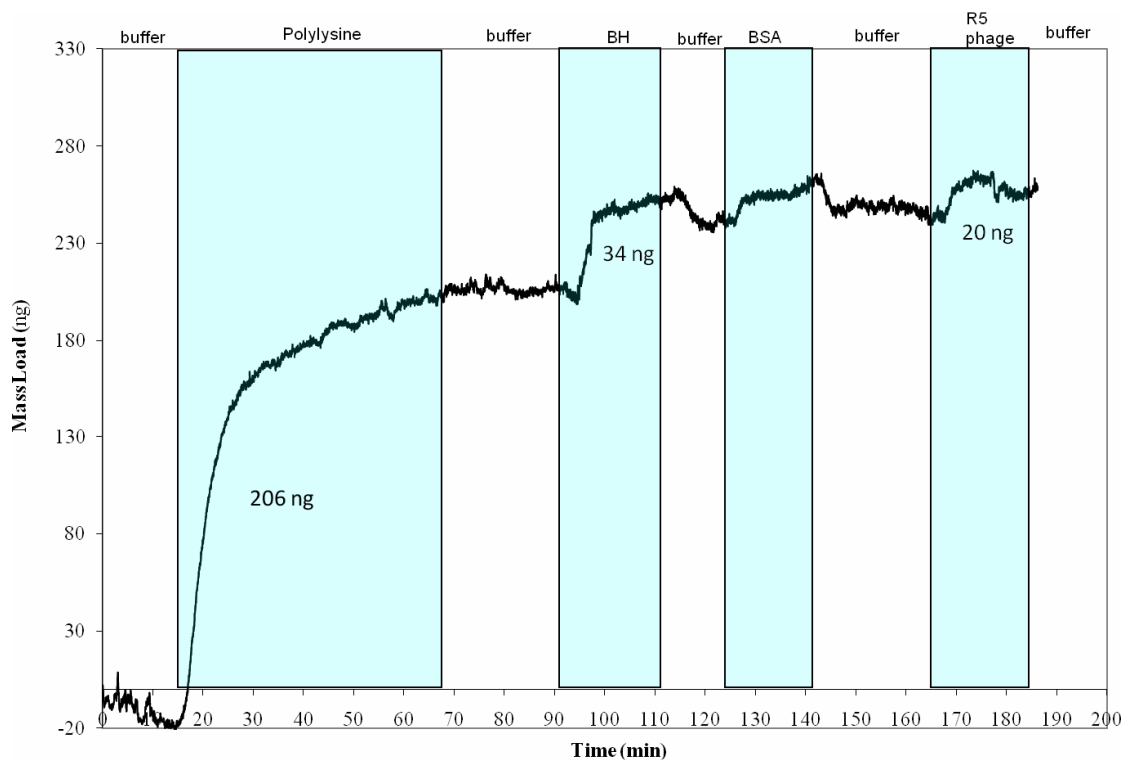


Figure 42. QCM quantification of round 5 phage recognition of beta-hematin surface. Approximately 34 ng of beta-hematin bound to the poly-lysine surface. The introduction of round 5 phage resulted in a mass loading of 20 ng, suggesting the successful recognition of panned phage and crystal.

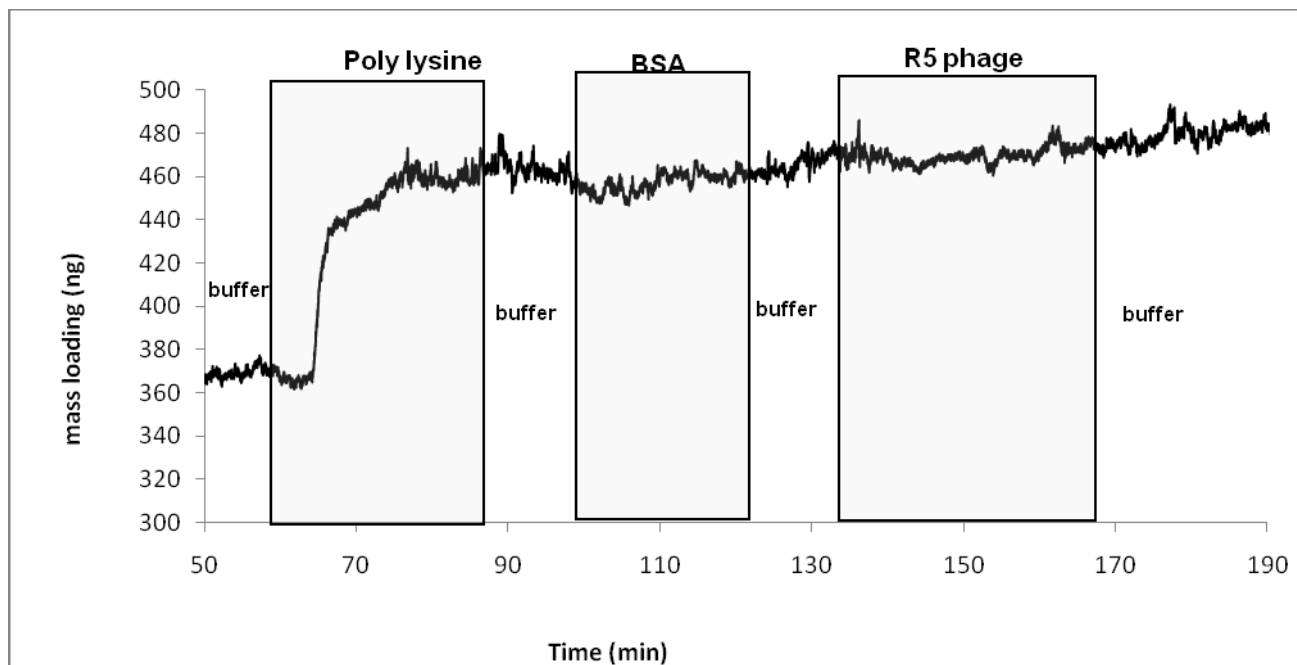


Figure 43. QCM measurements of round 5 phage and BSA-blocked poly-lysine served as a control for phage recognition of beta-hematin. No binding was detected for round 5 phage and BSA blocked poly-lysine surface, suggesting that mass loading (figure 42) detected for round 5 phage was a result of specific recognition for beta-hematin and not a result of nonspecific binding.

No significant binding was detected, confirming that previous observed binding of phage and crystal was a result of specific recognition by the phage particle for beta-hematin and not through nonspecific binding.

Phage peptides functionalities

Peptides are short, flexible amino acid sequences that can be quickly synthesized. Their ease of handling makes them a good candidate for a mediator or inhibitor of crystal growth. Approximately 200 phage viruses was identified from round 5 panning. These viruses were amplified and prepared for sequencing. Electrophoresis analysis of PCR product of isolated phage confirmed that DNA insert was 240bp (Figure 44). Purified PCR products were sequenced and 12 peptide sequences (Table 3) were identified. Three random, 7-mer peptides were generated to serve as control peptides. There is no observable trend in polarity and net charge for these peptides (Table 3). In fact, a wide range of hydrophilicity and net charge was exhibited. Pyridine quantification of beta-hematin formation under peptide mediation shows minimal conversion of heme with an average of 5% beta-hematin formation (Figure 45a). Three peptides expressed above average mediation at 10%, 17%, and 10%, EDKNNVA, ASDQEPS, and SITEDKN, respectively. FTIR and XRD characterization of product promoted by these peptides confirmed the successful formation of beta-hematin (Figure 46). Specifically, FTIR analysis exhibited beta-hematin characteristic peaks at 1664 cm^{-1} and 1210 cm^{-1} , denoting the presence of Fe(III)PPIX dimers. XRD measurements displayed peaks at 7, 22, 24 2theta, confirming the presence of beta-hematin unit cell. Together, these data unequivocally demonstrate the presence of beta-hematin. Analysis of EDKNNVA, ASDQEPS, and SITEDKN revealed that all peptides share similar hydrophilicity (EDKNNVA = 1.1, ASDQEPS = 0.9, SITEDKN = 1) with a ratio

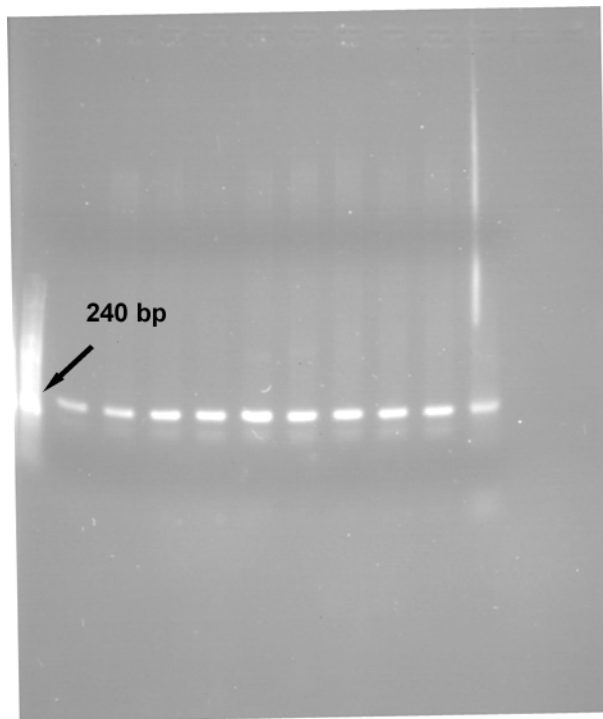


Figure 44. Electrophoresis analysis of round 5 PCR products confirmed the presence of 240 bp DNA fragment. Purified PCR products were used to identify the DNA sequence of beta-hematin specific 7-mer peptides.

Table 3. 7 amino acid sequence identified through phage panning. * denote control peptide (random scrambling of 7 amino acid sequence).

Sequence	MW	Average hydrophilicity	Ratio hydrophilic residues / total number residues	Iso-electric point	Net charge at pH 7.0
TWHTRHW*	1064.2	-0.8	14%	14	2.2
EDKNNVA	829.9	1.1	71%	7	0
EPSRPSR	868.9	1.4	71%	12.4	2
STFKKMD	897.1	0.7	57%	10.6	2
DTSRPSR	858.9	1.3	71%	12.4	2
PLGAAPG*	622.7	-0.4	0%	14	1
NNVATFE	834.9	-0.2	43%	7	0
KPSRPSR	868	1.4	71%	14	4
TAHLRIW*	937.1	-0.8	14%	14	2.1
ASDQEPS	773.8	0.9	71%	4.1	-1
EDKKPIR	926.1	1.9	71%	10.6	2
SITEDKN	846.9	1	71%	7	0
SIADQEP	799.8	0.6	57%	4.1	-1
NNVKTFE	892	0.3	57%	10.1	1
EDDQNNS	861.8	1.4	100%	3.7	-2

hydrophilic residues to total number of residues of 71%. Interestingly, four other peptides also possess a 71% hydrophilic residues, but do not exhibit above average percentage of heme conversion. All four of these peptides express a proline in the 5th position and a polar arginine in the 7th position, while three of the 4 peptides exhibit a serine in the 6th position. All four peptides promoted approximately 5% beta-hematin formation. Both EDKNNVA and SITEDKN have only one nonpolar residue towards the outer region of the peptide, suggesting that a heavily polar residue is more favorable for crystal formation. However, EDDQNNS contains all polar residues but did not promote beta-hematin. Scrambled peptides, TWHTRHA, TAHLRIW, and PLGAAPG, promoted no beta-hematin. The NP40 control, at 30.5 μ m, mediated 60 % beta-hematin formations. When compared to NP40, peptides are weak mediator of beta-hematin formation. In contrast to assays performed in acetate buffer, beta-hematin formation assay in citric buffer (37 C, pH 4.8, 12 hrs) did not promote crystallization (Figure 44b). The ability of concentrated acetate buffer to mediate beta-hematin was previously reported by Egan *et al.*(91) Similar to the presented peptide assay, beta-hematin formation in 4.5M acetate(91) solution produced crystal formation that follows a sigmoidal growth curve. In the first scenario, the acetate is likely to act as a phase transfer catalyst or work in conjunction with the peptide to promote beta-hematin nucleation. At a pH 4.8, the CB should have an overall negative charge, similar to acetate in this environment, suggesting that beta-hematin crystallization should proceed in both conditions. However, beta-hematin was only detected when acetate buffer was used in the assay. This result may be due to the amphiphilic characteristic of the acetate buffer at pH 4.8. In fact, lipid studies (chapter 1) and solvent studies (chapter 4) have demonstrated the importance of low dielectric environment during beta-hematin formation. Though citric buffer has charged regions, the hydrophobic region is not accessible due to steric hindrance.

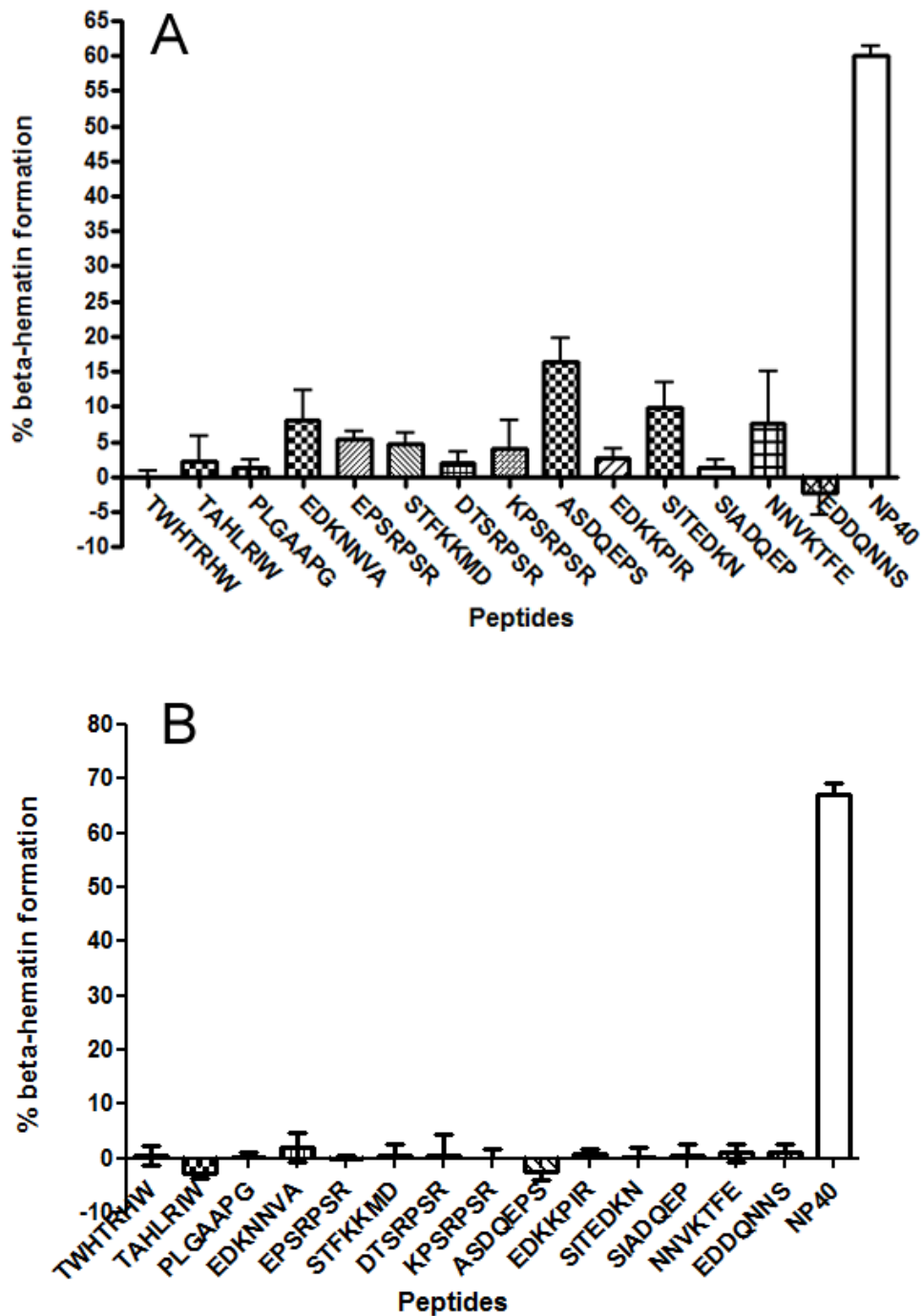


Figure 45. Peptide mediation of beta-hematin formation in acetate buffer and citric buffer conditions. In acetate buffer (a), three peptides (EDKNNVA, ASDQEPS, and SITEDKN) exhibited above average crystal formation. However, when compared to NP40, peptides are weak mediator of beta-hematin formation. No peptide exhibited beta-hematin promotion properties in citric buffer (b).

Fe(III)PPIX restricted access to the hydrophobic region of citric acid may explain why no beta-hematin is promoted in this buffer.

Next, the ability of these peptides to inhibit beta-hematin formation was assessed by incorporating 25 μ M chloroquine (CQ) to NP40 and peptides. Identified peptides do not exhibit beta-hematin inhibiting properties. The presence of the peptides did not prevent NP40 mediation of heme conversion. Furthermore, the percentage of heme conversion in the presence of NP40 and peptide appears to have additive properties. Mainly, an increased percentage of beta-hematin formation was measured for peptide+NP40 reaction (Figure 47). This increased amount is approximately the amount of product produced by the peptides alone, suggesting that two independent mechanism of crystal formation occurred.

Kinetics of peptide mediated beta-hematin formation

Kinetics curves of heme conversion exhibited similar sigmoidal curve pattern as those of beta-hematin formation in detergent(143) and acetic acid(91). This is likely due to the acetate buffer system that all three approaches employed in their assay. Heme conversion for ASDEQPS, EDKNNVA, and SITEDKN reached maximum formation approximately 5 hr into the reaction (Figure 48). ASDQEPS reached 15% crystal formation at 5.4 hr with a half life ($t_{1/2}$) at 5 hr. SITEDKN reached 12 % formation at 7.5 hr while EDKNNVA reached 11.5 % at 5.9 hr. When compared to the beta-hematin formation under NP40 mediation, the peptides heme conversion rates are nearly half as slow. In conjunction to peptide+NP40 data (Figure 47), similar rate of reaction between NP40 and peptides suggest that two independent mechanism of crystal formation took place.

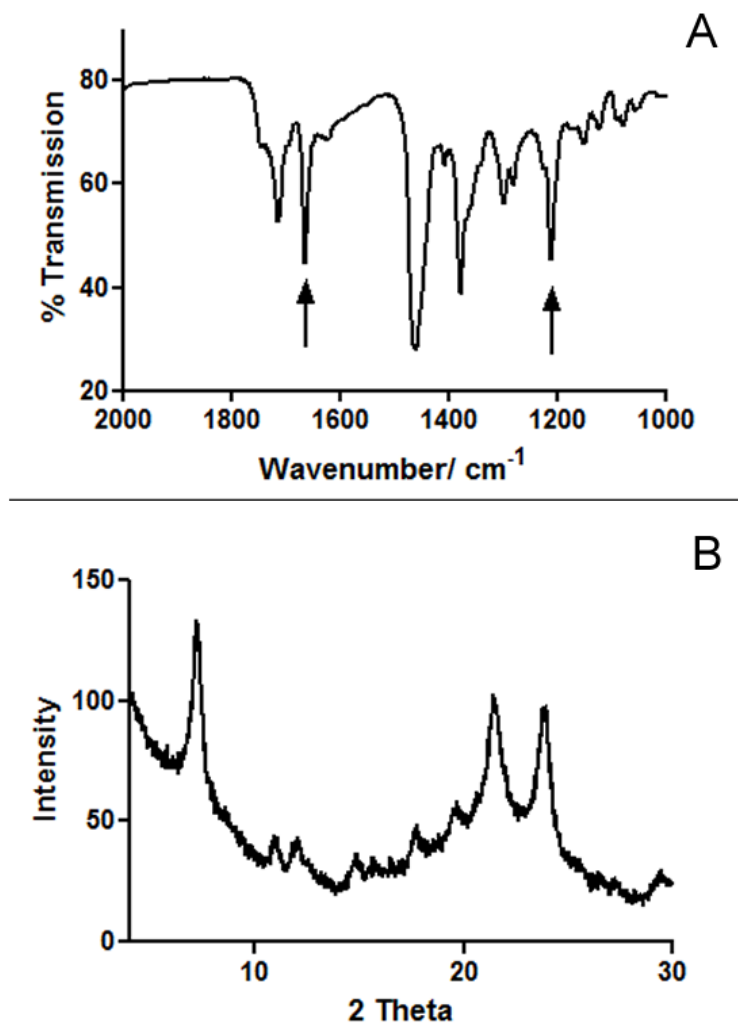


Figure 46. FTIR and XRD analysis of products form by EDKNNNVA. FTIR analysis(a) exhibit beta-hematin characteristic peaks at 1664 cm^{-1} and 1210 cm^{-1} . XRD measurement of product displayed beta-hematin characteristic peaks at 7, 22, 24 2theta, demonstrating the successful promotion of synthetic hemozoin.

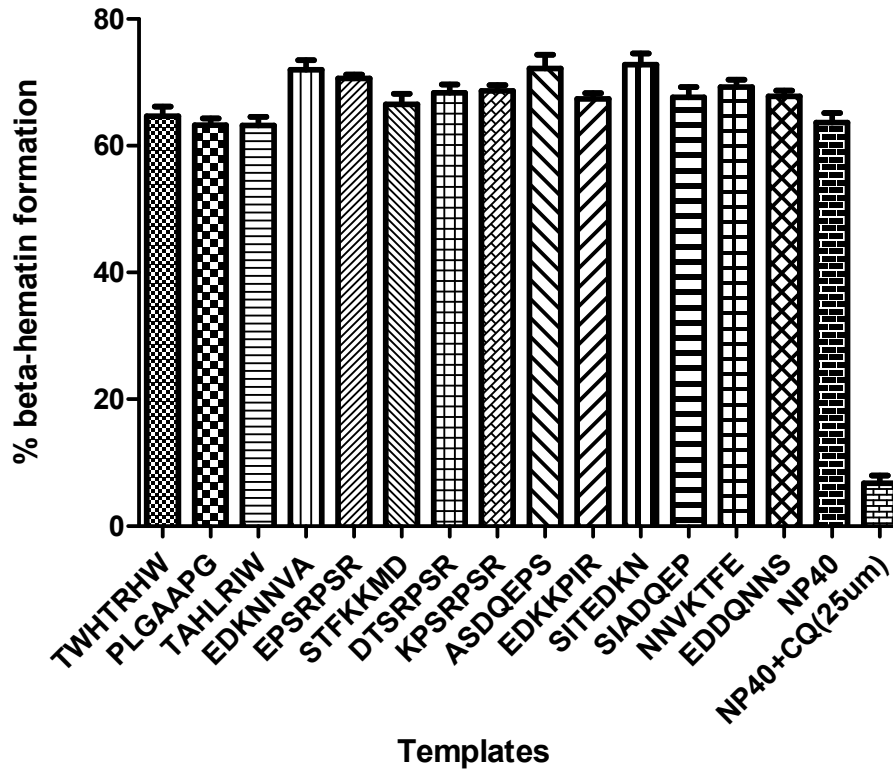


Figure 47. Peptides do not possess beta-hematin inhibiting properties. Incubation of NP40 and peptides with Fe(III)PPIX in acetate buffer did not inhibit crystal formation. Peptides that promoted (Figure 45) above average beta-hematin formation also promoted above average crystal formation the presence of NP40.

Orientation of peptides

Histidine-rich peptides (HRP) and proteins, characterized by their rich histidine and alanine, have been discovered in the digestive vacuole of the human malarial parasite(190) and was previously implicated as the *in vivo* catalyst for hemozoin formation.(49) HRP functionality extends beyond malaria as its roles in the biomineralization of heme,(49) copper, and zinc(191) have been established. However, studies using animal model with knockouts of the HRP genes concluded that HRP is a potent *in vitro* promoter of beta-hematin, but not the *in vivo* mediator for hemozoin formation. Nevertheless, the application of HRP in *in vitro* synthesis of nano assembly is abundant. For example, the HRP II epitope (AHHAHHAAD) is capable of stabilizing a variety of nanoclusters, including Au⁰ and Ag⁰ (192). Thus, it is surprising that none of the 12 peptides do not contain a histidine or alanine residue. In the epitope example, peptide ligands provide controllability of crystal morphologies by select ordering of residues at the bulk solution.(193) To examine the organization of peptides during beta-hematin synthesis in acetate buffer, dynamic light scattering (DLS) analysis was performed on dilution concentration (1 μM and 10 μM) of peptides (Figure 49). As predicted, ASDQEPS, EDKNNVA, and SITEDKN organized into aggregate bodies in the aqueous environment. All peptides appear to share similar aggregation trend. At low concentration, the size of peptide aggregation appears to be concentration dependent. ASDQEPS (Figure 49a) measurements is dominated with aggregates of 1mm at 1 μM and 3mM at 10 μM. Both EDKNNVA(Figure 49b) and SITEDKN (Figure 49c) produced smaller aggregates. At 1 μM peptide concentration, EDKNNVA measurements are dominated by peptide aggregates that are about 100nm in diameter, while SITEDKN measurements displayed a large population of peptide aggregates about 250 nm in size.

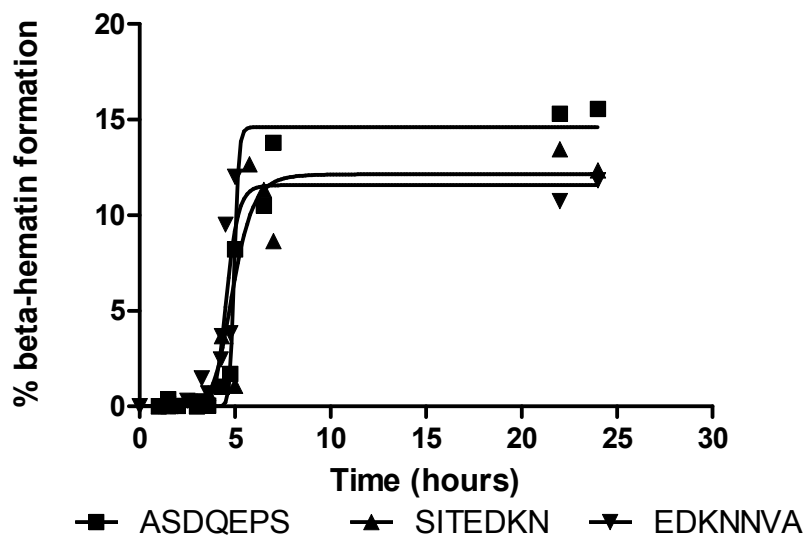


Figure 48. Kinetic of beta-hematin formation for ASDEQPS, SITEDKN, and EDKNNVA in acetate buffer. Heme conversion under all three peptide plateaued at approximately 5 hr into the reaction.

All peptides contain the 7 amino acids; however, the properties of these amino acids determine the degree of aggregation. EDKNNVA with an isoelectric point of 4.1 and an over charge of -1 at pH 4.8, produced the largest aggregation. This may be due to its largely charged ends. The first two residues on one end are glutamic-aspartic acid produces a 3 negative charges (carboxyl group of E and side chains of E and D). The other end of this peptide is predominately neutral and hydrophobic. At a pH 4.8, it is probable that this peptide organize with the hydrophobic region oriented inward with charged regions facing the bulk solution. This orientation will allow the negatively charged ends to Fe(III)PPIX molecules through ionic interactions. The polarized charge arrangement may increase aggregation size through static ionic interactions. SITEDKN's charge distribution is also skewed to the ends with two negatively charged residues followed by a positive (EDK). However, the concentration of negatively charged residues towards one end is not as heavy in SITEDKN as in EDKNNVA. This charge distribution may be responsible for the smaller size in peptide aggregation for SITEDKN. When compared to EDKNNVA and SITEDKN, ASDQEPS exhibits more equally distribution of charged residues. As a matter of fact, the negatively charged residues are spaced every other amino acid with two flanking residues being hydrophobic and neutrally charged at one end. This even distribution produced an overall -2 charge with no polarized charged ends and thus, may limit peptide aggregation.

The N-terminus of each peptide was acylated, producing an uncharged end. It is likely that, at pH 4.8, peptides are organized so that the N-terminus are oriented inward. EDKNNVA, SITEDKN, and ASDQEPS all possess a negatively charged C-terminus which can interact with the bulk Fe(III)PPIX solution through ionic interactions with the propionic group of Fe(III)PPIX molecules. Modeling studies of beta-hematin formation proposed that in the presence of water,

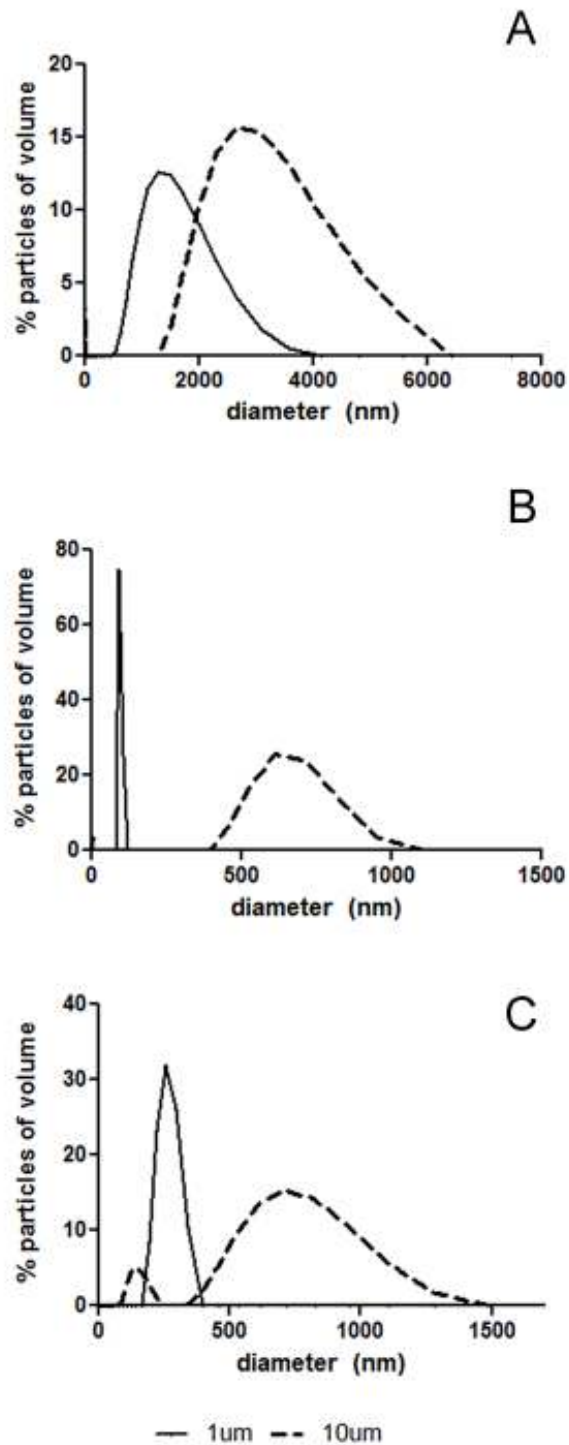


Figure 49. Dynamic light scattering (DLS) measurements of ASDQEPS (a), EDKNNVA (b), and SITEDKN (c). In aqueous environment, peptides spontaneously assembled into aggregated bodies. At 1 μM concentration, ASDQEPS formed aggregates larger than those of EDKNNVA and SITEDKN.

two Fe(III)PPIX molecules spontaneously dimerizes.(58) Crystal nucleation begins when the dimers assemble to form the growing crystal. However, in an aqueous environment, water molecules will hydrogen bond with the center iron, preventing dimer assembly. When beta-hematin crystallization occurs in an aqueous neutral lipid system, the lipid layer will eliminate water interactions, allowing crystal nucleation.(57, 58, 97) In the peptide system, this hydrophobic region is limited to only a few amino acid residues in length. This region may not be large enough to support continuous crystal growth, and thus, only a 10 percent beta-hematin formation was measured in the peptide system.

Peptide alignment with Heme Detoxification Protein

A budding proposal for hemozoin formation focuses on the Heme Detoxification Protein (HDP), a unique *Plasmodium* protein which is a potent beta-hematin promoter.(194) HDP investigation demonstrate that this protein is highly conserved across the *Plasmodium* genus, is extremely efficient in producing hemozoin, and is delivered to the food vacuole, the site of hemozoin formation, via a unique trafficking route.(194) Interestingly, when the phage peptides are aligned with the amino acid sequence of the HDP, EDKNNVA, SITEDKN, and ASDQEPS express high alignment. All seven amino acid exhibit good consecutive alignment with amino acid sequence of HDP (below). EDKNNVA, which is the best promoter of beta-hematin, exhibited the best alignment with HDP with all 7 amino acid possessing similar properties to those of HDP. Of those 5 amino acids, two are exact residue and five possess similar properties to its counterpart. SITEDKN and ASDQEPS exhibit two and one residues that are exact match, respectively. Scrambled peptide (control peptide), such as PLGAAPG, did not promote beta-

programmed components can provide the requisite building block for the assembly of new biologically inspired nanomaterials.

Future Directions

In this chapter, the proof demonstrating the application of phage display to beta-hematin crystal formation is presented. Initial virus screening and optimization of identified peptides suggest successful beta-hematin promotion by phage displayed identified peptides. The data presented here can serve as a stepping stone for understanding the molecular recognition involved during hemozoin formation. Future work for this project should investigate the controllability of beta-hematin morphologies based on peptide design. Long peptide chain may produce crystal that differs in shape from those produced by longer chain length. In addition, peptides with amphiphilic characteristic may be more successful at mediating beta-hematin formation. To increase phage display detection using QCM analysis, optimization of beta-hematin functionalization to QCM crystals must be performed.

Section Acknowledgements

The work in this chapter would not be complete without the assistant of several people. Special thanks to Dr. Catherine Purdom for her guidance and training on phage display techniques, Joshua Swartz and Stephen Jackson for their help with peptide synthesis, and Holly Carrell and Jamie Harrell for their assistant with PCR and DNA electrophoresis.

REFERENCES

1. Mann, S. (1993) Molecular Tectonics in Biomineralization and Biomimetic Materials Chemistry, *Nature* 365, 499-505.
2. Lowenstam, H. A. (1981) Minerals Formed by Organisms, *Science* 211, 1126-1131.
3. Sarikaya, M. (1999) Biomimetics: Materials Fabrication Through Biology, *Proc Natl Acad Sci U S A.* 96, 14183-14185.
4. Addadi, L., and Weiner, S. (1992) Control and Design Principles in Biological Mineralization, *Angew.Chem. Int. Ed.* 31, 153-169.
5. Knight, C. A., Cheng, C. C., and DeVries, A. L. (1991) Adsorption of Alpha-Helical Antifreeze Peptides on Specific Ice Crystal Planes. *Biophysical J.* 59, 409-418.
6. Addadi, L., and Weiner, S. (1985) Interaction between Acidic Proteins and Crystals: Stereochemical Requirements in Biomineralization. *Proc Natl Acad Sci U S A.* 82, 4110-4114.
7. Greenfield, G., Wilson, D. C., and Crenshaw, M. A. (1984) Ionotropic Nucleation of Calcium Carbonate by Molluscan Matrix, *Am Zool.* 24, 925-932.
8. Franceschi, V. R., and Nakata, P. A. (2005) Calcium Oxalate in Plants: Formation and Function, *Annu Rev Plant Biol* 56, 41-71.
9. Addadi, L., Weiner, S., and Geva, M. (2001) On How Proteins Interact with Crystals and Their Effect on Crystal Formation., *Z Kardiol.*, 90. Suppl 93:92-98.
10. Addadi, L., Rubin, N., Scheffer, L., and Ziblat, R. (2008) Two and Three-Dimensional Pattern Recognition of Organized Surfaces by Specific Antibodies, *Acc. Chem. Res.* 41, 254-264.
11. Ziegler, J., Linck, R., and Wright, D. W. (2001) Heme Aggregation inhibitors: antimalarial drugs targeting an essential biomineralization process, *Curr Med Chem.* 8, 171-189.
12. Carter, M. D., Hoang, A. N., and Wright, D. W. (2008) Hemozoin: A paradigm for biominerals in disease. , in *Wiley encyclopedia of chemical biology* pp 1-10, John Wiley & son.
13. Oliveira, M. F., d'Avila, J. C. P., Torres, C. R., Oliveira, P. L., Tempone, A. J., Rumjanek, F. D., Braga, C. M. S., Silva, J. R., Dansa-Petretski, M., Oliveira, M. A., de Souza, W., and Ferreira, S. T. (2000) Haemozoin in *Schistosoma mansoni*, *Molecular and Biochemical Parasitology* 111, 217-221.

14. Oliveira, M. F., Silva, J. R., Dansa-Petretski, M., de Souza, W., Braga, C. M. S., Masuda, H., and Oliveira, P. L. (2000) Haemozoin formation in the midgut of the blood-sucking insect *Rhodnius prolixus*, *FEBS letters* 477, 95-98.
15. Francis, S. E., Sullivan Jr., D. J., and Goldberg, D. E. (1997) Hemoglobin metabolism in the malaria parasite *Plasmodium falciparum*, *Annu. Rev. Microbiol.* 51, 97-123.
16. Tan, S. Y., and Ahana, A. (2009) Charles Laveran (1845-1922) : Nobel laureate pioneer of malaria, *Singapore Med J* 50, 657.
17. Organization, W. H. (2005) The world malaria report 2006.
18. Goldberg, D. E., Slater, A. F., Cerami, A., and Henderson, G. B. (1990) Hemoglobin degradation in the malaria parasite *Plasmodium falciparum*: an ordered process in a unique organelle, *Proc Natl Acad Sci U S A.* 87, 2931-2935.
19. Ginsburg, H., Kutner, S., Krugliak, M., and Cabantchik, Z. I. (1985) Characterization of permeation pathways appearing in the host membrane of *Plasmodium falciparum* infected red blood cells., *Mol Biochem Parasitol* 14, 313-322.
20. Hayward, R., Saliba, K. J., and Kirk, K. (2006) The pH of the digestive vacuole of *Plasmodium falciparum* is not associated with chloroquine resistance, *J Cell Sci* 119, 1016-1025.
21. Goldberg, D. E. (1993) Hemoglobin Degradation in Plasmodium-Infected Red Blood Cells, *Semin Cell Biol.* 4, 355.
22. Olliaro, P. L., and Goldberg, D. E. (1995) The Plasmodium Digestive Vacuole: Metabolic Headquarters and Choice Drug Target, *Paristol. Today* 11, 294.
23. Goldberg, D., Slater, A., Beavis, R., Chait, B., Cerami, A., and Henderson, G. (1991) Hemoglobin degradation in the human malaria pathogen *Plasmodium falciparum*: a catabolic pathway initiated by a specific aspartic protease, *J. Exp. Med.* 173, 961-969.
24. Perutz, M. (1987) The molecular Basis of Blood Diseases, W.B Saunders, Co., Philadelphia. pp. 127-178.
25. Rosenthal, P. J., McKerrow, J. H., Aikawa, M., Nagasawa, H., and Leech, J. H. (1988) A malarial cysteine proteinase is necessary for hemoglobin degradation by *Plasmodium falciparum*. *J Clin Invest* 82, 1560.
26. Kolakovich, K. A., Gluzman, I. Y., Duffin, K. L., and Goldberg, D. E. (1997) Generation of hemoglobin peptides in the acidic digestive vacuole of *Plasmodium falciparum* implicates peptide transport in amino acid production. *Mol Biochem Parasitol* 87, 123.
27. Courtesy of Dr. David Wright. (2010).
28. Ponka, P. (1999) Cell Biology of Heme, *Am J Med Sci.* 318, 241-256.

29. Balla, J., Balla, G., Jeney, V., Kakuk, G., Jacob, H., and Vercellotti, G. (2000) Ferriporphyrins and endothelium: a 2 edged sword-promotion of oxidation and induction of cytoprotectants, *Blood* 95, 3442-3450.
30. Schmitt, T. H., Frezzatti, W. A., and Schreier, S. (1993) Hemin-Induced Lipid Membrane Disorder and Increased Permeability: A Molecular Model for the Mechanism of Cell Lysis, *Archives of Biochemistry and Biophysics* 307, 96-103.
31. Schacter, B. (1988) Heme catabolism by heme oxygenase: physiology, regulation, and mechanism of action, *Semin. Hematol.* 25, 349-369.
32. Kimpara, T., Takeda, A., Watanae, K., Itoyama, Y., Ikawa, S., Watanae, M., Arai, H., Takahashi, K., and Shibahara, S. (1997) Microsatellite polymorphism in the human heme oxygenase-1 gene promoter and its application in association studies with Alzheimer and Parkinson disease, *Hum Genet* 100, 145-147.
33. Maines, M., Trakshell, G., and JKutty, R. (1986) Characterization of two constitutive forms of rat liver microsomal heme oxygenase: only one molecular species of the enzyme is inducible., *J. Biol. Chem.* 261, 411-419.
34. McCoubrey, W., Huang, T., and Maines, M. (1997) Isolation and characterization of a cDNA from the rat brain that encodes hemoprotein heme oxygenase-3, *Eur J. Biochem* 247, 725-732.
35. Tenhunen, R., Marver, H., and Schmid R. (1970) The enzymatic catabolism of hemoglobin: stimulation of microsomal heme oxygenase by hemin, *J Lab Clin Med* 75, 410-421.
36. Shibahara, S., Muller, R., H., T., and Yoshida, T. (1985) Cloning and expression of cDNA for rat heme oxygenase, *Proc Natl Acad Sci U S A.* 82, 7865-7869
37. Shibahara, S., Yoshida, T., and Kikuchi, G. (1978) Induction of heme oxygenase by heme in cultured pig alveolar macrophages, *Arch Biochem Biophys* 188, 243-250.
38. Yoshida, T., and Migita, C. (2000) Mechanism of heme degradation by heme oxygenase, *J Inorg Biochem* 82, 33-41.
39. Shibahara, S., Tomomi, K., and Kazuhito, T. (2002) Heme Degradation and Human Disease: diversity is the soul of life, *Antioxidants & Redox Signaling* 4, 593-602.
40. Pamplona, A., Ferreira, A., and Balla, J. (2007) Heme oxygenase-1 and carbon monoxide suppress the pathogenesis of experimental cerebral malaria, *Nat Med* 13, 703-710.
41. Pagola, S., Stephens, P. W., Bohle, D. S., Kosar, A. D., and Madsen, S. K. (2000) The structure of malaria pigment [β]-haematin, *Nature* 404, 307-310.

42. Slater, A. F., Swiggard, W. J., Orton, B. R., Flitter, W. D., Goldberg, D. E., Cerami, A., and Henderson, G. B. (1991) An iron-carboxylate bond links the heme units of malaria pigment, *Proc Natl Acad Sci U S A.* 88, 325-329.
43. Fitch, C. D., and Kanjanangulpan, P. (1987) The state of ferriprotoporphyrin IX in malaria pigment, *J Biol Chem* 262, 15552-15555.
44. Noland, G. S., Briones, N. B., and Sullivan, D. J. (2003) The shape and size of hemozoin crystals distinguishes diverse *Plasmodium* species, *Mol Biochem Parasitol.* 130, 91-99.
45. Buller, R., Peterson, M. L., Almarsson, O., and Leiserowitz, L. (2002) Quinoline Binding Site on Malaria Pigment Crystal: A Rational Pathway for Antimalaria Drug Design *Cryst. Growth Des.* 2, 553-562.
46. Egan, T. J., Combrinck, J. M., Egan, J., Hearne, G. R., Marques, H. M., Ntenti, S., Sewell, B. T., Smith, P. J., Taylor, D., van Schalkwyk, D. A., and Walden, J. C. (2002) Fate of haem iron in the malaria parasite *Plasmodium falciparum*, *Biochem. J.* 365, 343-347.
47. Slater, A. F. G., and Cerami, A. (1992) Inhibition by chloroquine of a novel haem polymerase enzyme activity in malaria trophozoites, *Nature* 355, 167-169.
48. Dorn, A., Stoffel, R., Matile, H., Bubendorf, A., and Ridley, R. G. (1995) Malarial haemozoin/[beta]-haematin supports haem polymerization in the absence of protein, *Nature* 374, 269-271.
49. Sullivan, D. J., Gluzman, I. Y., Russell, D. G., and Goldberg, D. E. (1996) On the molecular mechanism of chloroquine's antimalarial action, *Proc. Natl. Acad. USA* 93, 11865-11870.
50. Wellems, T. E., and Howard, R. J. (1986) *Proc Natl Acad Sci U S A.* 83, 6065.
51. Stahl, H. D., Kemp, D. J., Crewther, P. E., Scanlon, D. B., Woodrow, G., Brown, G. V., Bianco, A. E., Sanders, R. F., and Coppel, R. L. (1985) *Nucleic Acid. Res.* 13, 7837.
52. Papalexis, V., Siomos, M., Campanale, N.I., Guo, X., Kocak, G., Foley, M.I., Tilley, L. (2001) *Mol. Biochem. Parasitol.* 115, 77-86.
53. Sullivan, D. J. (2002) Theories on malarial pigment formation and quinoline action, *Int. J. Parasitol.* 32, 1645-1653.
54. Fitch, C. D., Kanjanangulpan, P. (1987) The state of ferriprotoporphyrin IX in malaria pigment, *J. Biol. Chem.* 15552.

55. Jackson, K. E., Klonis, N., Ferguson, D.J.P., Adisa, A., Dogovski, C., Tilley, L. (2004) Food vacuole-associated lipid bodies and heterogeneous lipid environments in the malaria parasite, *Plasmodium falciparum*, *Molec. Microbiol.* 54
56. Pisciotta, J. M., Coppens, I., Tripathi, A.K., Scholl, P.F., Shuman, J., Bajad, S., Shulaev, V., Sullivan, D.J. Jr. (2007) *Biochem J.* 402, 197-204.
57. Pisciotta, J. M., Coppens, I., Tripathi, A. K., Scholl, P. F., Shuman, J., Bajad, S., Shulaev, V., and Sullivan, D. J. (2007) The role of neutral lipid nanospheres in *Plasmodium falciparum* haem crystallization, *Biochem J.* 402, 197-204.
58. Egan, T. J., Chen, J. Y.-J., de Villiers, K. A., Mobotha, T. E., Naidoo, K. J., Ncokazi, K. K., Langford, S. J., McNaughton, D., Pandiancherri, S., and Wood, B. R. (2006) Haemozoin (beta-haematin) biomineralization occurs by self-assembly near the lipid/water interface, *FEBS Lett.* 580, 5105-5110.
59. Yayon, A., Cabantchik, Z.I., Ginsburg, H. (1985) Susceptibility of human malaria parasites to chloroquine is pH dependent, *Proc. Natl. Acad. Sci. U.S.A.* 82, 2784-2788.
60. Gary, T. G., Jensen, J.B., Ginsburg, H. (1986) Uptake of (3H) chloroquine by drug sensitive and resistant strains of the human malaria parasite *Plasmodium falciparum*, *Biochem. Pharmacol.* 35, 3805-3812.
61. Bray, P. G., Boulter, M.K., Ritchie, G.Y., Ward, S.A. (1994) Relationship of global chloroquine transport and reversal of resistance in *Plasmodium falciparum*, *Mol. Biochem. Parasitol.* 63, 87-94.
62. Hawley, S. R., Bray, P.G., Park, B.K., Ward, S.A. (1996) The role of drug accumulation in 4-aminoquinoline antimalarial potency. The influence of structural substitution and physicochemical properties. *Mol. Biochem. Parasitol.* 80, 15-25.
63. Hawley, S. R., Bray, P.G., O'Neil, P.M., Park, K., Ward, S.A. (1996) *Biochem. Parasitol.* 52, 723-733.
64. Hawley, S. R., Bray, P.G., Mungthin, M., Atkinson, J.D., Neill, P.M., Ward, S.A. . (1998) Relationship between Antimalarial Drug Activity, Accumulation, and Inhibition of Heme Polymerization in *Plasmodium falciparum* In Vitro, *Antimicrob. Agents Chemother.* 42, 682-686.
65. Dorn, A., Vippagunta, S.R., Matile, H., Bubendorf, A., Vennerstrom, J.L., Ridley, R.G. (1998) A comparison and analysis of several ways to promote haematin (haem) polymerisation and an assessment of its initiation *in vitro*., *Biochem. Pharmacol.* 55, 737.
66. Warhurst, D. C. The quinine-haemin interaction and its relationship to antimalarial activity. *Biochem. Pharm.* 30, 3323.

67. Ridley, R. G., Dorn, A., Vippagunta, S. R., and Vennerstrom, J. L. (1997) Haematin (haem) polymerization and its inhibition by quinoline antimalarials. *Ann. Trop Med Parasitol* 109, 97.
68. Fitch, C. D. (1998) Involvement of heme in the antimalarial action of chloroquine. *Trans. Am. Clin. Climatol. Assoc.* 109, 97.
69. Cooper, R. A., Hartwig, C. L., and Ferdig, M. T. (2005) Pfcr1 is more than the Plasmodium falciparum chloroquine resistance gene: a functional and evolutionary perspective, *Acta Trop.* 94, 170-180.
70. Ancelin, M. L., and Vial, H. J. (1992) Saturable and non-saturable components of choline transport in Plasmodium-infected mammalian erythrocytes: possible role of experimental conditions, *Biochem. J.* 283, 619-621.
71. Holz, G. G. J. (1977) Lipids and the malarial parasite, *Bull World Health Organ.* 55, 237-248.
72. Vielemeyer, O., McIntosh, M. T., Joiner, K. A., and Coppens, I. (2004) Neutral lipid synthesis and storage in the intraerythrocytic stages of Plasmodium falciparum, *Molecular and Biochemical Parasitology* 135, 197-209.
73. Jackson, K. E., Klonis, N., Ferguson, D. J. P., Adisa, A., Dogovski, C., and Tilley, L. (2004) Food vacuole-associated lipid bodies and heterogeneous lipid environments in the malaria parasite, *Plasmodium falciparum*, *Mol Microbiol.* 54, 109-122.
74. Nawabi, P., Lykidis, A., Ji, D., and Haldar, K. (2003) Neutral-Lipid Analysis Reveals Elevation of Acylglycerols and Lack of Cholesterol Esters in Plasmodium falciparum-Infected Erythrocytes, *Eukaryotic Cell* 2, 1128-1131.
75. Trager, W. (2003) The formation of haemozoin - further intrigue, *Trends in Parasitology* 19, 388-388.
76. Palacpac, N. M. Q., Hiramane, Y., Mi-ichi, F., Torii, M., Kita, K., Hiramatsu, R., Horii, T., and Mitamura, T. (2004) Developmental-stage-specific triacylglycerol biosynthesis, degradation and trafficking as lipid bodies in Plasmodium falciparum-infected erythrocytes, *J Cell Sci* 117, 1469-1480.
77. Oliveira, M. F., Kycia, S. W., Gomez, A., Kosar, A. D., Bohle, D. S., Hempelmann, E., Menezes, D., Vannier-Santos, M. A., Oliveira, P. L., and Ferreira, S. T. (2005) Structural and morphological characterization of hemozoin produced by Schistosoma mansoni and Rhodnius prolixus, *FEBS lett.* 579, 6010-6016.
78. Greenspan, P., Mayer, E. P., and Fowler, S. D. (1985) Nile red: a selective fluorescent stain for intracellular lipid droplets, *J. Cell Biol.* 10, 965-973.

79. Ncokazi, K. K., and Egan, T. J. (2005) A colorimetric high-throughput [beta]-hematin inhibition screening assay for use in the search for antimalarial compounds, *Anal Biochem.* 338, 306-319.
80. Solomonov, I., Osipova, M., Feldman, Y., Baetz, C., Kjaer, K., Robinson, I. K., Webster, G. T., McNaughton, D., Wood, B. R., Weissbuch, I., and Leiserowitz, L. (2007) Crystal Nucleation, Growth, and Morphology of the Synthetic Malaria Pigment β -Hematin and the Effect Thereon by Quinoline Additives: The Malaria Pigment as a Target of Various Antimalarial Drugs, *J Am Chem Soc.* 129, 2615-2627.
81. Oliveira, M. F., Silva, J. R., Dansa-Petretski, M., de Souza, W., Lins, U., Braga, C. M. S., Masuda, H., and Oliveira, P. L. (1999) Haem detoxification by an insect, *Nature* 400, 517-518.
82. Oliveira, M. F., Gandara, A. C. P., Braga, C. M. S., Silva, J. R., Mury, F. B., Dansa-Petretski, M., Menezes, D., Vannier-Santo, s. M. A., and Oliveira, P. L. (2007) Heme crystalization in the midgut of triatomine insects., *Comp Biochem Physiol C* 146, 168-174.
83. Mattson, F. H., and Volpenhein, R. A. (1962) Synthesis and properties of glycerides, *J. Lipid Res.* 3, 281-296.
84. Berlin, E., and Sainz, E. (1986) Acyl chain interactions and the modulation of phase changes in glycerolipids., *Biochim Biophys Acta.* 855, 1-7.
85. Salonen, A., Guillot, S., and Glatter, O. (2007) Determination of Water Content in Internally Self-Assembled Monoglyceride-Based Dispersions from the Bulk Phase, *Langmuir* 23, 9151-9154.
86. Weiner, S. (1986) Organization of extracellularly mineralized tissues: a comparative study of biological crystal growth, *CRC Crit Rev Biochem* 20, 365-408.
87. Huy, N. T., Maeda, A., Uyen, D. T., Trang, D. T. X., Shiono, M. T., Oida, T., Harada, S., and Kamei, K. (2007) Alcohols induced beta-hematin formation via the dissociation of aggregated heme and reduction in interfacial tension of the solution, *Act Tropica* 101, 130-138.
88. Coppens, I., Vielemeyer, O. (2005) Insights into unique physiological features of neutral lipids in Apicomplexa: from storage to potential mediation in parasite metabolic activities, *Int. J. Parasitol.* 35, 597-615.
89. De Villiers, K., Osipova, M., Mabothe, T., Solomonov, I., Feldman, Y., Kjaer, K., Weissbuch, I., Egan, T., and Leiserowitz, L. (2009) Oriented Nucleation of Beta-hematin Crystals Induced by Various Interfaces: Relevance to Hemozoin Formation, *Cryst. Growth Des.* 9, 626-632.
90. Egan, T. J., and Tshivhase, M. G. (2006) Kinetics of beta-haematin formation from suspensions of haematin in aqueous benzoic acid, *Dalton Trans.*, 5024-5032.

91. Egan, T. J., Mavuso, W. W., and Ncokazi, K. K. (2001) The mechanism of beta-hematin formation in acetate solution. Parallels between hemozoin formation and biomineralization processes, *Biochemistry* 40, 204-213.
92. Murphy, D. J. (2001) The biogenesis and functions of lipid bodies in animals, plants and microorganisms, *Prog. Lipid. Res.* 40, 325-438.
93. Coppens, I., and Vielemeyer, O. (2005) Insights into unique physiological features of neutral lipids in Apicomplexa: from storage to potential mediation in parasite metabolic activities, *Int. J. Parasitol.* 35, 597-615.
94. Jackson, K. E., Klonis, N., Ferguson, D. J. P., Adisa, A., Dogovski, C., and Tilley, L. (2004) Food vacuole-associated lipid bodies and heterogeneous lipid environments in the malaria parasite, *Plasmodium falciparum*, *Mol. Microbiol.* 54, 109-122.
95. Egan, T. J., Chen, J. Y.-J., de Villiers, K. A., Mabothe, T. E., Naidoo, K. J., Ncokazi, K. K., Langford, S. J., McNaughton, D., Pandiancherri, S., and Wood, B. R. (2006) Haemozoin (b-haematin) biomineralization occurs by self-assembly near the lipid/water interface, *FEBS Lett.* 580, 5105-5110.
96. Hoang, A. N., Ncokazi, K. K., de Villiers, K. A., Wright, D. W., and Egan, T. J. (2010) Crystallization of synthetic haemozoin (b-haematin) nucleated at the surface of lipid particles, *Dalton Trans.* 39, 1235-1244.
97. Hoang, A. N., Ncokazi, K. K., de Villiers, K. A., Wright, D. W., and Egan, T. J. (2010) Crystallization of synthetic haemozoin (beta-haematin) nucleated at the surface of lipid particles, *Dalton Trans.* 39, 1235-1244.
98. Morley, W. G., and Tiddy, G. J. T. (1993) Phase behaviour of monoglyceride/water systems, *J. Chem. Soc., Faraday Trans.* 88, 2823-2831.
99. Krog, N. J. (2001) Crystallization properties and lyotropic phase behavior of food emulsifiers. , in *Crystallization processes in fats and lipid system*. (Garti, N., and Sato, K., Eds.), pp 505-526, Marcel Dekker, IN, New York.
100. Gunston, F. D., and Padley, F. B. (1997) *Lipid Technologies and Applications*, Marcel Dekker, Inc, New York.
101. Egan, T. J., Combrinck, J. M., Egan, J., Hearne, G. R., Marques, H. M., Ntenti, S., Sewell, B. T., Smith, P. J., Taylor, D., van Schalkwyk, D. A., and Walden, J. C. (2002) Fate of haem iron in the malaria parasite *Plasmodium falciparum*, *Biochem. J.* 365, 343-347.
102. Cheng, Z., and Li, Y. (2007) What is responsible for the initiating chemistry of iron-mediated lipid peroxidation: an update,, *Chem. Rev.* 107, 747-766.

103. Greenspan, P., Mayer, E. P., and Fowler, S. D. (1985) Nile red: a selective fluorescent stain for intracellular lipid droplets, *J. Cell Biol.* *100*, 965-973.
104. Reichardt, C. (1994) Solvatochromic dyes as solvent polarity indicators, *Chem. Rev.* *94*, 2319-2358.
105. Solomonov, I., Osipova, M., Feldman, Y., Baetz, C., Kjaer, K., Robinson, I. K., Webster, G. T., McNaughton, D., Wood, B. R., Weissbuch, I., and Leiserowitz, L. (2007) Crystal nucleation, growth, and morphology of the synthetic malaria pigment b-hematin and the effect thereon by quinoline additives: the malaria pigment as a target of various antimalarial drugs, *J. Am. Chem. Soc.* *129*, 2615-2627.
106. Lakowicz, J. R. (2006) *Principles of fluorescence spectroscopy*, 3 ed., Springer Science and Business Media, New York City.
107. Yayon, A., Cabantchik, Z. I., and Ginsburg, H. (1984) Identification of the acidic compartment of *Plasmodium falciparum*-infected human erythrocytes as the target of the antimalarial drug chloroquine, *EMBO J.* *3*, 2695-2700.
108. Geary, T. G., Divo, A. D., Jensen, J. B., Zangwill, M., and Ginsburg, H. (1990) Kinetic modelling of the response of *Plasmodium falciparum* to chloroquine and its experimental testing *in vitro*, *Biochem. Pharmacol.* *40*, 685-691.
109. Hayward, R., Saliba, K. J., and Kirk, K. (2006) The pH of the digestive vacuole of *Plasmodium falciparum* is not associated with chloroquine resistance, *J. Cell Sci.* *119*, 1016-1025.
110. Egan, T. J., Mavuso, W. W., and Ncokazi, K. K. (2001) The mechanism of b-hematin formation in acetate solution. Parallels between hemozoin formation and biomineralization processes, *Biochemistry* *40*, 204-213.
111. Egan, T. J., and Tshivhase, M. G. (2006) Kinetics of b-haematin formation from suspensions in aqueous benzoic acid, *Dalton Trans.*, 5024-5032.
112. Palacpac, N. M. Q., Hiramane, Y., Seto, S., Hiramatsu, R., Horii, T., and Mitamura, T. (2004) Evidence that *Plasmodium falciparum* diacylglycerol acyltransferase is essential for intraerythrocytic proliferation, *Biochem. Biophys. Res. Commun.* *321*, 1062-1068.
113. Mitamura, T., and Palacpac, N. M. Q. (2003) Lipid metabolism in *Plasmodium falciparum*-infected erythrocytes: possible new targets for malaria chemotherapy, *Microbes Infect.* *5*, 545-552.
114. Vielemeyer, O., McIntosh, M. T., Joiner, K. A., and Coppens, I. (2004) Neutral lipid synthesis and storage in the intraerythrocytic stages of *Plasmodium falciparum*, *Mol. Biochem. Parasitol.* *135*, 195-207.

115. Egan, T. J. (2008) Haemozoin formation, *Mol Biochem Parasitol* 268, 127-136.
116. Jeney, V., Balla J., Yachie, A., Varga, Z., Vercellotti, G. M., Eaton, J. W., and Balla, D. (2002) Pro-oxidant and cytotoxic effects of circulating heme, *Blood* 100, 879-887.
117. Larsson, S. C., Adami, H. O., Giovannucci, E., and Wolk, A. (2005) Heme iron, zinc, alcohol consumption, and risk of colon cancer, *J. Natl Cancer Inst* 97, 232-2333.
118. Pierre, F., Tache, S., Petit, C. R., Van der Meer, R., and Corpet, D. E. (2003) Meat and cancer: haemoglobin and haemin in low-calcium diet promote colorectal carcinogenesis at the aberrant crypt stage in rats, *Carcinogenesis* 24, 1683-1690.
119. Kumar, S., and Bandyopadhyay, U. (2005) Free heme toxicity and its detoxification systems in human, *Toxicol. Lett.* 157, 175-188.
120. Davies, M. (1988) Detection of peroxy and alkoxy radicals produced by reaction of hydroperoxides with heme-proteins by electron spin resonance spectroscopy, *Biochim Biophys Acta.* 964, 28-35.
121. Van der Zee, J., Barr, D., and Mason, R. (1996) ESR spin trapping investigation of radical formation from the reaction between hematin and tert-butyl hydroperoxide., *Free Radic. Biol. Med.* 20, 199-206.
122. Tappel, A. (1995) Unsaturated lipid oxidation catalyzed by hematin compounds, *J. Biol. Chem.* 270, 721-733.
123. Gutteridge, J., and Smith, A. (1988) antioxidant protection by haemopexin of haem stimulated lipid peroxidation, *Biochem J* 256, 861-865.
124. Aft, R., and Mueller, G. (1984) Hemin-mediated oxidative degradation of proteins, *J. Biol. Chem.* 259, 301-305.
125. Aft, R., and Mueller, G. (1983) Hemin-mediated DNA strand scission., *J. Biol. Chem.* 258, 12069-12072.
126. Rudzinska, M. A., Trager, W., and Bray, R. S. (1965) Pinocytotic uptake and the digestion of hemoglobin in malaria parasites., *J. Protozool* 12, 563.
127. Li, C., Orbulescu, G., Sui, R. M., and Leblanc, R. M. (2004) Amyloid-like formation by self-assembly of peptidolipids in two dimensions, *Langmuir* 20, 8641-8645.
128. Triulzi, R. C., Li, C., Naistat, D., Orbulescu, J., and Leblanc, R. M. (2007) A two-dimensional approach to study amyloid beta-peptide fragment (25-35), *J. Phys. Chem C* 111, 4661-4666.

129. Thakur, G., Micic, M., and Leblanc, R. M. (2009) Surface chemistry of Alzheimer's disease: a langmuir monolayer approach, *Colloids and surfaces B: Biointerfaces* 74, 436-456.
130. Mitomo, H., Chen, W. H., and Regen, S. L. (2009) Oxysterol Induced rearrangement of the liquid-ordered phase: a possible linked to Alzheimer's disease, *J. Am. Chem. Soc* 131.
131. Chimote, G., and Banerjee, R. (2005) Lung surfactant dysfunction in tuberculosis: Effect of mycobacterial tubercular lipids on dipalmitoylphosphatidylcholine surface activity, *2005* 45, 215-223.
132. Ulman, W. (1991) *Ultrathin Organic Films*, Academic Press, Inc, New York.
133. Hann, R. A. (1990) in *Langmuir-Blodgett Films* (Roberts, G., Ed.), p 558, Plenum Press, New York.
134. Holman, K. T., Pivovar, A. M., Swift, J. A., and Ward, M. D. (2001) *Acc. Chem. Res.* 34, 107-118.
135. Egan, T. J., Hunter, R., Kaschula, C. H., Marques, H. M., Misplon, A., and Walden, J. C. (2000) Structure-function relationships in aminoquinolines: effect of amino and chloro groups on quinoline-hematin complex formation, inhibition of beta-hematin formation and antiplasmodial activity, *J. Med Chem* 43, 283-291.
136. Egan, T. J., Ross, D. C., and Adams, P. A. (1994) Quinoline anti-malarial drugs inhibit spontaneous formation of beta-hematin (malaria pigment), *FEBS Lett.* 352, 54-57.
137. Egan, T. J., Mavuso, W. W., Ross, D. C., and Marques, H. M. (1997) Thermodynamic factors controlling the interaction of quinoline antimalarial drugs with ferriprotoporphyrin IX, *J. Inorg. Biochem.* 68, 137-145.
138. Dorn, A., Vippagunta, S. R., Matile, H., Bubendorf, A., Vennerstrom, J. L., and Ridley, R. G. (1998) A comparison and analysis of several ways to promote haematin (haem) polymerisation and an assessment of its initiation in vitro., *Biochem Pharmacol.* 55, 737-747.
139. White, K. A., and Marletta, M. A. (1992) Nitric oxide synthase is a cytochrome p-450 type hemoprotein., *Biochemistry* 31, 6627-6631.
140. Ignarro, L. J., Ballot, B., and Wood, K. S. (1984) Regulation of soluble guanylate cyclase activity by porphyrins and metalloporphyrins. , *J. Biol. Chem.* 259, 6201-6207.
141. Ryter, S. W., and Tyrrell, R. M. (2000) The heme synthesis and degradation pathways: role in oxidant sensitivity. Heme oxygenase has both pro- and antioxidant properties. , *Free Radic Biol Med.* 28, 289-309.

142. Homewood, C. A., Jewsbury, J. M., and Chance, M. L. (1972) The pigment formed during haemoglobin digestion by malarial and schistosomal parasites., *Comp. Biochem. Physiol.* 43, 517–523.
143. Carter, M. D., Phelan, V. V., Sandlin R.D, Bachmann, B. O., and Wright, D. W. (2010) Lipophilic mediated assays for beta-hematin inhibitors, *Comb Chem High Throughput Screen* 13, 285-292.
144. Oliveira, M. F., Timm, B. L., Machado, E. A., Miranda, K., Attias, M., Silva, J. R., Dansa-Petretski, M., de Oliveira, M. A., de Souza, W., Sousa, N. M., Vugman, N. V., and Oliveira, P. L. (2002) On the pro-oxidant effects of haemozoin, *FEBS Lett.* 512, 139-144.
145. Tekwani, B. L., and Walker, L. A. (2005) Targeting the hemozoin synthesis pathway for new antimalarial drug discovery: technologies for in vitro beta-hematin formation assay, *Comb Chem High Throughput Screen* 8, 63-79.
146. Newman, D. M., Heptinstall, J., Matelon, R. J., Savage, L., Wears, M. L., Beddow, J., Cox, M., Schallig, H. D. F. H., and Mens, P. (2008) A magneto-optic route toward the in vivo diagnosis of malaria: preliminary results and preclinical trial data, *Biophys J.* 95, 994-1000.
147. Falk, J. E. (1964) *Porphyrins and Metalloporphyrins. Their General, Physical and Coordination Chemistry, and Laboratory Methods*, Vol. 2, Elsevier.
148. Kiss, G., and Hansson, C. (2004) Application of osmolality for the determination of water activity and the modelling of cloud formation., *Atmos. Chem. Phys. Discuss.* 4, 7667-7689.
149. Stiebler, R., Timm, B. L., Oliveira, P. L., Hearne, G. R., Egan, T. J., and Oliveira, M. F. (2010) On the physico-chemical and physiological requirements of hemozoin formation promoted by perimicrovillar membranes in *Rhodnius prolixus* midgut. , *Insect Biochemistry and Molecular Biology in press*.
150. de villiers, K. A., Kaschula, C. H., Egan, T. J., and Marques, H. M. (2007) Speciation and structure of ferriprotoporphyrin IX in aqueous solution: spectroscopic and diffusion measurements demonstrate dimerization, but not mu-oxo dimer formation, *J Biol Chem* 12, 101-117.
151. Blauer, G., Akkawi, M. (2002) Alcohol-water as a novel medium for beta-hematin preparation., *Arch Biochem Biophys* 398, 7-11.
152. Bohle, S. D., Dinnebier, R. E., Madsen, S. K., and Stephens, P. W. (1997) Characterization of the product of the heme detoxification pathway in malarial late trophozoites by X-ray diffraction., *J. Biol. Chem.* 272, 713-716.

153. Egan, T. J., and Ncokazi, K. K. (2005) Quinoline antimalarials decrease the rate of [beta]-hematin formation, *Journal of Inorganic Biochemistry* 99, 1532-1539.
154. Bohle, D. S., Kosar, A. D., and Stephens, P. W. (2003) The reversible hydration of the malaria pigment β -hematin, *Can. J. Chem.* 81, 1285-1291.
155. Dupont, Y., and Pougeois, R. (1983) Evaluation of H₂O activity in the free or phosphorylated catalytic site of Ca²⁺-ATPase., *FEBS Lett.* 156, 93-98.
156. Corrêa Soares, J. B., Maya-Monteiro, C. M., Bittencourt-Cunha, P. R., Atella, G. C., Lara, F. A., d'Avila, J. C., Menezes, D., Vannier-Santos, M. A., Oliveira, P. L., Egan, T. J., and Oliveira, M. F. (2007) Extracellular lipid droplets promote hemozoin crystallization in the gut of the blood fluke *Schistosoma mansoni*., *FEBS Lett.* 581, 1742-1750.
157. Stiebler, R., Hoang, A. N., Egan, T. J., Wright, D. W., and Oliveira, M. F. (2010) Increase on the steady-state soluble heme levels in acidic conditions is an important mechanism for spontaneous heme crystallization *in vitro*, *PLOS-ONE*.
158. Bohle, D. S., Kosar, A. D., and Stephens, P. W. (2002) Phase homogeneity and crystal morphology of the malaria pigment beta-hematin, *Acta Cryst D*58, 1752-1756.
159. Orlov, P. P. (1928) *Izv. Akad. Nauk*, 529.
160. Brown, S. B. (1969) *Biochem J.* 115, 279-285.
161. Egan, T. J., and Ncokazi, K. K. (2004) Effects of solvent composition and ionic strength on the interaction of quinoline and antimalarials with ferriprotophyrin IX, *J Inorg Biochem* 98, 144-152.
162. Parthasarathi, N., Hansen, C., Yamaguchi, S., and Spiro, T. G. (1987) Metalloporphyrin core size resonance Raman marker bands revisited: implications for the interpretation of hemoglobin photoproduct Raman frequencies, *J Am Chem Soc.* 109, 3865.
163. Choi, S., Spiro, T. G., Langry, K. C., Smith, K.C., Budd, D. L., and Lamarr, G. N. (1982) *J Am Chem Soc.* 104, 4345.
164. Mashiko, T., Kastner, M. E., Spertalian, K., Scheidt, W. R., and Reed, C. A. (1978) *J Am Chem Soc.* 100, 6354.
165. Granberg, R., and Rasmuson, A. (2005) Crystal growth rates of paracetamol in mixtures of water + acetone + toluene, *Particle Technology Fluidization* 51, 2441.
166. Loudon, G. (2002) *Organic Chemistry* 4th ed. ed., Oxford University Press, New York.

167. Coppens, I., and Vielemeyer, O. (2005) Insights into unique physiological features of neutral lipids in Apicomplexa: from storage to potential mediation in parasite metabolic activities, *International Journal for Parasitology* 35, 597-615.
168. Naik, R. R., Brott, L.L., Clarson, S.K., Stone, M.O. (2002) Silica-precipitating peptides isolated from a combinatorial phage display peptide library., *J. Nanosci. Nanotech.*, 95-100.
169. Peelle, B. R., Krauland, E.M., Wittrup, K.D., Belcher, A.M. (2005) "Probing the interface between biomolecules and inorganic materials using yeast surface display and genetic engineering, *Acta Biomater.* 2, 145-154.
170. Whaley, R. S., English, D.S., Hu, E.L., Barbara, P.F., Belcher, A.M. (2000) Peptides with Semiconductor Binding Specificity for Directed Nanocrystal Assembly, *Nature* 405, 665.
171. Tomczak, M. M., Slocik, M.O., Nail, R.R. (2007) Bio-based approaches to inorganic material synthesis, *Biochem. Soc. Trans.* 35 part III, 512.
172. Kroger, N., Deutzmann, R., Sumper, M. (1999) Polycationic peptides from diatom biosilica that direct silica nanosphere formation, *Science* 286, 1129-1132.
173. Shimizu, K., Cha, J., Stucky, G.D., Morse, D.E. (1998) Silicatein α : Cathepsin L-like protein in sponge biosilica, *Proc. Natl. Acad. Sci. U.S.A* 95, 6234-6238.
174. Tomczak, M. M., Glawe, D.D., Drummy, L.F., Lawrence, C.G., Stone, M.O., Perry, C.C., Pochan, D.J., Deming, T.J., Naik, R.R. . (2005) *J Am Chem Soc.* 127, 1257-1282.
175. Ahmad, G., Dickerson, M.B., Church, B.C., Cai, Y., Jones, S.E., Naik, R.R., King, J.S., Summers, C.J., Kroger, N., Dandhage, K.H. (2006) *Adv. Mater.* 18, 1759-1763.
176. Si, S., Bhattacharjee, R.R., Banerjee, A., Mandal, T.K. . (2006) *Chem. Eur. J.* 12, 156-165.
177. Bhattacharjee KK, D. A., Halder D, Haldar D, Di S, Banerjee A, Mandal TK. N. (2005) *Nanosci. Nanotechnol.* 2005: 5, 1141-1147 5, 1141-1147.
178. Slocik JM, N. R., Stone MO, Wright DW. . (2005) *J. Mater. Chem.* 7, 749-753.
179. Bhargava SK, B. J., Agrawal S, Coloe P, Kar G. . (2005) *Langmuir* 21, 5949-5956.
180. Slocik JM, N. R. (2005) *Small* 1, 1048-1052.
181. Janshoff, A., Galla, H.-J., and Steinem, C. (2000) Piezoelectric Mass-Sensing Devices as Biosensors - An Alternative to Optical Biosensors?, *Angewandte Chemie* 39, 4004-4032.

182. Ngeh-Ngwainbi, J., Suleiman, A. A., and Guilbault, G. G. (1990) Piezoelectric crystal biosensors, *Biosensors and Bioelectronics* 5, 13-26.
183. Sauerbrey, G. (1959) Verwendung von Schwingquarzen zur Wägung dünner Schichten und zur Mikrowägung, *Zeitschrift für Physik A Hadrons and Nuclei* 155, 206-222.
184. Frey, D. L., and Corn, R. M. (1996) Covalent Attachment and Derivatization of poly(L-lysine) monolayers on gold surfaces as characterized by polarization- modulation FT-IR spectroscopy, *Anal. Chem.* 68, 3187-3193.
185. Mullis, K. B., Faloona, F. A. (1987) Specific synthesis of DNA in vitro via a polymerase-catalyzed chain reaction, *Methods in Enzymology* 155, 335-350.
186. Gibbs, R. A. (1990) DNA Amplification by the Polymerase Chain Reaction, *Analyt. Chem.* 62, 1202-1214.
187. Erlich, H. A., Gelfand, D., and Sninsky, J. J. (1991) Recent Advances in the Polymerase Chain Reaction, *Science* 252, 1643-1651.
188. Chang, B., Taniguchi, H., Miyamoto, H., and Yoshida, S.-i. (1998) Filamentous Bacteriophages of *Vibrio parahaemolyticus* as a Possible Clue to Genetic Transmission, *J. Bacteriol.* 180, 5094-5101.
189. Cabilly, S. (1999) The basic structure of filamentous phage and its use in the display of combinatorial peptide libraries, *Mol Biotechnol* 12, 143-148.
190. Brewer, D., and Lajoie. (2000) *Rapid. Commun. Mass Spec.* 14, 1736-1745.
191. Bryan, G. W., and Gibbs, P. E. (1979) *J. Mar. Biol. Assoc. U.K.*, 59, 969-973.
192. Slocik, J. M., Moore, J. T., and Wright, D. W. (2002) Monoclonal Antibody Recognition of Histidine-Rich Peptide Encapsulated Nanoclusters, *Nano Letters* 2, 169-173.
193. Slocik, J. M., and Wright, D. W. (2003) Biomimetic Mineralization of Noble Metal Nanoclusters, *Biomacromolecules* 4, 1135-1141.
194. Jani, D., Nagarkatti, R., Beatty, W., Angel, R., Slebodnick, C., Andersen, J., Kumar, S., and Rathore, D. (2008) HDPâ€”A Novel Heme Detoxification Protein from the Malaria Parasite, *PLoS Pathog* 4, e1000053.

APPENDIX A

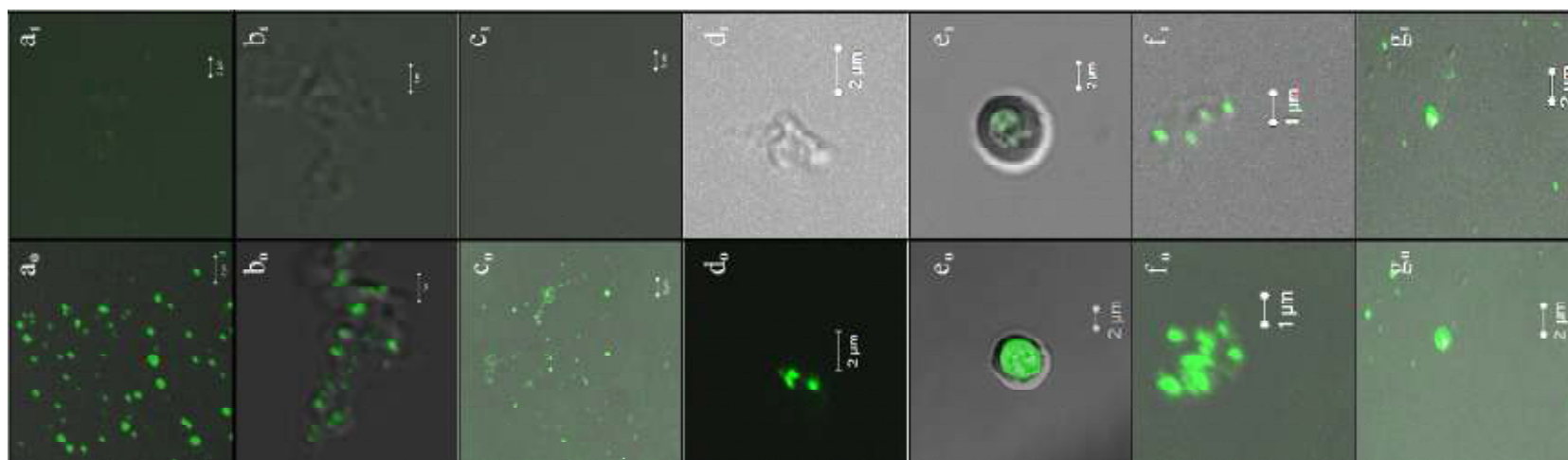


Figure 50. Confocal micrographs of NR labeled SNLB. in the presence of Fe(III)PPIX. The bottom panels show NR fluorescence from NR in lipid droplets prior to addition of Fe(III)PPIX. Careful addition of Fe(III)PPIX results in almost complete quenching of the NR signal at pH 4.8 (c) and 5.5(d), but incomplete or no quenching at pH 1.3(a),2.3 (b) 6.5(e), 7.3(f) and 8.1(g), top panel.

APPENDIX B

MN(III)PPIX Crystallization in Citric Buffer: DMSO System

The CB:DMSO system presented in chapter 4 was applied to MN(III)PPIX in hopes to synthesizing manganese(III) substituted protoporphyrin IX crystals. Here, preliminary data are presented.

Methods

Mn(III)PPIX was purchased from Frontier Scientific (Logan, Utah). 1mg of amorphous sample was dissolved in 1 mL solution of 1:1 50mM citric buffer (CB) to DMSO in a glass vial. The solution was immediately wrapped in foil and sonicated for approximately five minutes. Upon completion of incubation, the sample was washed with a solution of 0.1M sodium bicarbonate (pH 9). The dried sample was characterized with SEM, FTIR, and XRD (Figure 50).

Preliminary Results

Preliminary data demonstrates the success of Mn(III)PPIX crystallization using the CD:DMSO system. SEM analysis revealed that these crystals are rectangular in shape; however, crystal dimensions are not consistent across all samples (Figure 50a,b). Mn(III)PPIX crystals resemble those of Fe(III)PPIX crystals that are produced in the same system. However, a molecular examination of these Mn(III)PPIX crystals revealed that they differed from Fe(III)PPIX (Figure 50, c,d). FTIR analysis displayed distinct peaks at 1230, 1550, and 1720 cm^{-1} . XRD analysis revealed peaks at 7.2° theta that is likely to correspond to the {100} dominate crystal face of the crystal. Another distinct peak is present at 22.2° theta which probably

correspond to the {010} crystal face. Preliminary data presented here demonstrates the successful mediation of Mn(III)PPIX using the CB:DMSO system. Further examination of this pathway is necessary to better understand solvent mediated crystallization.

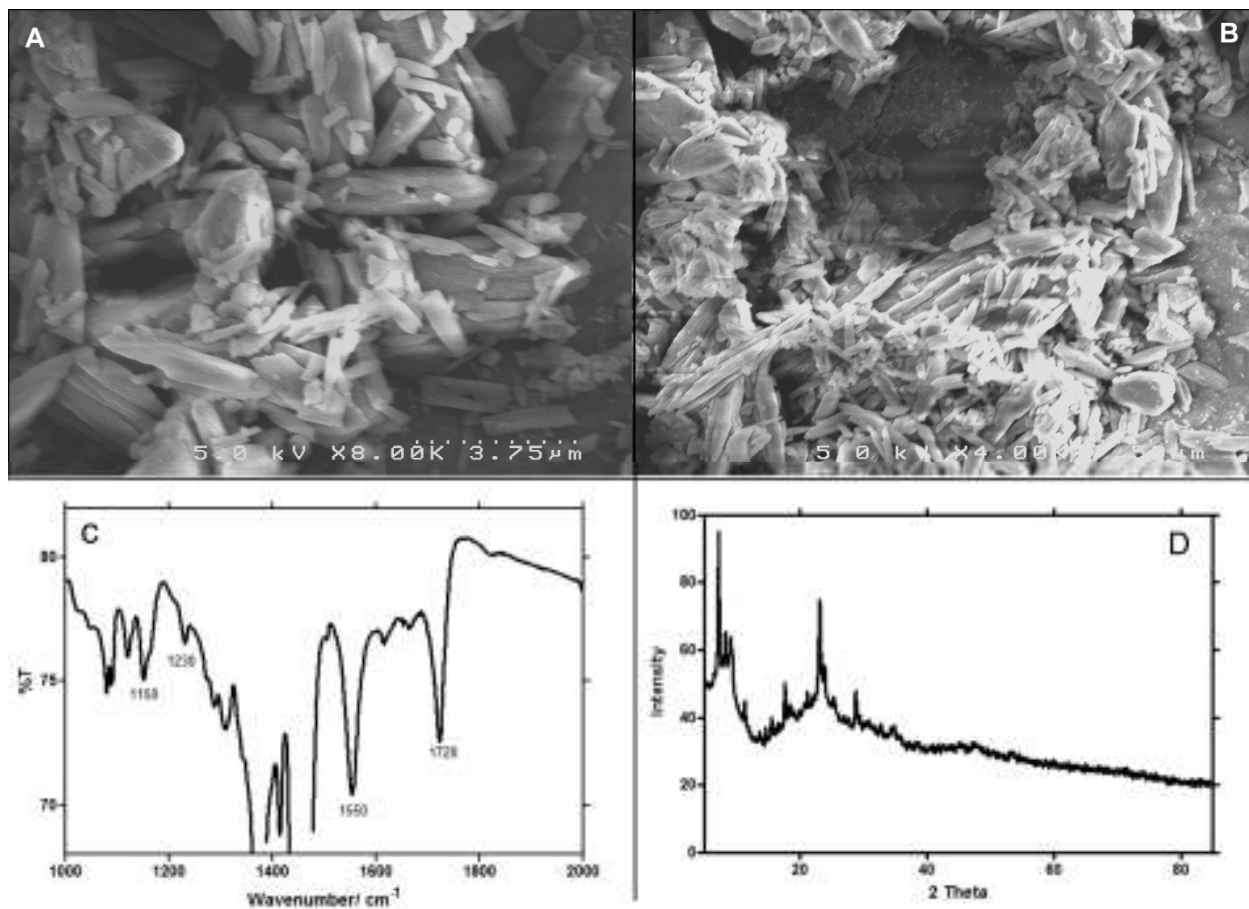


Figure 51. Characterization of Mn(III)PPIX crystals produced in citric buffer: DMSO system. SEM analysis(a,b) reveal that Mn(III)PPIX crystal resemble those of Fe(III)PPIX. However, IR (c) and XRD (d) analysis demonstrate that these crystals differed at the molecular level. IR regions $1350\text{-}1500\text{ cm}^{-1}$ is obscured by nujol matrix.

APPENDIX C

Phage Panning Protocol

1. Place ~2mg of hemozoin in small, sterile tube. Add 1 mL of sterile PBS, sonicate and vortex the sample. Centrifuge sample at 3,000 RPM for 30 seconds. Decant supernatant.
2. Add 400uL of sterile PBS and 100uL of stock phage. Incubate for 6 hrs at RT or 37C.. Wash unbound phage with PBST, 5X.
3. Start *e.coli* liquid culture from plate: take a sterile loop and remove *e.coli* from plate to a 50mL sterile tube containing 5mL of 2xYT broth. Store at 37C with gentle agitation. Do not tighten cap.
4. After 6 hours incubation of hemozoin and phage, wash with sterile PBS. Add 1mL of PBS. Gentle agitation (flipping mixture on Jonas' desk) for five mins. Centrifuge for 30 seconds at 3,000 RPM. Decant the supernatant. And repeat 5 – 10 X.
5. Remove supernatant from final wash. Elute with 150uL of PH2 and 0.2 M glycine for 15 mins. at room temperature. Keep sample mixing.
6. Add 30 uL of 1M Tris buffer for total of 180 uL. This is the phage output.
7. Add 100 uL of solution in step 6 to 100 uL of *e. coli* in a 50 mL tube. Incubate for 30 mins. at 37C to jumpstart amplification. After 30 mins. Add an additional 5mL of 2xYT + Kam (50um/mL) broth. Incubate at 37C overnight.
8. Make top agar lawn (when starting wash). Refer to titering protocol for steps on how to make top agar. Plate 10uL of phage (add the phage into the top agar solution and pour them together).
9. Next morning. Spin down *e.coli* + phage amplification for 5 mins. at 3000 RPM. Save supernatant in cryo tubes (1.5mL each). Use this amplified phage to repeat steps 1-9. Repeat 4-5 times.
11. Plate amplified phage using titering protocol. Count phage to determine concentration of amplified phage.

Note) all PBS is sterile and contained magnesium and calcium.

APPENDIX D

Phage Titering Optimized Protocol

1. From a phage stock where the titer is expected to be 10^{11} to 10^{14} pfu/ml 10-fold serial dilutions are made down 1 column of a 96 well microtiter dish.
2. From either the 6th or 7th fold dilution (choose the 6th if you expect the titer to be low and the 7th if you expect it to be high) make a series of 12 2-fold dilutions into PBS. 9I typically choose the 6th)
 - a) Transfer 50 uL 10-fold into 50uL PBS for the first, change tips, mix 3x, transfer 50ul of this well into another 50 ul, change tips, mix 3x, etc. Because at this point the concentration is very low it is essential to change tips between wells.
3. Plate 5 ul from each two fold dilution on the surface of a bacterial lawn, allow a few minutes for absorption, and incubate inverted over night at 37C.
4. Count the phages for each dilution \rightarrow pfu/5ul and plot $\log_{10}(\text{pfu}/5\text{ul})$ vs dilution # (disgard any dilution with fewer than 5 plaques because of sampling). The y-intercept of the trendline give the value at 0 dilution so the titer is determined by:

$$\text{Tier}(\text{pfu}/\text{ml}) = 10^b(10^a)(200);$$

a is the 10 fold dilution used by to start the 2-folds

b is the y-intercept

Note) the lawn is made using ~4mL 2xYT top agar at 55C, 20uL 1M IPTF, 20ul 10mg/ml Kanamycin, 80ul 2% XGAL, and 300uL *e.coli* cells from an overnight culture of XL1-blue. The reagents are vortexed quickly and poured onto the surface of a prewarmed 2xYT plate.

Anh N. Hoang

144 N. Timber Dr., Nashville, TN 37214 (801) 703-3721 Ahoang801@gmail.com

- EDUCATION:** Doctor of Philosophy, Interdisciplinary Material Science – projected August 2010
Vanderbilt University, Nashville, TN
Dissertation: “Crystal Engineering: Heme Detoxification in Malaria”
- Bachelor of Arts, Biochemistry, English - June 2006
Mount Holyoke College, South Hadley, MA
High honors
Thesis Title: “Time and stage specific of β -Fz1 expression during *Drosophila* metamorphosis”
- RESEARCH EXPERIENCE**
- BioMaterial Research Lab, (Vanderbilt University, Nashville TN), June 2007 - present
Graduate Research Assistant (Advisor: Dr. David Wright)
Research goal: To investigate the molecular interactions involved during the crystallization of a biomineral called hemozoin, the malaria pigment.
- Bioinorganic Chemistry Lab, (Cape Town, South Africa), July – December 2009
International Research Affiliate (Advisor: Dr. Timothy Egan)
Research goal: Investigated the role of neutral lipid droplets during the malaria infection
- Genetics Lab, (Mount Holyoke College, South Hadley, MA), August 2003-2006
Undergraduate research assistant (Advisor: Dr. Craig Woodard)
Research goal: To Investigate the functionality of a gene, β -Fz1, during the developmental stage of the fruit fly.
- Plant Genetic Lab, (University of Utah, Salt Lake City, UT), June – August 2003, 2004, 2005
Undergraduate Research Assistant (Advisor: Dr. Leslie Sieburth)
Research goal: To investigate the positioning and functionality of genes responsible for mutation in *Arabidopsis Thaliana*
- SCIENTIFIC PUBLICATIONS**
- Hoang AN, Ncokazi KK, de Villiers KA, Wright DW, Egan TJ. Crystallization of synthetic haemozoin (beta-haematin) nucleated at the surface of lipid particles. *Dalton Transactions*. 2010, 39 (5): 1235-1244.
- Stiebler R*, Hoang AN*, Egan TJ, Wright DW, Oliveira MF. Increase on the steady-state soluble heme levels in acidic conditions is an important mechanism for spontaneous heme crystallization *in vitro*. *PLoS ONE*. submitted *Participated equally in the manuscript
- Hoang AN, Sandlin RD, Omar, A, Egan TJ, Wright DW. Neutral lipid bodies: The Neutral Lipid Composition Present in the Digestive Vacuole *Plasmodium falciparum* Concentrates Heme and Mediates β -hematin Formation with an Unusually Low Activation Energy. In preparation.
- Hoang AN, Stiebler R, Swartz JD, Oliveira MF, Egan, TJ, Wright DW. Control of beta-hematin morphologies using solvent-water system. In preparation
- Hoang AN, Cliffl DE, Wright DW. Interactions of neutral lipids and Ferriprotoporphyrin IX during hemozoin formation in Langmuir-Blodgett films.
- Carter MD, Hoang AN, Wright, DW Hemozoin: a paradigm for biominerals in disease, in *Encyclopedia of Chemical Biology*, ed. Tadhg P. Begley, New York, 2008, vol. 4.
- CONFERENCE PRESENTATIONS**
- National Science Foundation (NSF) IGERT 2010 meeting, “The Neutral Lipid Composition Present in the Digestive Vacuole *Plasmodium falciparum* Concentrates Heme and Mediates β -hematin Formation with an Unusually Low Activation Energy”
- 2010 Material Research Society (MRS) spring conference, “Crystallization of synthetic hemozoin nucleated at the surface of lipid bodies”

Anh N. Hoang

144 N. Timber Dr., Nashville, TN 37214 (801) 703-3721 Ahoang801@gmail.com

-2009 10th Annual Nanoscience and Nanotechnology Forum, "Crystal Engineering Heme Detoxification", poster winner

-2009 Vanderbilt Institute of Chemical Biology Symposium, "Formation of the malaria pigment at the lipid-water interface," poster winner

AWARDS:

National Science Foundation (NSF) IGERT Fellow
Marieb Research Grant
Society of Plant Biologist undergraduate research grant
O.C Tanner Scholarship
Papa John's scholarship

PROFESSIONAL ORGANIZATION:

Nashville Material Research Society (MRS)
American Chemical Society (ACS)
Society of Women Engineers (SWE)